MASTERARBEIT / MASTER'S THESIS

Titel der Masterarbeit / Title of the Master's Thesis

„Neotectonics of the Diendorf Fault from Melk to Pulkau – analysing four fault segments along 80 kilometres“

verfasst von / submitted by

Eva-Maria Ranftl, BSc

angestrebter akademischer Grad / in partial fulfilment of the requirements for the degree of

Master of Science (MSc)

Wien, 2021 / Vienna, 2021

Studienkennzahl lt. Studienblatt / degree programme code as it appears on the student record sheet:	A 066 815
Studienrichtung lt. Studienblatt / degree programme as it appears on the student record sheet:	Masterstudium Erdwissenschaften UG2002
Betreut von / Supervisor:	Dr. Kurt Decker

Acknowledgements

Firstly, I want to thank my supervisor, Kurt Decker, who sometimes seems to know about his student's skills and competences better than they do themselves. Thanks for enabling this comprehensive thesis, for your support, encouragement and appreciation.

Equally, my gratitude goes to Esther Hintersberger. She introduced me to the working techniques of tectonic geomorphology and paleoseismological trenching and was a great support in the field – thank you very much for your invested time and your inspiring enthusiasm.

I'm also grateful to Michael Weissl for helping with field work and for his input on several topics, including archaeology, to Lisa Oppenauer, who accompanied me a lot and helped at the trench site, as well as Christopher Kollmann.

Moreover, many thanks go to Adrián Flores-Orozco, Timea Katona and Lukas Aigner (Research Unit Geophysics, TU Wien), for conducting the geophysical surveys and for providing some codes and advice.

Finally, I would like to thank Reinhard Roetzel for informing us about the Loisium construction pit and for sharing his professional expertise.

Abstract

The Diendorf-Boskovice-Čebín Large-scale Fault System is a more than 230 km long approximately SW-NE striking fault system on the southeastern margin of the Bohemian Massif. The Austrian part, referred to as Diendorf Fault System, extends over about 120 km in Lower Austria from Wieselburg in the southwest via Melk–Krems–Langenlois–Maissau and Pulkau to the Austrian-Czech border, then running further northeast into the area around Brno (Czech Republic). Left-lateral strike-slip faulting along the Paleozoic structure had been reactivated due to northbound Alpine orogenic processes in Cretaceous and Miocene times. Additionally, some authors reported Quaternary faulting, or even classified the fault system as recently active and potentially hazardous. Unequivocal evidence for recent fault slip, however, had not been provided so far.

This thesis' main objective was therefore to assess the tectonic activity of the Diendorf Fault in Lower Austria by means of geomorphological, geological and paleoseismological investigations. Integrated data from fault segments in the surroundings of Melk, Langenlois, Maissau and Pulkau, in combination with results of previous studies, reinterpretation of geophysical measurements and borehole data, give insights into the Quaternary tectonic evolution of this prominent morphological feature.

Morphotectonic parameters indicate landscape response to deformation at all four examined fault segments. This data is corroborated by estimates of Miocene and Quaternary average vertical displacement rates derived from marker horizons and geophysical imaging. Data indicate average vertical slip rates of about 0.01 mm/a at Langenlois and Pulkau. Clear evidence of Quaternary deformation is further derived from three outcrops exposing faulted Pleistocene loess or alluvium in a supposed pull-apart basin at Langenlois. Fault data indicate complex deformation including both, NNE-SSW directed extension, apparently not explicitly associated with the Diendorf Fault, and ENE-WSW directed extension, being in agreement with Pleistocene sinistral slip at the Diendorf fault. Although OSL dating is not completed yet, data suggest, that the youngest ages of faulted strata so far lie within the uppermost Late Pleistocene.

Tectonic activity of the Diendorf Fault, however, could not be confirmed in a paleoseismological trench at Melk, which exposed unfaulted fluvial gravels and the transition to silt with loess input.

Zusammenfassung

Das Diendorf-Boskovice-Čebín-Großstörungssystem ist ein über 230 km langes etwa SW-NE-verlaufendes Störungssystem am Südostrand der Böhmischen Masse. Der österreichische Teil (Diendorf Störungssystem) erstreckt sich über eine Länge von etwa 120 km in Niederösterreich von Wieselburg im Südwesten über Melk–Krems–Langenlois–Maissau und Pulkau bis zur Grenze zu Tschechien, von hier weiter nach Norden bis in die Gegend von Brünn. Sinistrale Seitenverschiebungen entlang der Paläozoischen Verwerfung wurden während nordwärts gerichteter Deformationsphasen der Alpidischen Orogenese in Kreide und Miozän reaktiviert. Weiters haben einige Autoren Quartäre Störungen beschrieben, oder das Störungssystem sogar als rezent aktiv und potenziell gefährlich eingestuft.

Ziel dieser Arbeit war es daher, die tektonische Aktivität der Diendorf Störung in Niederösterreich mittels geomorphologischer, geologischer und paläoseismologischer Methoden zu beurteilen. Umfassende Daten aus den Gebieten um Melk, Langenlois, Maissau und Pulkau, kombiniert mit Ergebnissen früherer Untersuchungen, Neuinterpretation geophysikalischer Messungen, sowie Bohrlochdaten, geben Einblick in die quartäre tektonische Entwicklung dieses markanten Elements.

Morphotektonische Parameter deuten entlang aller vier evaluierten Störungssegmente landschaftliches Feedback auf eine Deformation an. Die Annahmen werden durch Abschätzung der miozänen und quartären durchschnittlichen Vertikalversatzraten an Markerhorizonten, sowie geophysikalische Untersuchungen bekräftigt. Die Daten resultieren in Versatzraten von etwa 0.01 mm/a in Langenlois und Pulkau. Eindeutige Nachweise für quartäre Deformation liefern drei Aufschlüsse, die Störungen in pleistozänem Löss und Alluvium zeigen. Die vorgefundenen Störungen bilden komplexe Deformation ab, sowohl NNE-SSW-gerichtete Extension, die nicht unbedingt der Diendorf Störung zuzurechnen ist, als auch ENE-WSW-gerichtete Extension. Obwohl die OSL-Datierung für einige Proben noch ausständig ist, liegen bereits Alter des obersten Jungpleistozäns für die bisher jüngsten deformierten Sedimente vor. Es konnte jedoch keine Störungsaktivität der Diendorf Störung in einem paläoseismologischen Trench in Melk nachgewiesen werden, in welchem ungestörte alluviale Schotter und der Übergang zu Silt mit Lösseintrag beobachtet werden konnten.

Contents

1. Introduction

1.1. Regional Overview

The Diendorf Fault System is a SW-NE striking fault zone in Lower Austria and the Czech Republic. It extends from Wieselburg in the southwest via Melk–Krems–Langenlois–Maissau and Pulkau towards Brno (Czech Republic), where it is supposed to be kinematically linked to the Boskovice Furrow and the Čebín Fault (Figdor and Scheidegger 1977, W. Lenhardt et al. 2007, Pospíšil et al. 2009, Schermann 1966). These structures form the approximately 230 km long left-lateral Diendorf-Boskovice-Čebín Large-scale Fault System on the southeastern margin of the Bohemian Massif, prominent in geology and morphology. Extending over 120 km in Lower Austria alone, the Diendorf Fault (DF) roughly divides the crystalline plateau of the Bohemian massif, mostly consisting of Variscan granitoid and gneissoid rocks, from the Alpine Molasse foreland basin (see figure 1.1). The Waitzendorf Fault (WF) extends subparallely to the DF from Pulkau (Lower Austria) over the Austrian-Czech border to Znajmo (Roštínský, Pospíšil, and Svábenský 2013, Rötzel 1996). It may be regarded as a left-stepping stepover of the DF with connecting N-S striking normal faults (Decker 1999). A similiar dislocation is the Falkenberg Fault (FF) south of the DF (Nehyba et al. 2012), first mentioned by Waldmann 1922, known to form the southeastern boundary of the Zöbing half-graben and potentially cutting the granulites of Dunkelstein (G. Fuchs and Matura 1976). The left-lateral displacement along the DF is estimated between 25 km derived from distinctive offset of these granulites (Schermann 1966) and about 40 km derived from offset of magnetic anomalies (Figdor and Scheidegger 1977, G. Fuchs and Matura 1976). Some authors even assume the DF's continuation in the south under the East Alpine Mountain Front, e.g. Jaros and Mísař 1976.

1.2. Tectonic Evolution of the Diendorf Fault

A system of deep-seated conjugate wrench faults of about NW-SE and SW-NE striking shear zones cuts throughout the southern Bohemian Massif, with the Diendorf Fault being its easternmost structure (Brandmayr et al. 1995, Matte 1990, see figure 1.2). It developed before or early during the Variscan Orogeny in the Paleozoic, Jaros and Mísař 1976 assume a Lower Paleozoic primary evolution, because of the mode of Devonian rock deposits. Novotný 2012 describe deeply rooted high-velocity anomalies in depth recursive seismic tomography data corresponding to mafic intrusions near or within some of the regional fault zones. Their interpretation is, that during the Variscan orogeny massively intruded melts used the pre-existing fault systems.

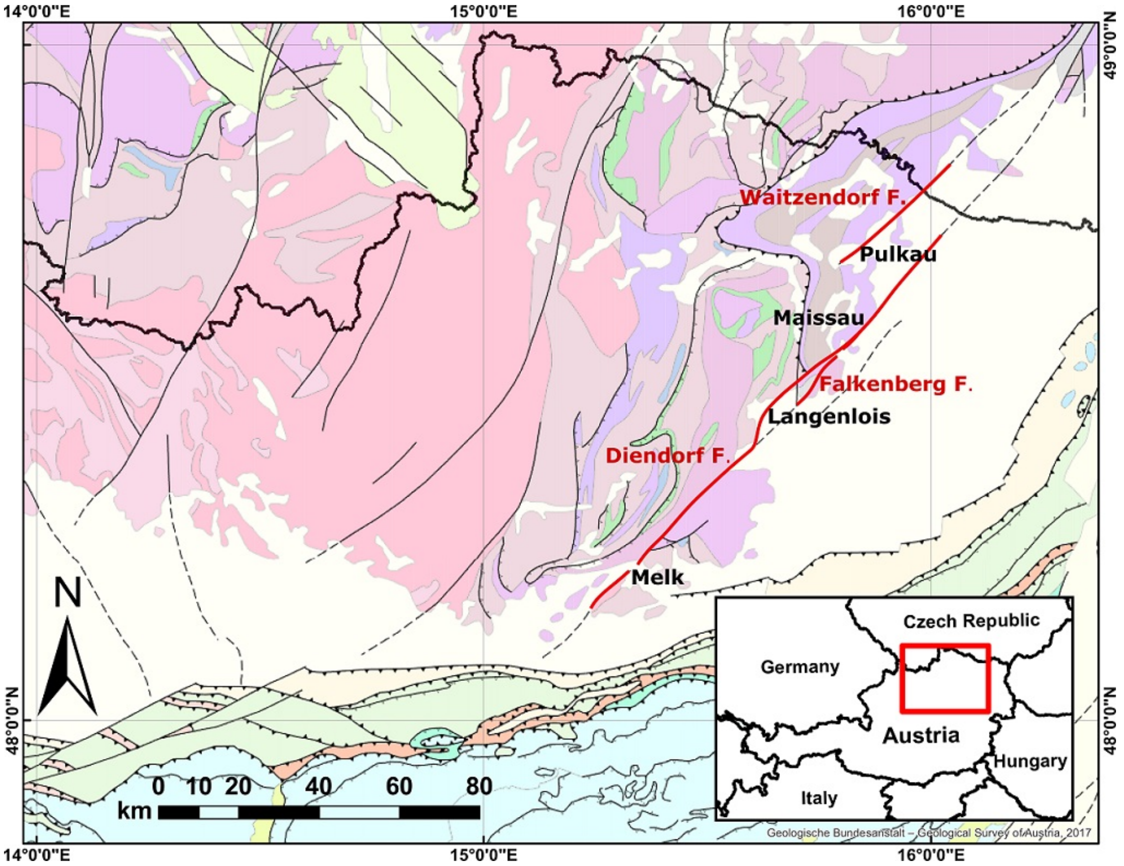

Figure 1.1.: Geographic and geological overview southern Bohemian Massif with DF and units of the East Alpine Thrust; legend in appendix.

However, main faulting activity was obtained towards the end of Variscan orogenic processes. Permo-Carboniferous clastic sediments fill the Boskovice Graben and the wedge-shaped Zöbing pull-apart basin (Lower Austria) along the DF; the deposits of the Zöbing Paleozoic have been well known since the 19th century (cf. Nehyba et al. 2012). Brandmayr et al. 1995 used ^{40}Ar/^{39}Ar for dating mylonitic shear zones of the Rodl-Kaplice and Danube Faults, which led to Lower Permian ages of about 287 Ma (NW-SE trending) and 288-281 Ma (SW-NE trending). Although characterized by ductile mylonitic fabric as well, the Diendorf shear zone was dominated by brittle deformation, presumably due to the maintenance of a very high fluid pressure during Variscan tectonics (Brandmayr et al. 1995). According to several authors (e.g. G. Fuchs and Matura 1976, Tollmann 1985), faulting was reactivated in the Mesozoic and Cenozoic, being influenced by Alpine orogenic processes, when the Bohemian Massif became the tectonic foreland of the N-directed movements of the Eastern Alps. Most likely since an overall tectonic regime similar to the Variscan palaeostress field had been established, Paleozoic faults reactivated locally at higher crustal levels (Stackebrandt and Franzke 1989, Brandmayr et al. 1995). Sediment fill of the Budějovice Basin and the Třeboň Basin (Czech Republic) document strike-slip movements in the Cretaceous and Miocene along the Jáchymov Fault and Rodl-Kaplice Fault (G. Fuchs and Matura 1976, Slánská 1976).

Miocene lateral extrusion compensating N-S convergence in the Eastern Alps (Ratschbacher et al. 1991) resulted in reactivation of the SW-NE trending sinistral horizontal faults. Outcrop evidence of Lower and Middle Miocene movements at the DF was described by Decker 1999, as well as the development of horst-and-graben structures (most likely Pliocene) in the area of the DF close to the Austrian-Czech border. WNW trending horst-and-graben formation did correspond to a stress field with vertical maximum stress axis σ_1 and a NNE-trending minimum stress axis σ_3. Such stresses could not have activated sinistral horizontal faulting. However late Quaternary tectonics and probably recent faulting activity again reflect northbound Alpidic deformation by left-lateral strike-slip movement (Decker 1999).

1.3. Quaternary Faulting and Recent Tectonic Activity: Recap and Objectives

Movements in Pleistocene loess were already assumed by Figdor and Scheidegger 1977, Scheidegger 1976 in Lower Austria (around Langenlois) due to joints approximately perpendicular or parallel to the DF. Hintersberger and Decker 2018 reported WNW-ESE striking normal faults in loess deposits and even a subvertical slickenside almost perpendicular to the DF ca. 5 km southwest of Langenlois. Leichmann and Hejl 1996 described a NNW-SSE trending fault in Quaternary sediments west of the Boskovice Furrow. Pospíšil et al. 2009, Pospíšil et al. 2012, Roštínský, Pospíšil, and Svábenský 2013 suggested recent tectonic activity on the eastern margin of the Boskovice Furrow, the DF and WF in Austria based on precise leveling, GPS measurements and geophysical data. The DF also was taken into account in the European Database of Seismogenic Faults (Basili et al. 2013) and the SHARE project. The project's main objective was to provide a community-based seismic hazard model for the Euro-Mediterranean region, including faults that were capable of generating earthquakes of magnitude $M \geq 5.5$. And Roštínský, Pospíšil, Svábenský, et al. 2020 classify the Diendorf-Čebín Tectonic Zone as a risk region with 1.5 mm/y and $M \geq 4.0$ based on GNNS-observed horizontal movements and seismicity from the eastern Bohemian Massif. This infers a potentially hazardous activity of the DF, which requires detailed observation. This study aims to asses the recent tectonic activity of the DF in Austria, combining various earlier results of multiple approaches with new geological data and reinterpretation of geophysical measurements and drilling data.

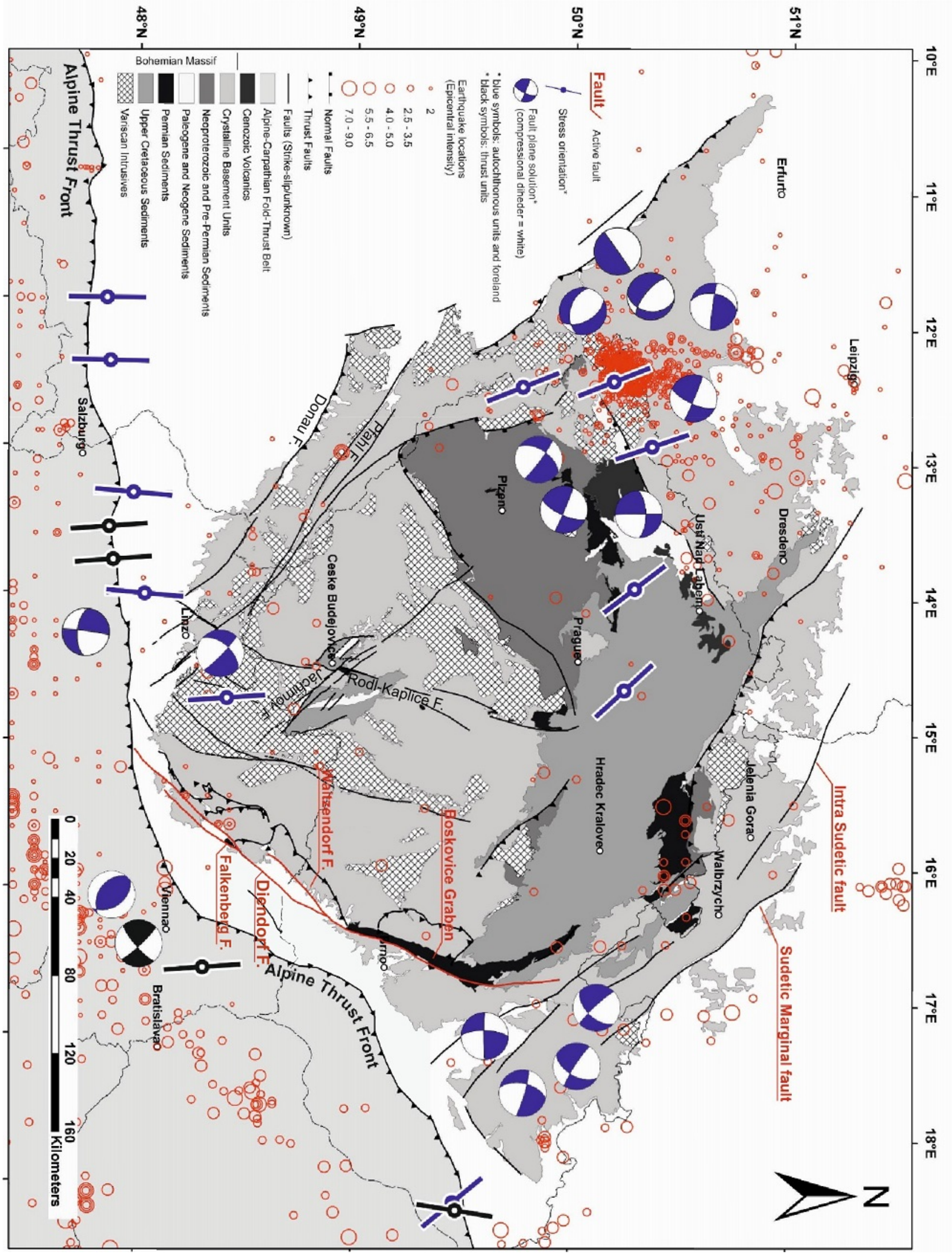

Figure 1.2.: Main tectonic units and fault systems in the Bohemian Massif and the Eastern Alps, with stress orientations and fault plane solutions, modified from Hintersberger and Decker 2018.

2. Methods

2.1. Tectonic Geomorphology

Landscape evolution is influenced by geological processes, see e.g. Burbank and Anderson 2012 for a comprehensive overview. Earthquakes often produce ground dislocations or surface ruptures – fault scarps. The threshold for producing detectable surface ruptures is intensity[1] $I \approx \text{VIII}$ (Michetti, Audemard M., et al. 2005, after Wells and Coppersmith 1994), that corresponds to a magnitude M of about 5 to 5.5. However, deformation caused by slowly moving (creeping) faults might also manifest in surface features. Depending on deformation rates and erosion rates, these features can be preserved in a landscape. The investigation of geomorphic markers is a tool to identify faults or fault scarps in maps, satellite or LiDAR images. Examples for geomorphic markers are conspicuously linear lineaments in topography, or fluvial systems reacting to vertical or horizontal movements of one fault block relative to another (figure 2.1). Such features or the computation of quantitative *morphotectonic parameters* can reveal disequilibria between deformation and denudation, due to a landscape's response to active tectonic forces.

The geometry of mountain fronts, stream profiles and the shape of valleys or catchment areas are commonly used for calculating geomorphic parameters. They are quantitative values, which help to assess the state of disequilibrium between uplift (or subsidence) and fluvial erosional processes. The parameters in table 2.1 have been calculated for some segments of the DF, as successfully applied in the southern Bohemian Massif e.g. by Popotnig et al. 2013.

2.2. Geophysical Measurements

For subsurface investigation at the DF geophysical imaging provided valuable information. The Technical University of Vienna[2] applied electrical resistivity tomography (ERT) and transient electromagnetic (TEM) measurements around Melk (Zelking-Matzleinsdorf and Großpriel). Sedimentary thickness in Maissau was obtained from reflection (and refraction) seismic profiles by Meurers et al. 1993.

For the **electrical resistivity tomography (ERT)** an electric current is injected into the ground through a pair of electrodes and the resulting voltage is measured be-

---

[1] European Macroseismic Scale (EMS-98), Environmental Intensity Scale (ESI 2007)

[2] Department of Geodesy and Geoinformation, Research Division Geophysics – Wiedner Hauptstraße 8/E120, 1040 Vienna

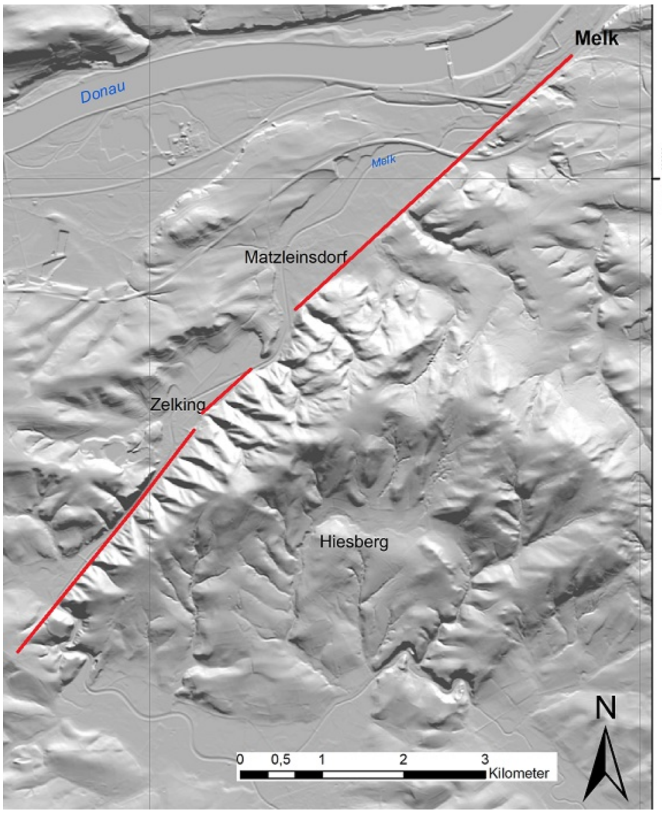

Figure 2.1.: LiDAR image of a linear mountain front along the DF with triangular facets due to active incising creeks at Zelking, 6 km southwest of Melk.

tween another pair of electrodes (Everett 2013, chapter 4). An apparent resistivity can be obtained, which serves as an indicator of the actual underlying electrical resistivity of the ground. Different arrangements of the electrodes give information at different depths and lateral positions. Inversion of the data provides a 2D (or 3D) resistivity section. For the geoelectrical measurements along the DF, induced polarization imaging has been applied using a 10-channel Syscal Switch72pro (Iris instruments), which permits the deployment of 72 electrodes and simultaneous collection of readings in 10 voltage dipoles for every current injection. Measurements along several profiles with 5 m spacing and/or 1 m spacing at four sites have been conducted.

Reflection and refraction seismic surveying is based on introducing mechanical energy into the subsurface and recording the resulting mechanical response (Everett 2013, chapter 6). An active source of mechanical energy generates seismic waves (elastic waves) propagating through the ground. The waves are reflected (or refracted) on layers with changing rock properties, following Huygens' principle and Snell's Law. Reflected waves are recorded at the ground surface by seismic receivers, geophones. The first arrivals of

Mountain front sinuosity $Smf = \frac{Lmf}{Ls}$		
Lmf = length of the mountain front along the foot of the mountain; Ls = length of a straight line along the mountain front.	$Smf < 1.4$ – active tectonics, $Smf > 3$ – inactive tectonics	Bull and McFadden 1977
Stream gradient index $SL = \frac{\Delta H}{\Delta L} \cdot L$		
$\frac{\Delta H}{\Delta L}$ = channel slope or gradient of the reach; L = total channel length from the midpoint of the reach of interest up-stream to the highest point on the channel.	High SL values - less rock resistance	Hack 1973
Ratio of valley floor width-to-height $Vf = \frac{2 \cdot Wdf}{(Eld - Evf) + (Erd - Evf)}$		
Wdf = width of the valley floor; Evf = elevation of the valley floor; Eld and Erd = elevation of the left and right valley divides	Low values (< 0.5 after Burbank and Anderson, 2001) deep valleys with active incision	Bull and McFadden 1977
Drainage elongation ratio $Re = \frac{2 \cdot \sqrt{\frac{A}{\pi}}}{Lb}$		
A = basin area; Lb = basin length	$Re < 0.5$ active tectonics $Re > 0.75$ inactive tectonics	Schumm 1956
Elongation ratio $Bs = \frac{Lb}{Wb}$		
Lb = length of the basin from its mouth to the most distal point; Wb = basin width	High values – high tectonic activity	Ramírez-Herrera 1998
Circularity index $C = \frac{Ab}{Ac}$		
Ab = basin area; Ac = *area* of a circle with the same length of perimeter as the basin.	Low values – more elongated basin	Bell 2004
Basin shape $Rf = \frac{Ab}{Lb}$		
Ab = basin area; Lb = basin length from its mouth to the most distal point	Low values – high tectonic activity	Talling et al. 1997

Table 2.1.: Geomorphic indices used in this study, modified from Popotnig et al. 2013; first column: variables used in formulae; second column: inferences of calculated values; third column: references.

P- or S-waves give the two-way travel time from the source to the reflector, and from there to the receivers, which can be inverted into reflector depths.

2.3. Structural Geology, Sediment Analysis and Outcrop Documentation

Several outcrops, most of them anthropogenic (building pits, clay pits, vinyard terraces etc.), have been investigated in terms of structural geology. The main objective was to detect dislocations and shear senses in rocks and sediments in order to infer recent tectonic movements locally or at least to outline the deformational history along the DF, as proposed by e.g. Brandmayr et al. 1995, Decker 1999, Schermann 1966. Geological compass measurements (dip direction, inclination angle, striation) on faults, slickensides and joints in crystalline as well as in unconsolidated rocks were carried out to determine fault kinematics and, where possible, the associated stress regime. Fault geometry has been examined, especially bending along strike-slip faults is important for interpretation and discussion in the following chapters, see figure 2.2 for explanation. A releasing bend may result in an extensional region and the formation of a pull-apart basin (*negative flower structure* in vertical section), inducing secondary normal faulting. In addition, fault offsets could be measured in several cases such as a building pit in Langenlois. Outcrops and significant details were outlined and sketches transformed into digital drawings in Inkscape. Pictures of outcrops or detail structures were taken for documentation, for larger areas photomosaics were produced by manually orthorectifying and stitching in ArcGIS. Sediment samples from Großpriel were granulometrically analysed by sieving and, for grain size $< 0.063\,\mathrm{mm}$, SediGraph analysis (micrometrics SediGraph III). Grain shape, roundness and lithology were checked under a Nikon SMZ-U microscope.

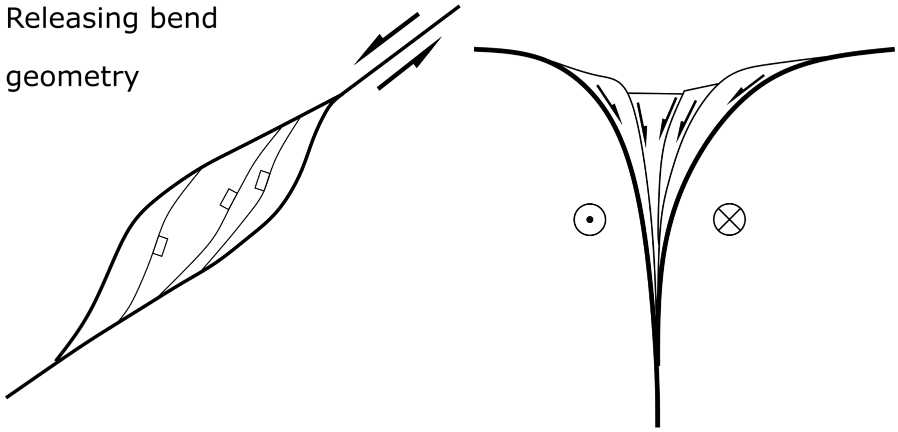

Figure 2.2.: Releasing bend of sinistral strike-slip fault in plan view (left) and vertical section (*negative flower structure*, right).

2.4. Paleoseismological Trenching

McCalpin 2008 defines paleoseismology as the study of prehistoric earthquakes, especially their location, timing (or recurrence), and size (magnitude). Whereas seismological data is provided by instrumental recordings during earthquakes, paleoseismology is the interpretation of geologic evidence (ground effects in geologic and geomorphic record as in Michetti, Audemard M., et al. 2005) created during *paleoearthquakes*. Coseismic deformation structures (*seismites* sensu Vittori et al. 1991) such as rock escarpments, scarp-derived colluvial wedges, fissure fills, soft-sediment deformations and also secondary structures like ground liquefication or landslides can reveal prehistoric ground motions.

Where no obvious fault scarp, fault rocks or seismites crop out, geologists may look for earthquake evidence in the shallow subsurface in paleoseismological trenches. That large earthquakes can occur without having created surface rupturing in historical times, showed e.g. the Sumatra (Indonesia) earthquake of 2004 – with a death toll of > 250000 from tsunamis accompanying the earthquake. In the Bohemian Massif Štěpančíková et al. 2010 were the first to apply the trenching technique at the Sudetical Marginal Fault. They could derive four faulting events – in an area where no earthquakes are known from the historical record. Hintersberger, Decker, et al. 2018 could reassess the earthquake hazard at the Markgrafneusiedl Fault of the Vienna Basin, a region with moderate seismicity about 70 km from the DF.

Paleoseismological trenching might reveal earthquakes, that happened tens to hundreds of thousand years ago, depending on the limits of absolute age dating of the displaced sediments, whereas seismological data exists since the early 20th century. In the investigated area and the adjacent Bohemian Massif historical earthquake documentation doesn't go back further than a few hundred years (Nasir et al. 2013); data are linked to human settlement, existing writing systems and the noticeability of ground shaking, which results in sparse historical earthquake data from the time prior to seismological observations. This limited data can be extended and supplemented by paleoseismological methods. However, trench investigations along a fault segment are not always able to capture all recent surface faulting events which occurred along that segment (Michetti, Audemard M., et al. 2005). Paleoseismological trenching was the next logical step, after geomorphology and geophysical data indicated promising results, especially around Melk. In Großpriel an about 30 m long NW-SE striking trench with a width of 1.5 m was excavated, and a maximum depth of 3.5 m. 26 m of the northeastern wall were cleaned and about 10 m of the southwestern wall, which was benched for safety reasons around the deepest spot. Both walls were covered by a 0.5 x 0.5 m grid – horizontal lines A to F, vertical lines consecutively numbered – and mapped in detail at the scale of 1:15. Pictures were taken of areas of 1.5 x 1 m maximum to produce a high-resolution photomosaic.

2.5. Luminescence and Radiocarbon Dating

To obtain numerical ages for sedimentation e.g. after the latest supposed deformation event, the following geochronological methods were applied.

Optically Stimulated Luminescence (OSL) dating for this thesis is performed by the Department of Geology, University of Innsbruck[3]. One out of the four studied sites around Langenlois, the former brickyard, has been dated by Thiel et al. 2011. The OSL method is based on time dependent accumulation of radiation damage in the crystal lattice of grains (quartz and potassium-rich feldspar) due to natural radiation after deposition of a sediment; more detailed information e.g. in Feathers 2008. The absorption of radiation energy creates lattice defects (free electrons or vacancies). Sunlight heals such defects during transport (referred to as *bleaching*), which resets the counting. The afterwards accumulated defects can be artificially healed by radiating with a narrow bandwidth of visible light; electrons fall back into their initial state, which produces a light signal (luminescence). The intensity of the signal is proportional to the time passed after deposition, and the *burial age* is computable.

Samples had been taken by hammering opaque tubes into the profiles and directly sealing them to be lightproof. Reference sediment from the immediate sample surrounding, required for natural dose rate determination, was put into plastic bags. For the locations Geißberg and Wolfsgraben the in-place radiation has been detected by in-situ gamma ray spectrometry (ORTEC DigiBase with 2 inch NaI(Tl) detector) combined with beta counting of the sample material (RisøGM-25-5 counter) to define the dose rates. Further methodological details on OSL age dating of our samples are described in the unpublished report of the Luminescence Dating Lab, University of Innsbruck (Meyer 2019).

Radiocarbon (^{14}C) dating of two charcoal samples taken from the paleoseismological trench was assigned to the Beta Analytic testing laboratory[4]. They use accelerator mass spectrometry for carbon isotope fractionation. The ^{14}C method was initially proposed by Libby 1946, Libby 1952. ^{14}C isotopes form in the stratosphere due to ionising radiation. The overall atmospheric ^{14}C content is constantly represented in organic carbon by entering the biological carbon cycle via carbon dioxide due to plant metabolism and food intake. After the death of an organism, the exponential radioactive decay of ^{14}C starts. On account of a half-life of 5568 years (*Libby half-life* used by Beta Analytic) the time of death can be calculated, when the present day ratio of ^{14}C to the stable carbon isotopes (^{12}C and ^{13}C) is determined.

Additionally we profited from unexpected **archeological findings** enabling temporal approximation of at least one layer exposed in the paleoseismological trench – the one containing the charcoal –, clearly identifiable as anthropogenic, because of a fire pit with pottery finds. In a stratigraphically older layer, we spotted a flint, probably a shaped silex tool. The findings were reported to the Federal Monuments Authority Austria[5] and site investigation was carried out by ARDIG[6].

---

[3] Univ. Ass. Prof. Mag. Dr. Michael Meyer, Head of Luminescence Dating Laboratory – Innrain 52, 6020 Innsbruck

[4] https://www.radiocarbon.com/

[5] *Bundesdenkmalamt*, Department of Lower Austria – Hoher Markt 11, Gozzoburg, 3500 Krems a. d. Donau

[6] Archäologischer Dienst GmbH – Porschestraße 39, 3100 St. Pölten

3. Data and Interpretations

3.1. Tectonic Geomorphology Data

3.1.1. The Zelking Segment (Melk)

Southwest of Melk, around Zelking and Großpriel Ranftl 2017 assessed the tectonic activity of a perfectly linear fault segment of the DF with triangular facets (as seen in figure 2.1, chapter 2.1, geographical overview and geological map in figure 3.2). Longitudinal stream profiles had been studied and the following quantitative morphotectonic parameters had been computed: stream gradient-index SL, valley floor width-to-hight Vf, drainage elongation ratio Re, elongation ratio Bs, circularity index C and basin shape Rf. Hintersberger and Decker 2018 additionally calculated the mountain front sinuosity Smf. Calculation of the geomorphic indices is based on the 10 x 10 m DEM of Lower Austria and fluvial river profiles and valley cross sections extracted from it.

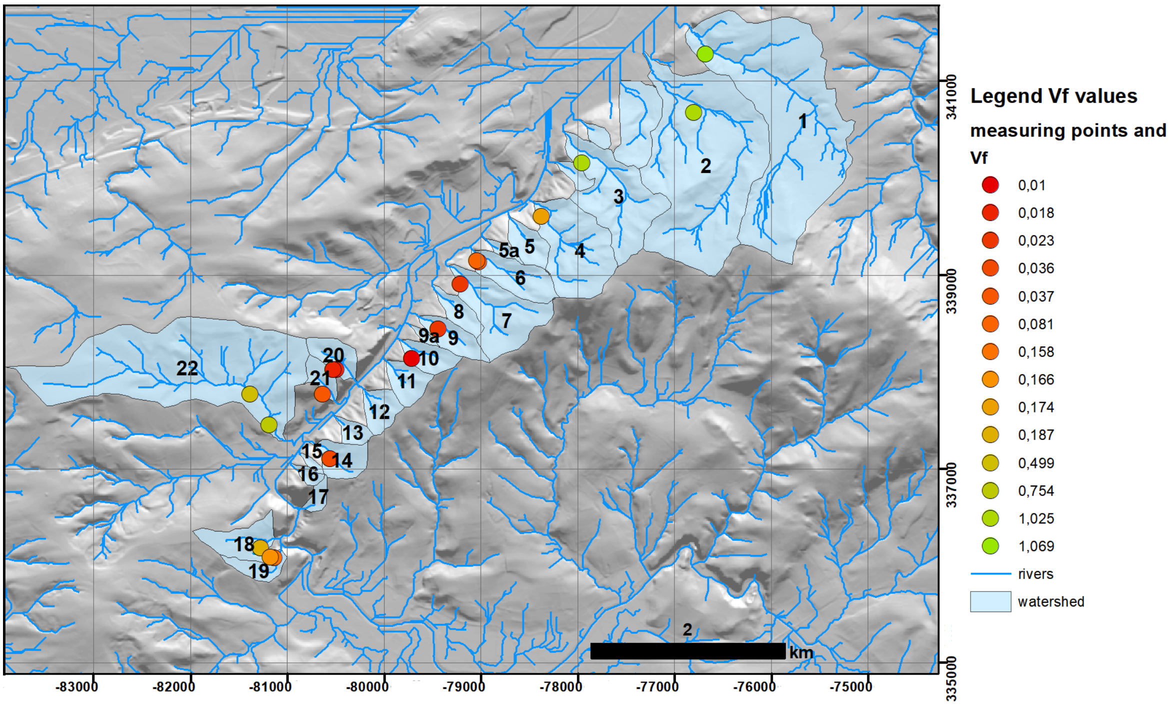

Figure 3.1.: Catchment areas of the assessed valleys with measuring points of valley floor width; colours correspond to Vf values, red indicating active incision.

In addition to the topographic information of the DEM, the valley floor widths were acquired by field measurements (dry ditches excluded). Figure 3.1 shows the investigated drainage basins with measuring points of the valley floor widths. Red to light orange colours for low Vf values indicate active incising streams, whereas green colours suggest more mature fluvial systems.

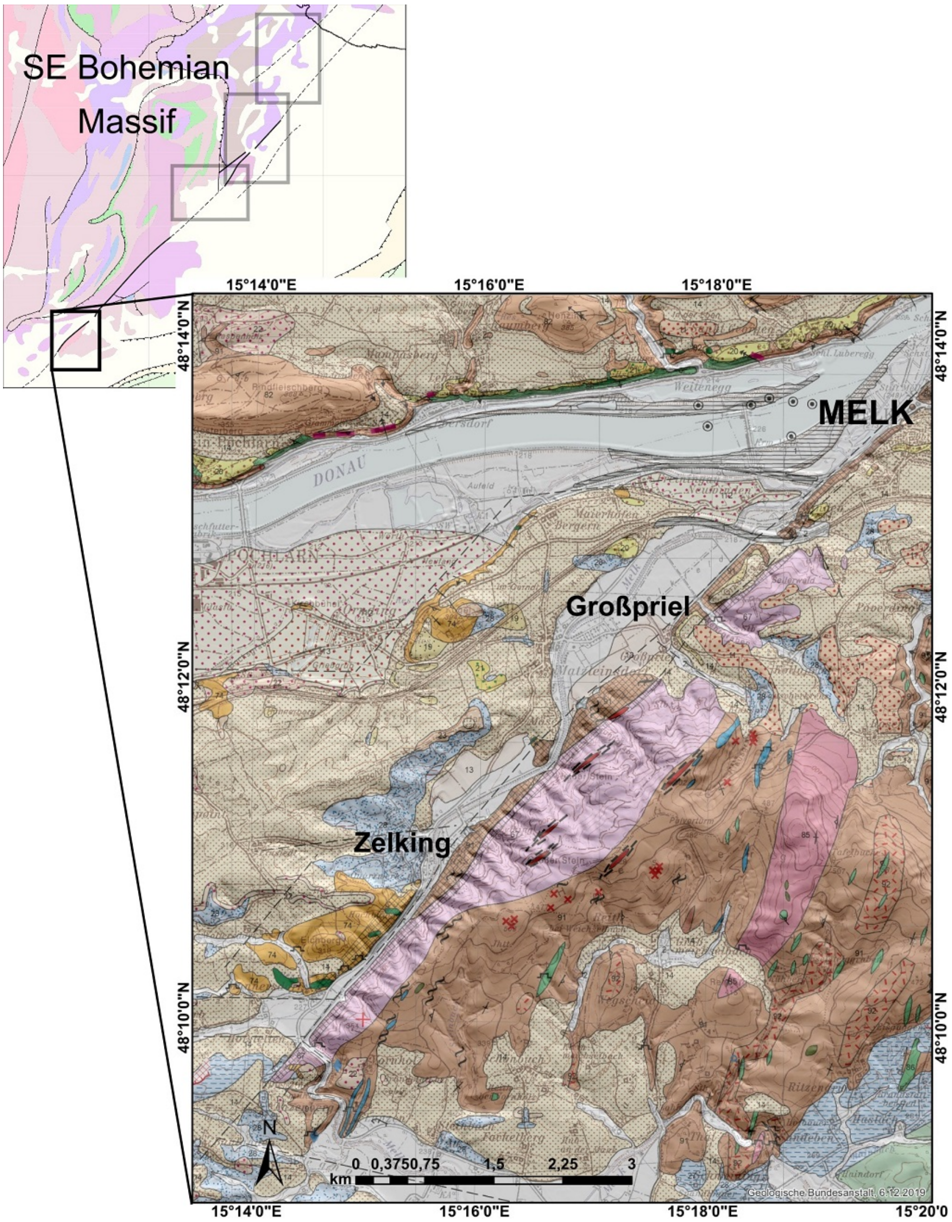

Figure 3.2.: Geographical overview of fault segment location Zelking (Melk) and local geology after Kreuss and Linner 2018.

Table 3.1 gives the mean values of the geomorphic indices computed and the calculated values for valley number 1 located in Großpriel, which had been chosen for trenching later (read more in chapter 3.2.2). The mean values are similar to the morphotectonic calculations of stream number 1; Vf and Bs are exceptions, implying inactive fluvial erosion, however very high Bs values in the area are given by small elongated watersheds without actual creeks (see tables of all calculated parameters in appendix A.1, A.2). The anomalous (upward convex) stream profile of valley number 1 is shown in figure 3.3, with the SL values pointing out knickpoints, usually indicating disturbance of a watercourse. They could refer to a fault scarp, but also to less erodible rocks or higher flow energy, e.g. at a confluence – anyway, the profile shows, that the fluvial erosion is out of equilibrium. Low Vf values on both fault blocks indicate an overall uplift of the area and/or incision of the River Melk, which runs parallel to the DF between both crystalline blocks. The stream profile of the Melk has been analysed, although the river had been straightened and engineered between Zelking and Großpriel. See the longitudinal profiles of the rivers Melk and Mank plus SL values in figure 3.4. The obvious knickpoints or changes in the watercourse of the River Melk are either anthropogenic (at 15000 m and 28000 m) or can be explained by the confluence of the rivers Melk and Mank (at about 2000 m) and by lithological changes (at 8000 m of Melk, or 7000 m of Mank). The stream profiles are clearly anomalous though. The upward convex shape would support the idea of an overall uplift of both fault blocks at Zelking, as geomorphology and morphotectonic parameters pointed out in the first place.

All in all, data, on-site morphology and nearby seismic activity gave a vague impression of ongoing faulting. A geophysical field survey was planned and conducted for additional information (see chapter 3.2.1).

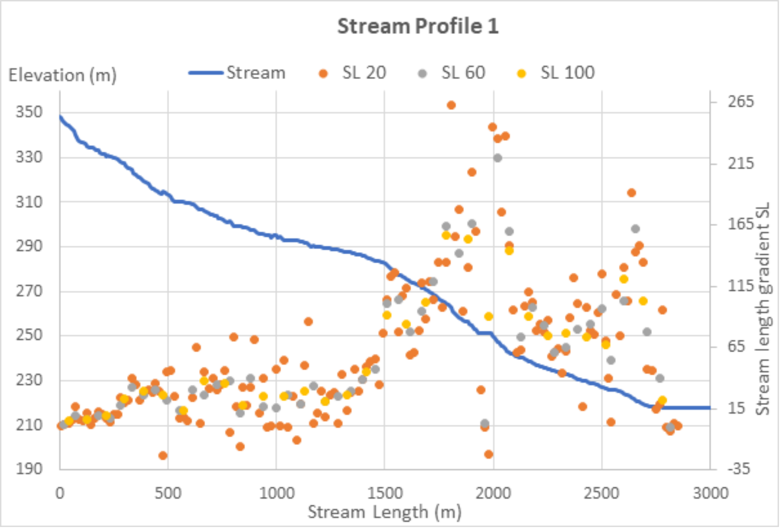

Figure 3.3.: Stream profile of valley number 1 with SL values calculated for stream length intervals of 20, 60 and 100 m identifying knickpoints (Ranftl 2017).

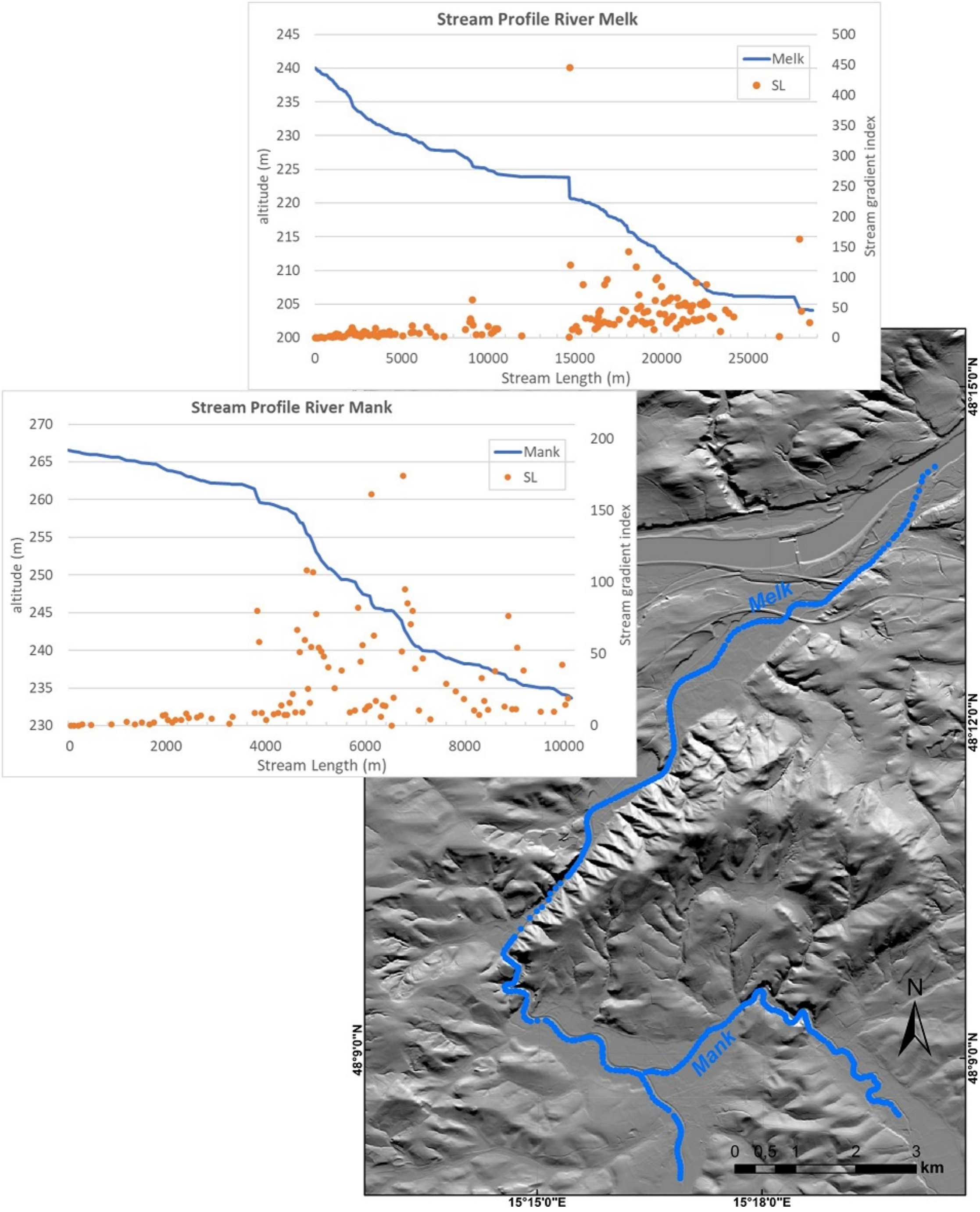

Figure 3.4.: Stream profiles of the rivers Melk and Mank with SL values for knickpoint identification, calculated for stream length intervals between the manually picked coordinate points given in the LiDAR image (blue).

Smf	SL	Vf	Re	Bs	C	Rf
mean (all valleys Zelking)						
1.1	62.17	0.26	0.435	3.501	0.423	0.155
valley number 1						
1.1	58.87	1.07	0.435	2.605	0.441	0.149

Table 3.1.: Average values of indices computed by Ranftl 2017 and Hintersberger and Decker 2018 for all valleys (top) and indices for valley number 1 (bottom).

3.1.2. Maissau and Pulkau Fault Segments

The northernmost prominent linear fault scarp of the DF is formed by the granites of Maissau. Some kilometres to the northeast, the stepover of the DF to the linear segment of the Waitzendorf Fault (WF) at Pulkau is assumed (Decker 1999, Schnabel 2002) – a geographical overview and the geological map are given in figure 3.5. Southwest from Maissau a part of the Zöbing pull-apart basin at a releasing bend of the DF is visible and the Falkenberg Fault (FF) as the southern border of the basin. South from Pulkau three dashed lines indicate the assumed N-S striking linking faults between DF and WF.

Quantitative morphotectonic parameters from the segments Maissau and Pulkau were computed by Hintersberger and Decker 2018 with methods as the ones described for the Zelking Segment in chapter 3.1.1. Only the study of the Vf values demanded a field survey carried out by the author[1] to acquire the valley floor widths for calculation. See Vf values in figure 3.6 (symbols red to green – active to inactive), as well as drainage basins with colour scale for Re values. As the Re, also Bs, C and Rf calculations are based on the 2D-geometry of these drainage basins (full table in appendix A.4), so all indices show similar results. Vf and Re (or Bs, C and Rf) do not match significantly, as seen in figure 3.6.

Furthermore the Vf values have not been calculated for exactly the same watersheds as the other parameters, which makes comparison difficult. Therefore, the table of mean values for the Maissau and Pulkau segments (table 3.6) gives the overall data (top), as well as isolated mean values from Maissau and Pulkau, where Vf-assessed valleys and watersheds overlap. Compared to a mean Vf for all valleys of 0.94, the mean Vf excluding valleys 0, 1, 38, 39, 40 (along one of the supposed N-S linking faults at the stepover between DF and WF) is only 0.23. Average Vf values of both, the Maissau and the Pulkau segment, are 0.28, which suggests active fluvial erosion, whereas average indices based on basin geometry do not show significant divergence compared to the overall mean. The detailed image of the Zöbing pull-apart basin in figure 3.6 gives rather high Vf values crossing the basin with a mean Vf of 0.72, but low Vf values close to the supposed DF and FF.

---

[1] with special thanks to the students of the course 'Active Tectonics', summer term 2019

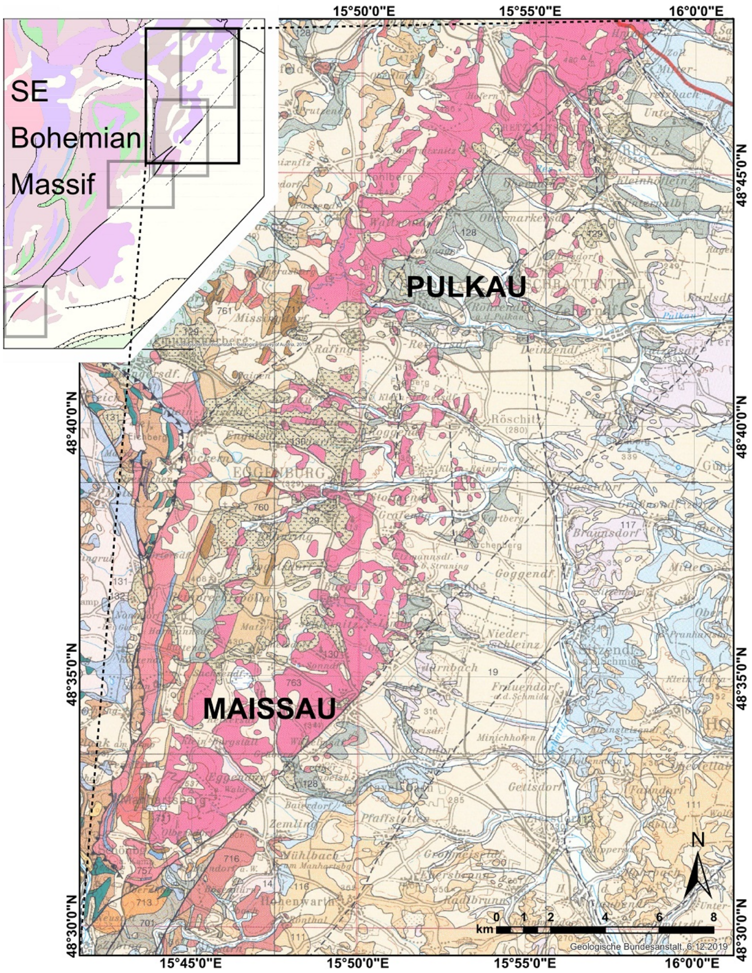

Figure 3.5.: Geographical overview of fault segment locations Maissau and Pulkau in the geological map of Lower Austria after Schnabel 2002.

Smf	Vf	Re	Bs	C	Rf
mean (all valleys DF northeast and WF)					
1.46	0.94	0.397	3.946	0.360	0.129
mean (Maissau)					
1.4	0.28	0.393	3.831	0.358	0.123
mean (Pulkau, WF)					
1.43	0.28	0.403	3.846	0.354	0.131

Table 3.2.: Average values of geomorphic indices computed by Hintersberger and Decker 2018 for valleys and catchments displayed in figure 3.6. Mean values of Maissau include valleys 30–36, 12 and adjacent one (S); mean values of Pulkau (WF) include valleys 6–11, 28 and intermediate ones without numbering.

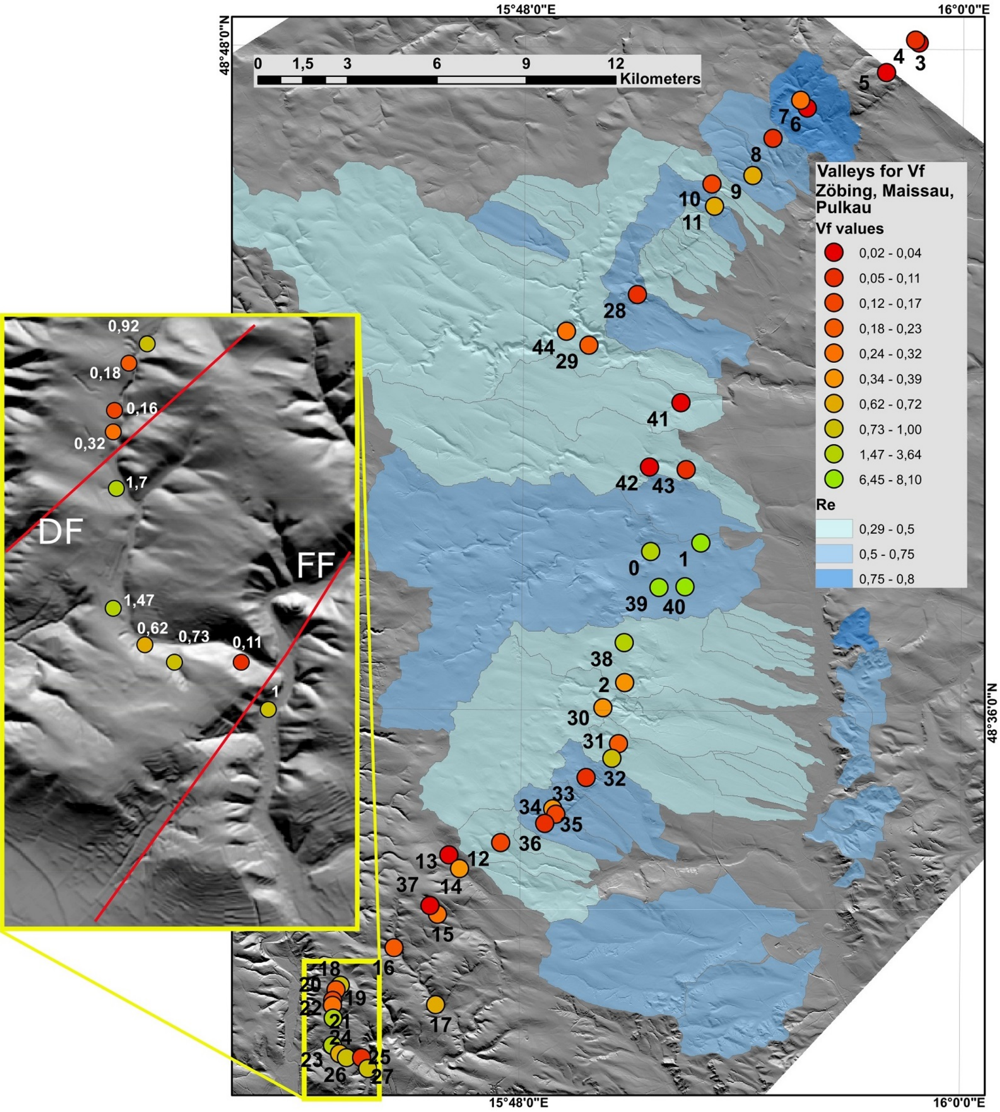

Figure 3.6.: Vf values as white labels and symbols (red indicating active incision) at measuring points of Wdf for Vf calculation around Maissau, Pulkau and the Zöbing pull-apart basin (in detail); catchment areas for other parameters, showing Re in different shades of blue, after Hintersberger and Decker 2018.

Hintersberger and Decker 2018 also mentioned sinistral deflection of rivers at Maissau (figure 3.7). This could hint to young or recent strike-slip tectonics at the DF in that area, whereas the calculated geomorphic indices assess fluvial response to relative vertical movements. Recent strike-slip faulting at Maissau could reactivate basin formation at the releasing a few kilometres to the southwest. Four outcrops around Langenlois, giving more insight on Quaternary deformation, are described in chapters 3.2.3 to 3.2.6.

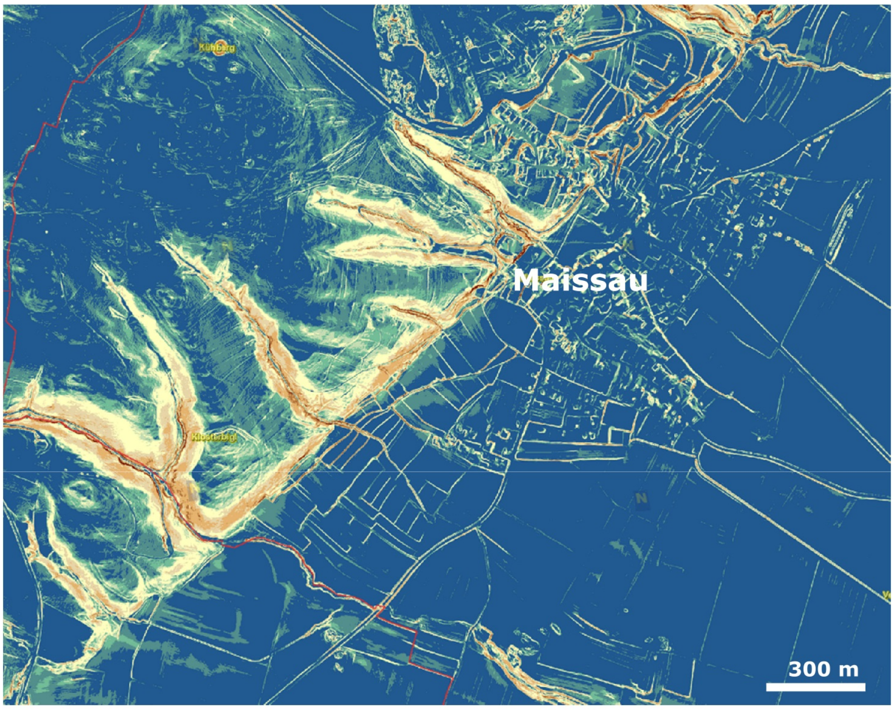

Figure 3.7.: Slope angle map of Maissau showing sinistral deflection of rivers (from Hintersberger and Decker 2018).

3.2. Quaternary Deformation Data

3.2.1. Quaternary Thickness from Shallow Boreholes and Geophysical Measurements (Melk)

Southwest of Melk, regarding the construction of a hydroelectric power plant at the Danube, numerous **shallow boreholes** in varying depth had been drilled in the 1970s and 1980s. Figure 3.8 displays borehole locations of investigated data (full table in appendix A.5). The symbol size is corresponding to the Quaternary thickness and the colour reflects the underlying lithology of Quaternary sediments. Yellow means, the well did only reach Quaternary rocks, crystalline rock under Quaternary is red and sands of the Linz-Melk Formation[2] under Quaternary blue. The labels give the top of crystalline rocks, when reached. Within the green ellipse in the northeast, some drillings reach comparatively low top elevations of crystalline rocks (125 to 155 m), where the River Danube converges the DF.

---

[2] Oligocene–Miocene marine quartz sands, quarried in the area; cf. Rötzel et al. 1983

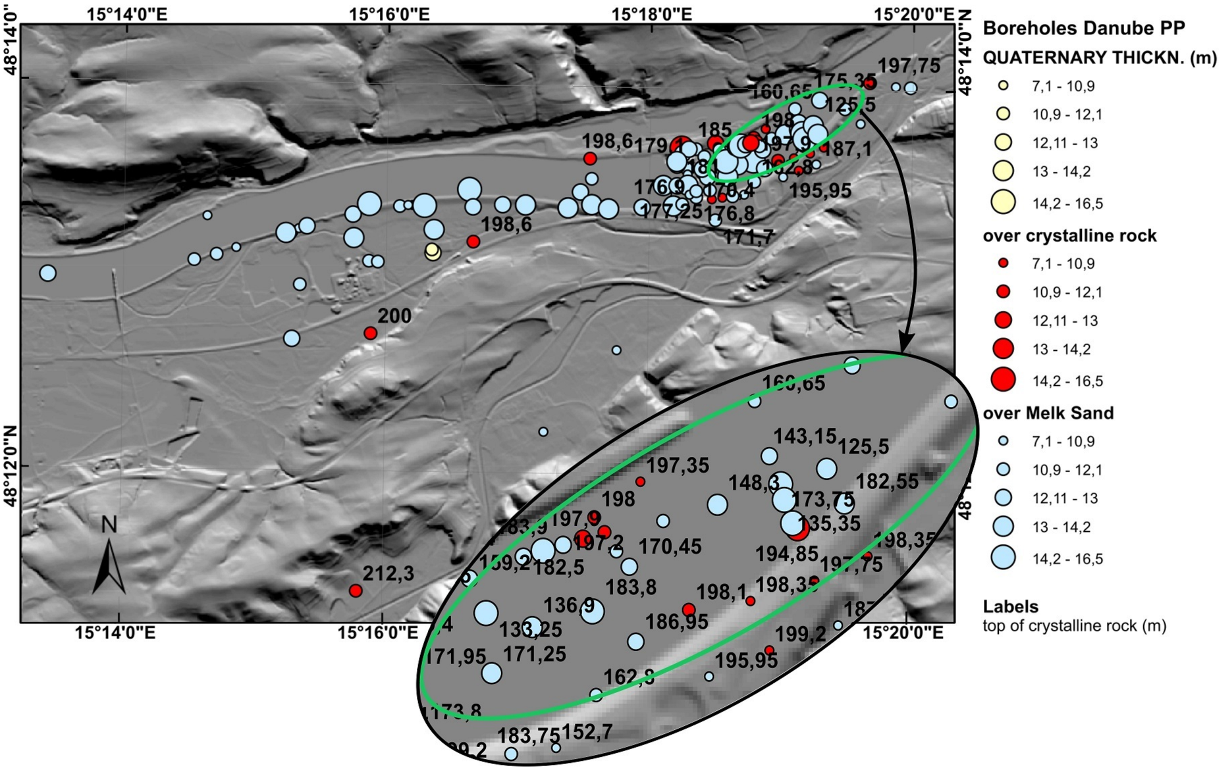

Figure 3.8.: Quaternary thickness (symbol size) from shallow boreholes in the vicinity of the hydropower plant Melk. Colours show lithology underlying Quaternary sediments. Anomalously low top elevations of crystalline rocks (labels) occur within green oval.

That could be interpreted as the Danube cutting into weakened (cataclastic) rocks. Lithologies of these rocks are discriminated in paragneiss, amphibolite and granulite for seven well locations on the valley floor in the geological map of crystalline rocks on the southeastern margin of the Bohemian Massif (Matura 1984); see locations of these and a geographical overview in the geological map (figure 3.2) in the previous chapter 3.1.1. As expected, highest Quaternary thicknesses are as well found at Danube level. Also observable are higher Quaternary thicknesses over Linz-Melk sand than over crystalline rocks, since the river could erode the soft sediments more effectively.

Figure 3.9 shows the Quaternary thickness again (symbol size), the colours are now outlining the elevation of the base of Quaternary sediments from low (blue) to high (red). The Quaternary base elevation expectedly decreases towards the Danube River.

For better comparability Quaternary thickness and base level data have been plotted as raster surfaces by nearest neighbour interpolation in ArcGIS (figure 3.10). The base level model seems quite smooth (decreasing heights from the DF towards the Danube), whereas Quaternary thickness varies especially along the supposed fault scarp.

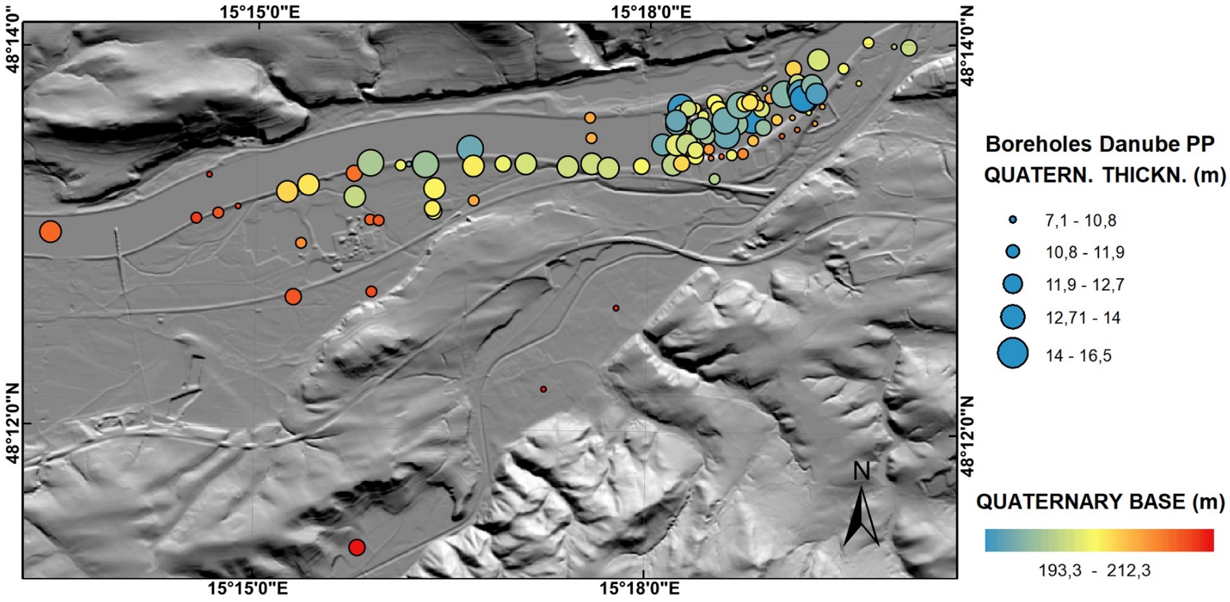

Figure 3.9.: Quaternary thickness (symbol size), colours showing elevation of Quaternary base from low (blue) to high (red).

Notable is also the low Quaternary height (brown) at a valley mouth, where an alluvial fan had been observed (chapter 3.2.2) and thick Quaternary deposits would be expected. A small scale releasing bend was suggested (around GEP3, figure 3.11), to explain varying thicknesses and base level heights, however high crystalline top elevation from the southernmost borehole does not support that theory – we would expect a graben here, not hard rock in a depth of only 12.1 m. Borehole data provides punctual information though, e.g. a crystalline boulder could affect the rock top height at a single well. The borehole could as well be located outside of the supposed graben-structure, and simply not be influenced by the small-scale releasing bend.

Geophysical measurements have been conducted to supply more detailed information crossing the DF, see locations in figure 3.11 and coordinates of starting and ending points of profiles in appendix (A.6). The high resistivity areas (red to orange, figures 3.12 and 3.13) can be regarded to image bedrock. A fault, where hard rock is adjacent to sediments, is therefore presumed at GEP1, two fault branches were interpreted at GEP2 and one to two branches in image GEP3. At the latter, the depression around 110 to 120 m of profile length could be the expression of the bending fault branch, suspected above to cause local subsidence, which also might influence the overlying sediments. Differentiation between sediments is challenging though, but borehole data provides subsurface information.

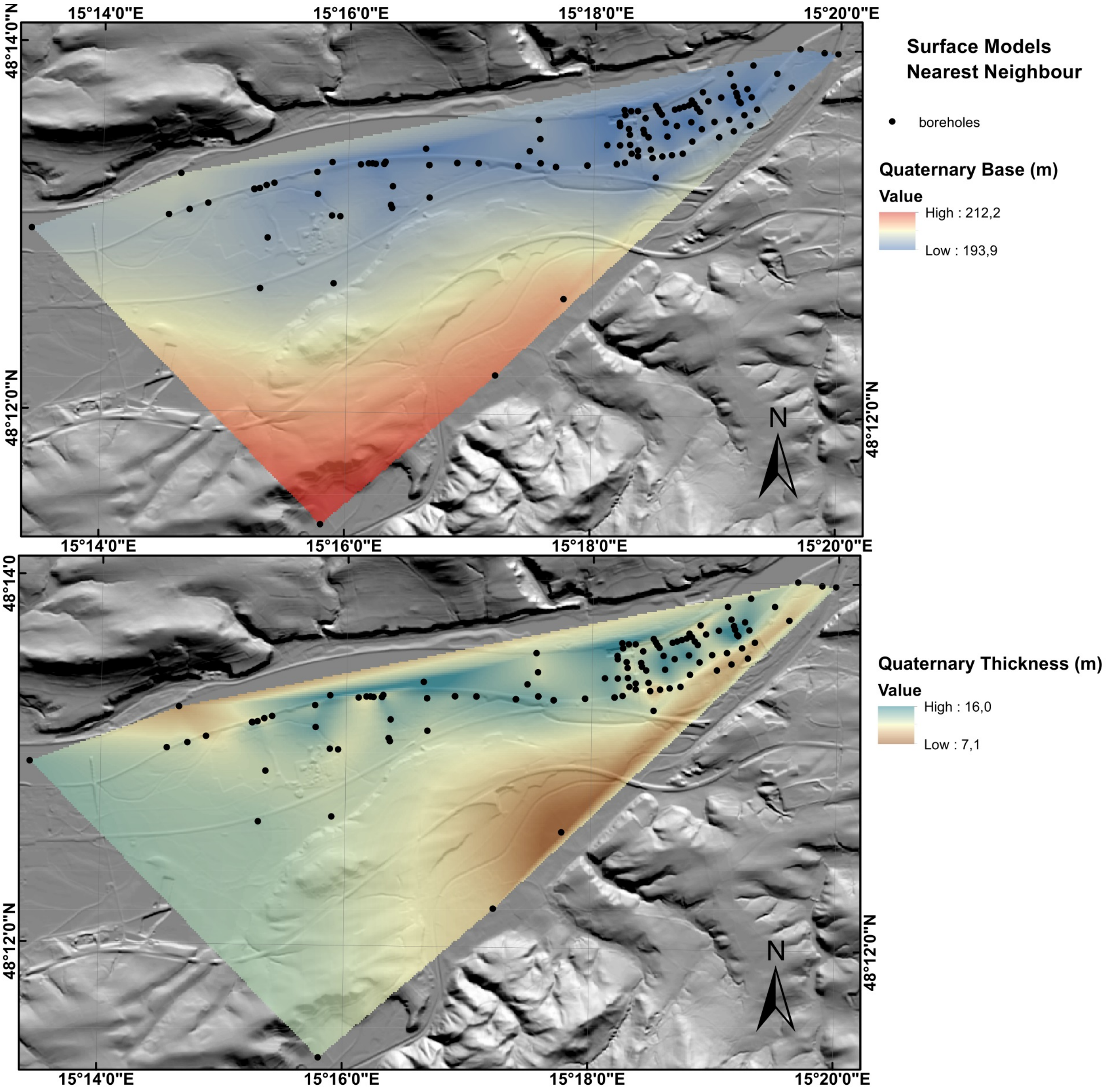

Figure 3.10.: Surface models of Quaternary base (top) and thickness (bottom) created of shallow borehole data in ArcMap.

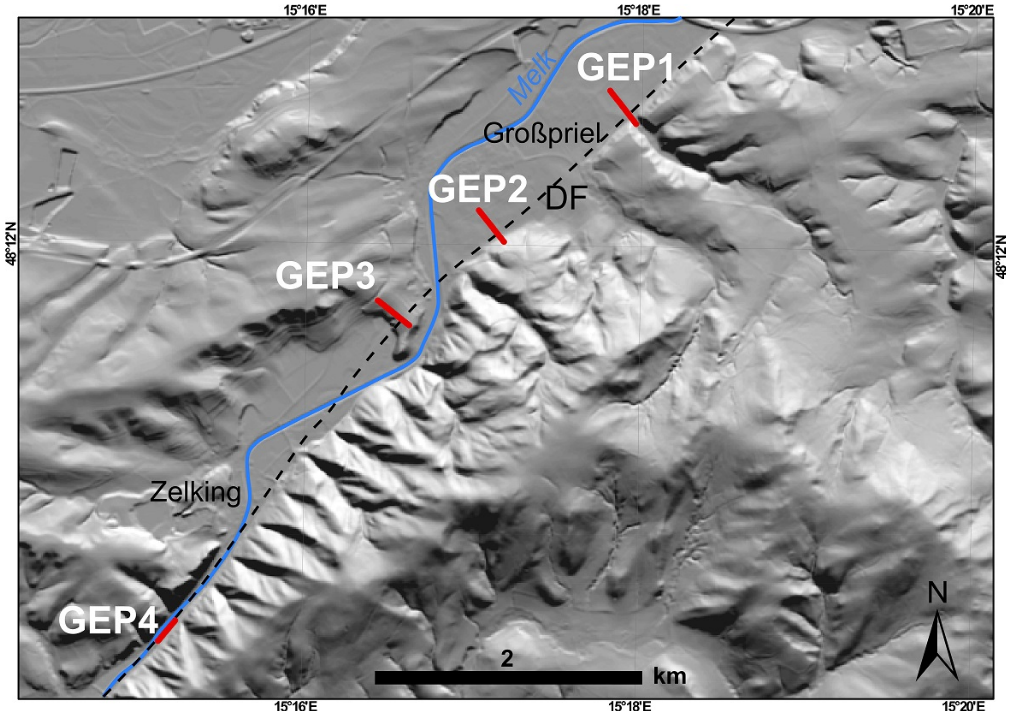

Figure 3.11.: Geoelectrical profile (GEP) locations at the Zelking fault segment southwest of Melk.

A well only a few metres from the ending point of GEP1 (long profile) found sand of the Linz-Melk Fm. at 7.1 m below ground level. Another borehole, close to GEP2 (long profile), reaches the Linz-Melk Fm. at 7.4 m below ground level. In both wells, Quaternary sediments superimpose Linz-Melk sands. At GEP2 Linz-Melk sands overlie hard rock, at GEP1 their thickness is interpreted to extend signal depth. As we know from trenching (chapter 3.2.2) at the detailed profile of the GEP1 site, the area with the low resistivity (dark blue) reflects clay (haugh), which might be found at the top 5 m from about 50 m of the detailed GEP2 profile as well. Surface geology as in the geological map (used in figure 3.2, '13') shows silt at the GEP2 profile location and the last third of the GEP3. Clay content and water saturation can cause resistivity variations within similar sediment layers. Anyway, the detailed GEP2 image seems to show subsidence of Quaternary sediments at a sub-vertical fault branch. The southernmost borehole, located approximately between GEP3 and GEP4, gives a Quaternary thickness of 12.1 m directly over crystalline rock. This is not supportive to the GEP3 image, but GEP4 reflects hard rock at about 13 m below ground level. As discussed above, the boreholes could be influenced by a rock bolder.

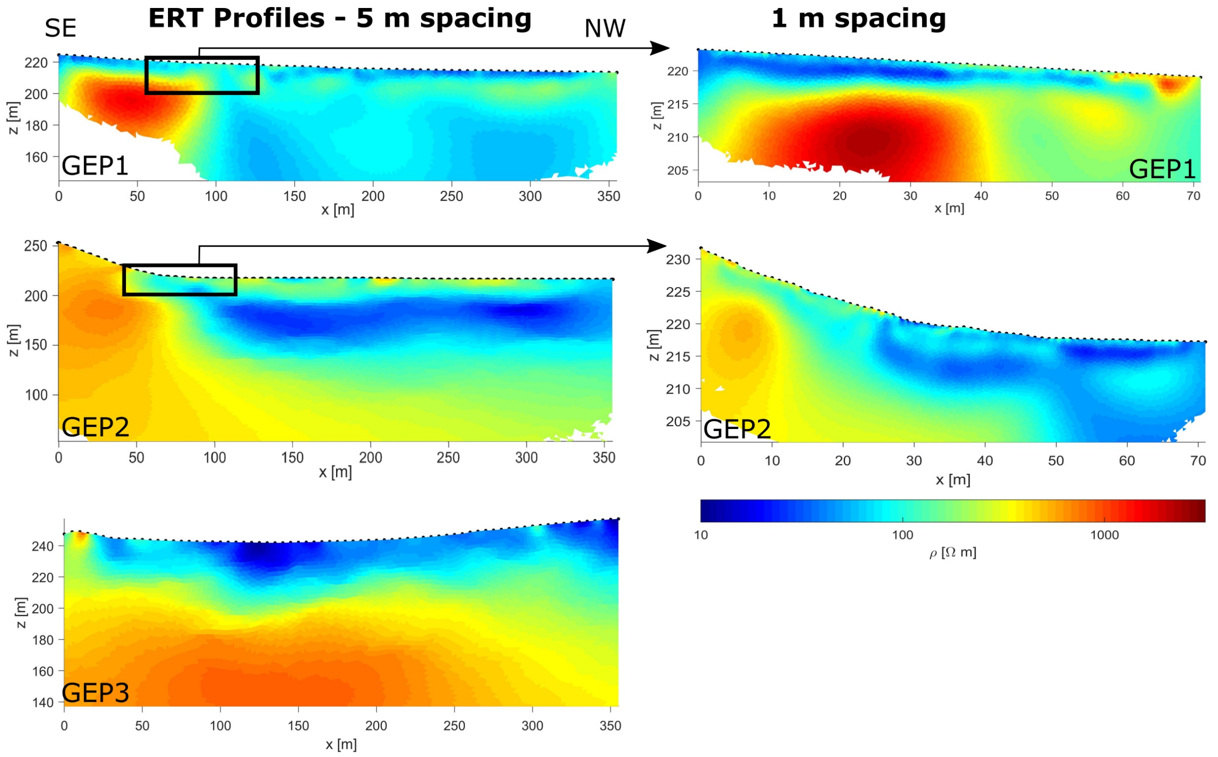

Figure 3.12.: ERT profiles GEP1-3 across DF. Starting points are not the same for long and short (detailed) profiles! See e.g. profile location of GEP1 in figure 3.14, in the following chapter 3.2.2 and coordinates of starting and ending points in appendix A.6.

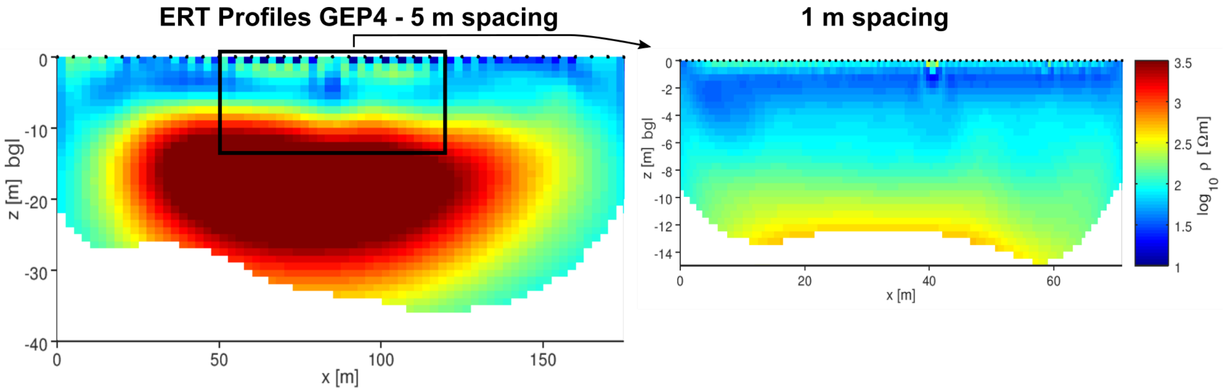

Figure 3.13.: ERT profiles GEP4 parallel DF, long profile left, short (detailed) profile right. Find coordinates of starting and ending point in appendix A.6.

3.2.2. Trench Site Großpriel (Melk)

The site in Großpriel (city of Melk) had been chosen for trenching due to accessibility of the supposed fault scarp as well as geomorphological and geophysical data from the Zelking segment, especially from ERT profiles on that spot (locations in figure 3.14, profiles with 1 m and 5 m electrode spacing). A geological and geographical overview of the trench location is given in figure 3.15.

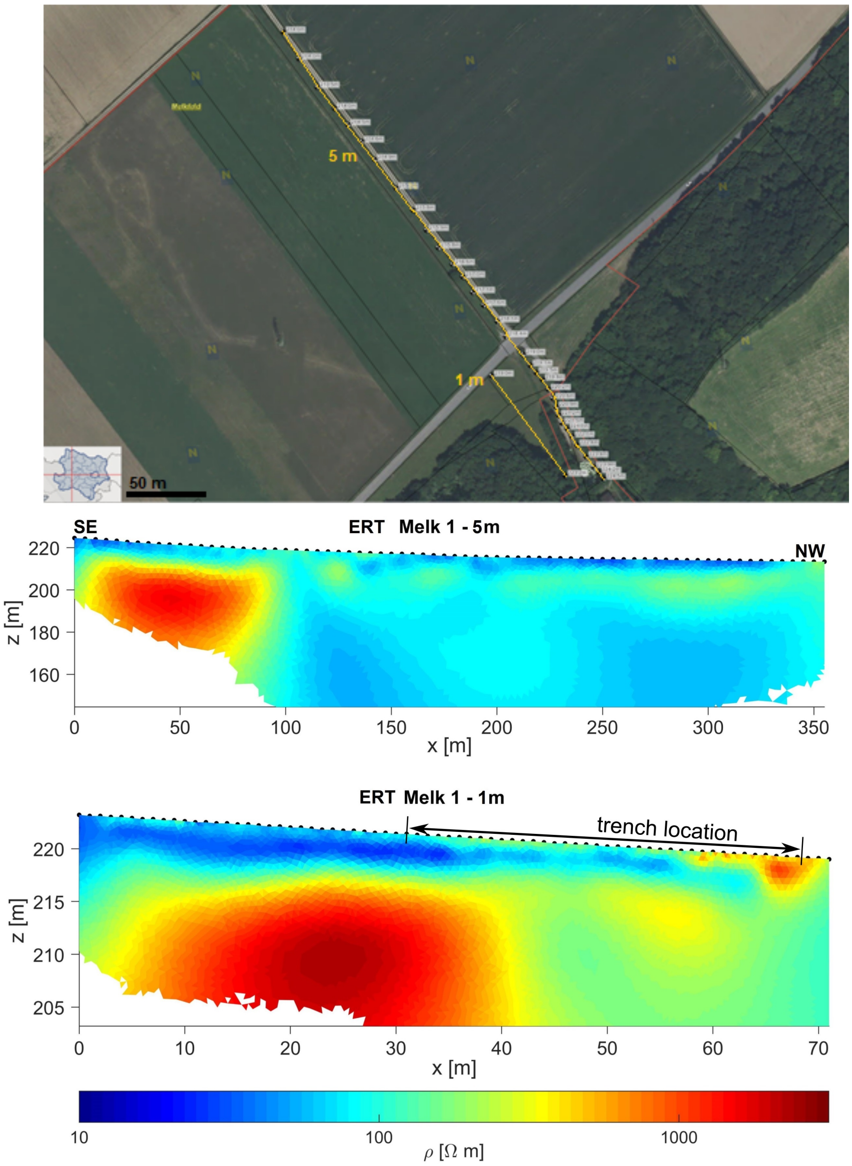

Figure 3.14.: Electrical resistivity tomography (ERT) profile locations at trench site (top) and results of inversion (center and bottom).

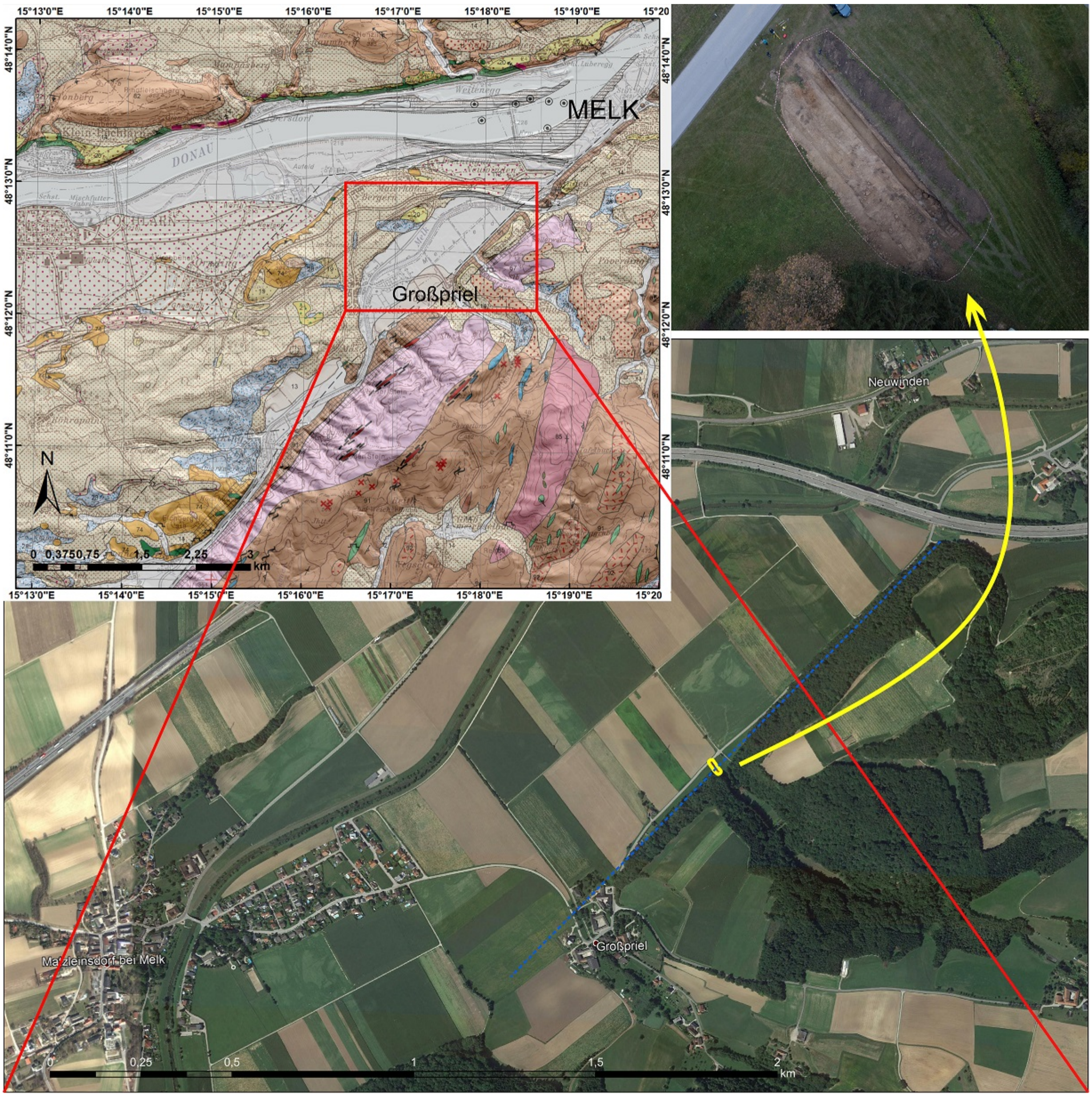

Figure 3.15.: Location of the trench in Großpriel (city of Melk); geological map of Melk (Kreuss and Linner 2018, top left), drone image (top right) by Joseph Hochwarter and satellite image (bottom) with blue stippled line indicating the DF.

Figure 3.16.: Trench site, person and 0.5 x 0.5 m wall grid for scale; direction of view is southeast.

Figure 3.16 shows a photograph of the excavation. To the right (northeast) a minor brook leaves the valley (as seen in figure 3.15 top right); an alluvial fan is observable across the street, far into the fields. About 700 m from the site the tributary flows into the River Melk, the River Danube is 2.1 km away.

The unconsolidated **sediments** in the trench start with rubble at the base ① (sketch figure 3.17, sediments in detail in figure 3.18). The mostly angular components vary in size from a few cm up to about 30 cm and primarily consist of granitoid rock, rich in biotite. Precipitations of iron and manganese oxides concentrate in the base level, but can also be found in overlying sediments. The layer above the gravel is a silty fine sand ②, subhorizontally laminated in sandy and silty layers of 1 to 3 cm in the back of the trench (from about vertical grid line 30 in figure 3.17). The grain size of the fine sand layers and the light yellow and grey colours showed similarities to sands of the Linz-Melk Fm., hence the sediment sample SED 1 was taken from the southwestern wall for comparison. OSL sample 1 is from that layer too, whereas samples OSL 2 and OSL 3 were taken from the overlying layer, which is not laminated, but siltier ③, interposed with lenses of gravel ④ and detrital grains of quartz and feldspar (grit). Gastropod shells have been found in the silt layer, most likely from recent species. It is a rather smooth transition from the sandy layer to the silt, also from the silt getting browner upwards to the

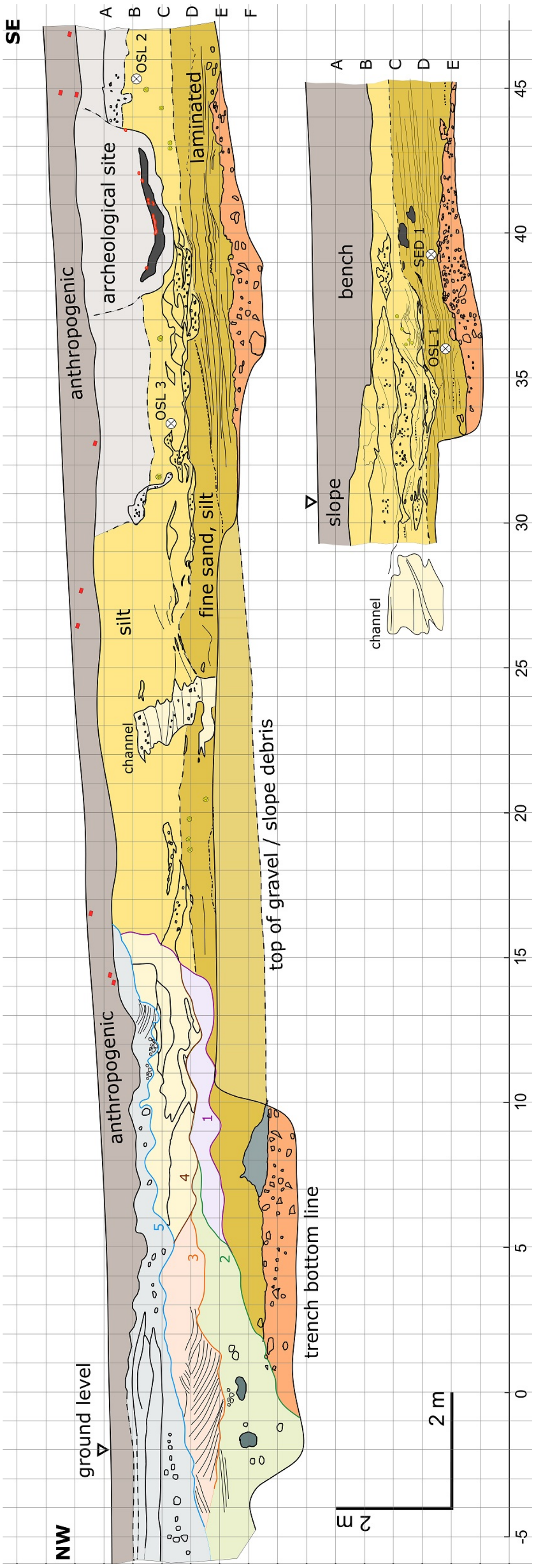

Figure 3.17.: Sketches of NE wall (top) and SE wall (bottom) of the trench in Großpriel.

Base rubble

Laminated fine sand

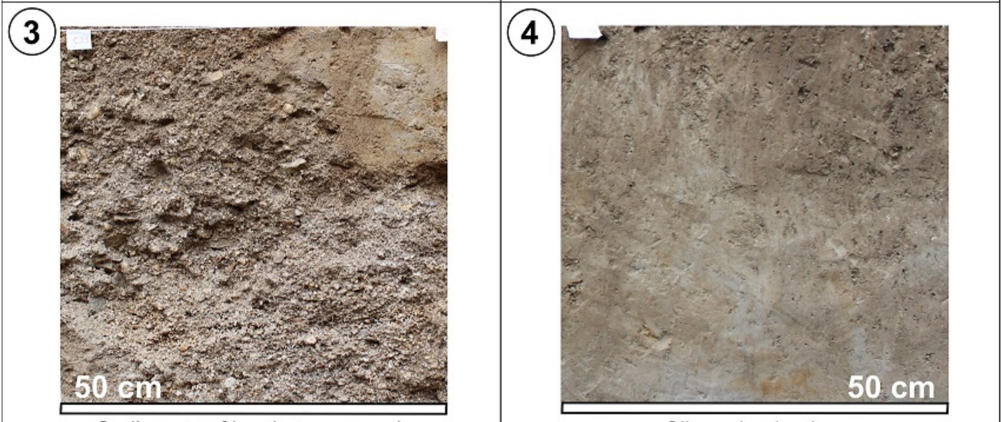

Sediments of local stream + grit

Silt, no lamination

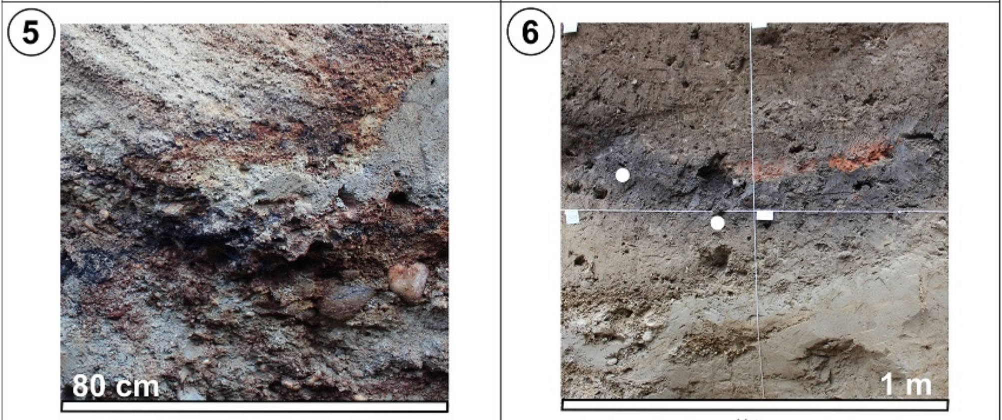

Erosional contacts + mud balls (flood)

Archaeol. site + ^{14}C sample locations

Figure 3.18.: Types of sediment in the trench, oldest ① to youngest ⑥, plus location (cf. wall grid, figure 3.17, all NE wall, but ② SW wall). ①: Base rubble, E–F38. ②: Laminated fine sand, C44. ③: Sediments of local stream + grit, C23. ④: Massive silt, devoid of lamination, B29. ⑤: Erosional contacts + grey mud balls, D1–E2. ⑥: ^{14}C sample locations indicated by white dots, taken from dark (charred) anthropogenic layer with fired clay (red), B39–C40.

anthropogenic top layer ⑥. In the first 10 m of the trench the fine sand and silt sediments are unconformably overlain by coarse-grained deposits ⑤. The rock material of the coarse sediments has not been analysed.

Granulometric analysis was carried out for sample SED 1 and bulk reference sediment from OSL 1 and OSL 2. Similar to the macroscopic classification, sample SED 1 was identified as fine sand (vc)(si)S, sample OSL 1 as silty fine sand (c)siS and sample OSL 2 as sandy silt (c)sSi (classification after Blott and Pye 2012). See table 3.3 for detailed grain size fractions, and pictures of microscopy in figure 3.19. The grains are mostly angular with very angular as well as rounded to well rounded components (e.g. fig. 3.19: Ⓒ), many grains are spherical. Rhizoliths form almost all components of the > 2 mm fraction and make up a great amount to 0.5 mm (fig. 3.19: Ⓐ, Ⓒ, Ⓔ). They are still common in the > 0.250 mm fraction. The coarser grain size portions also contain gastropod fragments (fig. 3.19: Ⓐ, Ⓔ). More and well conserved shells (two with a size of 1.75 mm and 1.125 mm) have been found in sample OSL 2. All samples contain idiomorphic mica (fig. 3.19: Ⓒ) and quartz grains, with mica being more present in the coarser fractions, and increasing mica content from sample SED 1 over OSL 1 to OSL 2. Heavy minerals (garnet, disthene, tourmaline,. . .) and even some euhedral crystals have been observed (fig. 3.19: possibly zircon in 1st quadrant of Ⓑ and quartz in Ⓒ).
Grain size parameters were derived graphically after Folk and Ward 1957 and via moment statistics (interpretation after Friedman 1962). See appendix for detailed table (A.8) and particle size distributions and histograms (figure A.3).

		sample SED 1			**sample OSL 1**			**sample OSL 2**		
grain size		**mass**		**cum**	**mass**		**cum**	**mass**		**cum**
> mm	**> Φ**	**g**	**%**	**%**	**g**	**%**	**%**	**g**	**%**	**%**
2	-1	0.319	0.35	0	0.716	0.76	0	0.366	0.42	0
1	0	0.052	0.06	0.35	0.302	0.32	0.76	0.885	1.01	0.42
0.5	1	0.288	0.31	0.40	0.415	0.44	1.08	0.881	1.00	1.42
0.25	2	11.813	12.83	0.72	5.176	5.51	1.52	4.139	4.71	2.42
0.125	3	47.361	51.45	13.55	25.252	26.87	7.03	10.832	12.32	7.13
0.063	4	20.315	22.07	64.99	30.543	32.50	33.90	20.099	22.86	19.45
0.0315	5	2.929	3.18	87.06	4.621	4.92	66.40	11.828	13.45	42.31
0.016	6	3.039	3.30	90.24	11.705	12.46	71.32	13.532	15.39	55.77
0.008	7	1.287	1.40	93.54	4.857	5.17	83.78	6.456	7.34	71.16
0.004	8	0.993	1.08	94.94	2.564	2.73	88.94	4.080	4.64	78.50
0.002	9	0.797	0.87	96.02	1.720	1.83	91.67	2.789	3.17	83.14
0.001	10	0.625	0.68	96.89	1.248	1.33	93.50	2.376	2.70	86.31
0.0005	11	0.613	0.67	97.56	1.181	1.26	94.83	2.582	2.94	89.01
0.00025	12	0.588	0.64	98.23	1.214	1.29	96.09	2.376	2.70	91.95
< 0.00025	13	1.042	1.13	98.87	2.462	2.62	97.38	4.700	5.35	94.65
		92.059	100	100	93.978	100	100	87.922	100	100

Table 3.3.: Grain size analysis of three sediment samples from trench site Großpriel.

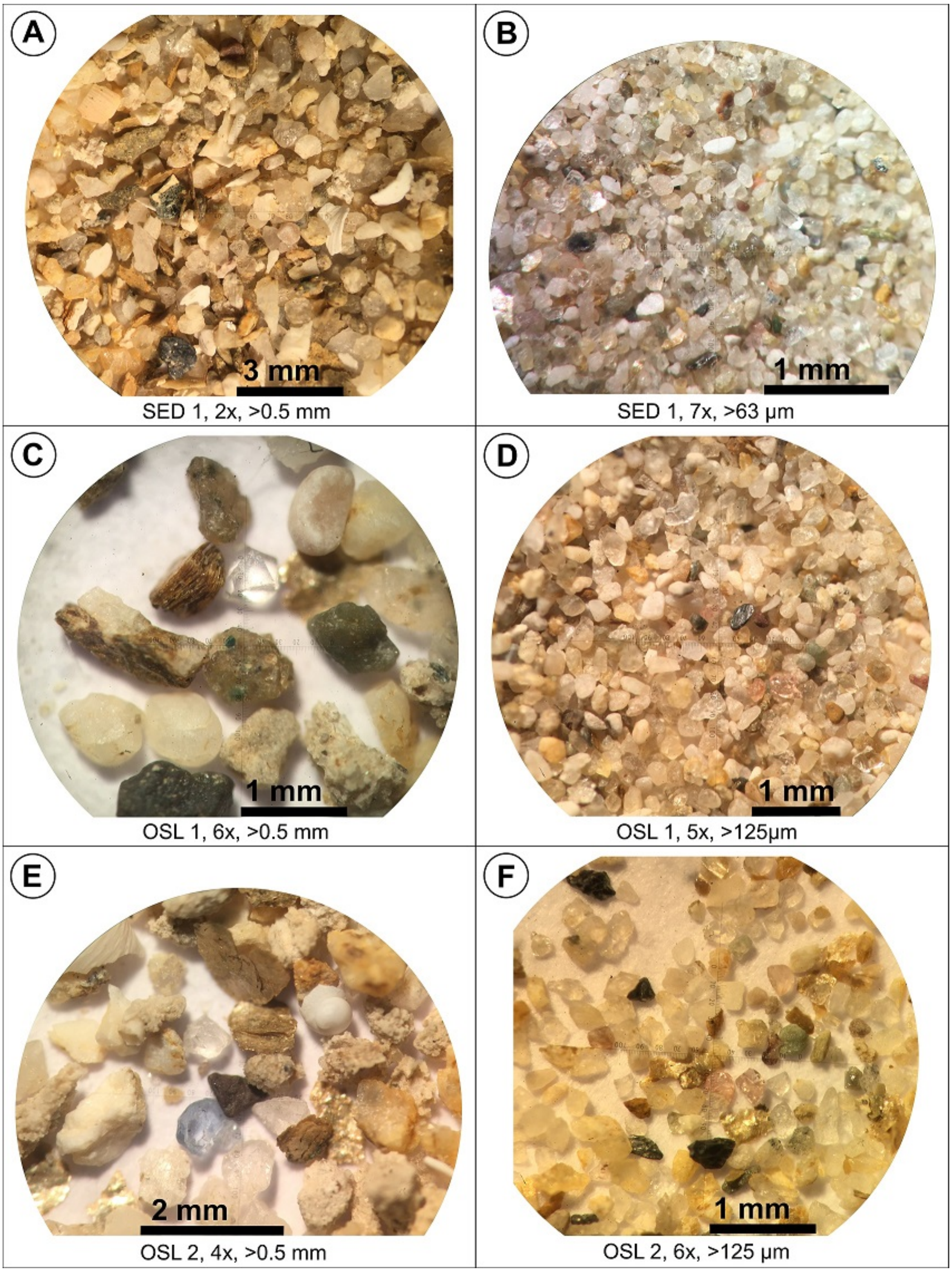

Figure 3.19.: Sediment samples under the microscope (reflected light), SED 1 (Ⓐ, Ⓑ), OSL 1 (Ⓒ, Ⓓ), and OSL2 (Ⓔ, Ⓕ). Left side shows pictures of the > 0.5 mm fractions, right side shows smaller grain sizes.

The **sedimentary environments** are interpreted as follows:

① The basal rubble consists of slope debris (angular crystalline rock components with intact biotite) interfingering with alluvial fan deposits of the tributary.

② The fine sands (samples SED 1 and OSL 1) actually seem, for some part, to be made up by sand of the Linz-Melk Fm. as microscopy and granulometry suggested. The sands were probably brought in by floods, the lamination indicating a low-energy flow regime then formed in (nearly) stagnant waters of the floodplain of the rivers Melk or Danube.

③ Angular grit and Pleistocene terrace pebbles were most likely transported by the local stream, since grit was found as in-situ weathering product of granite in the valley (cf. geological map in figure 3.2) and terrace gravel lies on top of both valley flanks. These sediments form the intercalated beds.

④ The massive silt (sample OSL 2) could reflect the transition from fluvial sedimentation at the site to aeolian loess deposition.

⑤ Five different channel fill successions could be distinguished (1–5 in figure 3.17). Erosional event number 2 in the sketch (figure 3.17, green) with rounded pebbles up to 15 cm and mudballs up to 30 cm indicates high stream energy and quick deposition. The flood was even eroding the base gravel. Number 3 shows cross stratification of sand and pebbles, whereas in number 5, the river was carrying larger components up to 15 cm again (orange and blue in figure 3.17).

⑥ The top layer was identified as anthropogenic due to brick fragments. This interpretation is supported by information from locals on the straightening of the stream in the mid 20th century. Also, an archaeological find is given in layer ⑥, read more below.

Prehistoric **Archaeological findings** have been described for the area of Melk e.g. by Coolen 2015 and Karl 1996, even in the closer surroundings of the trench site in Großpriel, Kollapriel and Zelking. A mould-shaped pit with charcoal and fired clay in the southeastern part of the trench (northeastern wall) has been noticed soon during excavating and then been reported as a find; see sketch figure 3.17 around vertical grid line 40 and sediment detail picture in 3.18: ⑥. In the southwestern wall some browned root channels have been spotted. The archaeological service investigating the site discovered ceramic shards, which are likely to date in the Late Bronze Age and/or early Hallstatt Period, as described in their report (Baumgart 2019). Two small pieces of pottery could be related to medieval times. Before closing the trench a bucket of the burnt material was taken, in order to find seed grains for archaeobotanical dating, since the site was interpreted to be a crop pit at that time. Instead of grains more pottery shards were revealed during sieving and even a burnt bone, probably from a human finger. This led to the reinterpretation, that the place would be a Hallstatt Age cremation site.

Carbon age dating of charcoal taken from grid boxes B 39 and C 39 revealed ages of 2330 ± 30 a BP (C 39) and 2420 ± 30 a BP for B 39, although with a broader calibrated date peak for the latter. Residual probability of an older age of sample B39 (around 2700 a BP) is given. Anyway, the ages of the charcoal samples correspond to the Latène Period (and Hallstatt Age for the lower probability of an older age), which still fits the former suggestion of a cremation burial site quite well.

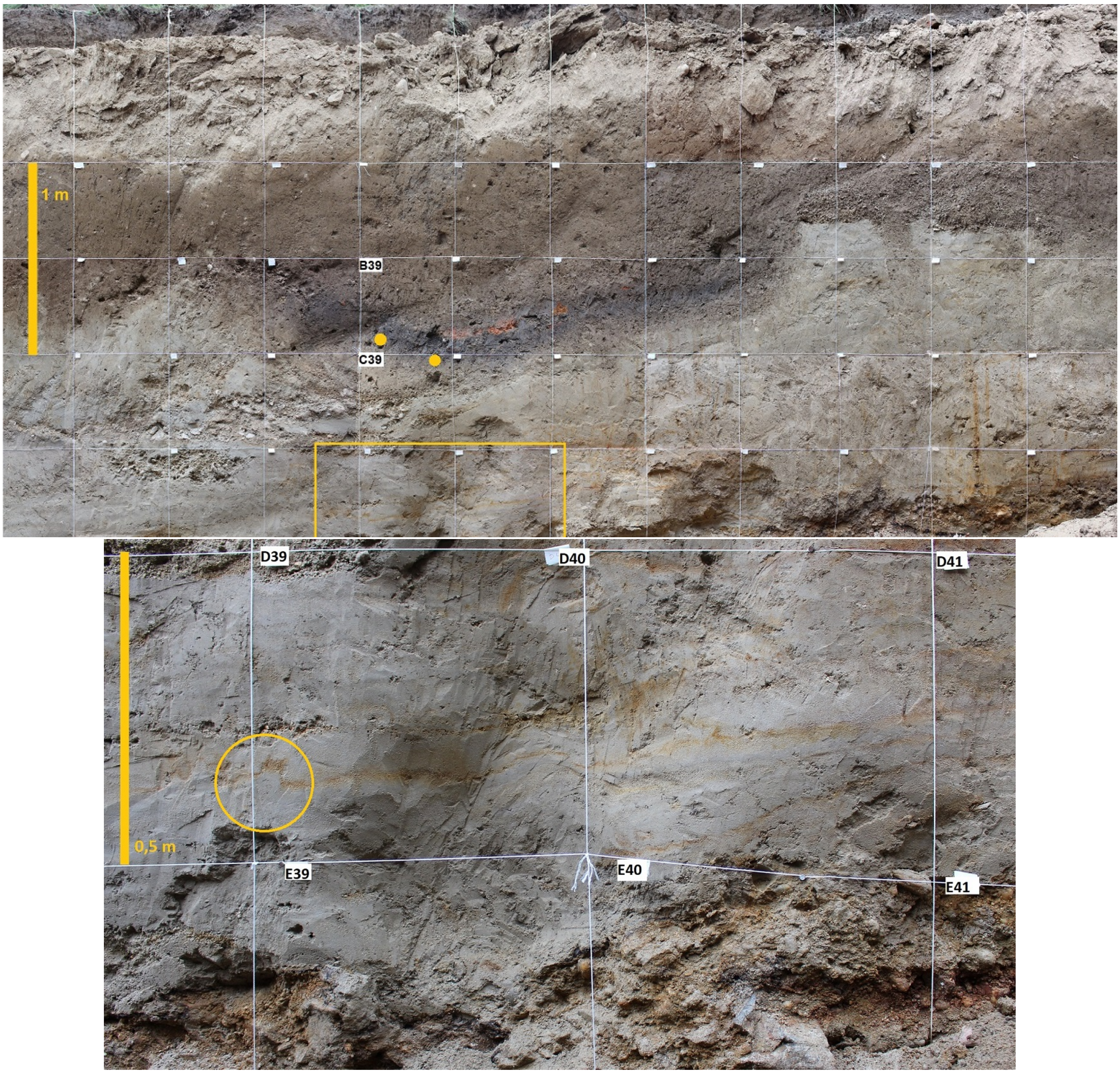

Figure 3.20.: Archaeological find on NE trench wall with ^{14}C sample locations as yellow symbols (top) and detail of folds in laminated horizon, in circle (bottom).

No clear **evidence of faulting** could be found in the trench, but some structures could indicate sediment disarrangement. The top of sedimentary unit ① (basal rubble) seems very planar and gently sloping from vertical grid lines 2 to 35 (see sketch in figure 3.17). From 35 to 40 on the SW wall and at about 40 on the NE wall a step from 25 to 50 cm can be observed, which might be of tectonic origin. However, further to the southeast, the top of the rubble is sloping downwards. Transgressional onlap of the laminated sands above that bump suits the interpretation of these sands as flood sediments. These sediments did not give hints of faulting, however they appeared loose on the NE wall. Some of the laminated 1 cm layers did seem folded (figure 3.20), but that could be the result of minor flow turbulence in the water-saturated fines after sedimentation. Again, this was observed only on the NE wall, but the gravel lenses, which supposedly are related to stream beds, accumulate near that area on both walls. Presumably, the step in the basal rubble is the only indication of tectonic activity, though.
Using teleseismic P-wave arrivals during active seismic recordings for near-subsurface investigations on a 400 m long line almost along the GEP1 ERT profile, Piana Agostinetti et al. (in preparation) claims, that a transition from shallow bedrock to a sediment-filled graben would be located between 120 m and 280 m from the starting point of the seismic as well as the GEP1 profile. That would be across the street in northwest direction from the trench and in greater depth, but is maybe visible on the 5 m-GEP1 ERT image too (section between 150 and 250 m with slightly higher resistivity in figure 3.14).

Compass measurements in hard rock close to the trench site revealed fault planes and fractures in angles of about 30 ° and 60 ° to the DF (figure 3.21). These could be antithetic and synthetic Riedel shear fractures induced by sinistral SW-NE strike-slip faulting. Similar larger-scale structures could have contributed to the formation of the bigger and broader valley compared to most of the other ones at the ridge of the Zelking segment, due to greater erodibility of the host rocks, resulting in higher sedimentation rates and an alluvial fan at the valley mouth.

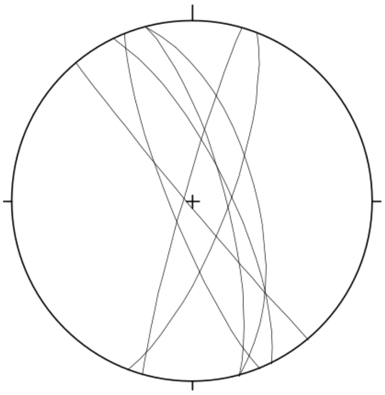

Figure 3.21.: Schmidt's net of fault planes and fractures in crystalline rocks in the surroundings of the trench site in Großpriel.

3.2.3. Langenlois Wolfsgraben

Langenlois is located at a releasing bend of the DF, southwest of the Paleozoic sedimentary rocks of the Zöbing pull-apart basin, that document early tectonic movements. Because of Pleistocene loess cover, the strike of the DF as the transtensional basin's northern margin and the FF as the southern margin cannot be followed nowadays – except for the FF at the Geißberg as bedrock-loess contact. See geological map and geographic overview with outcrops in figure 3.22.

As Hintersberger and Decker 2018 reported, in the Wolfsgraben, about 6 km southwest of Langenlois, small-scale faults crop out on a several metres high wall of loess deposits. The deep and narrow valley, terraced into narrow stripes, lies close to and probably within the southern margin of the basin. Badenian[3] conglomerates form the base of Pliocene to Pleistocene terrace gravel and Late Pleistocene loess cover.

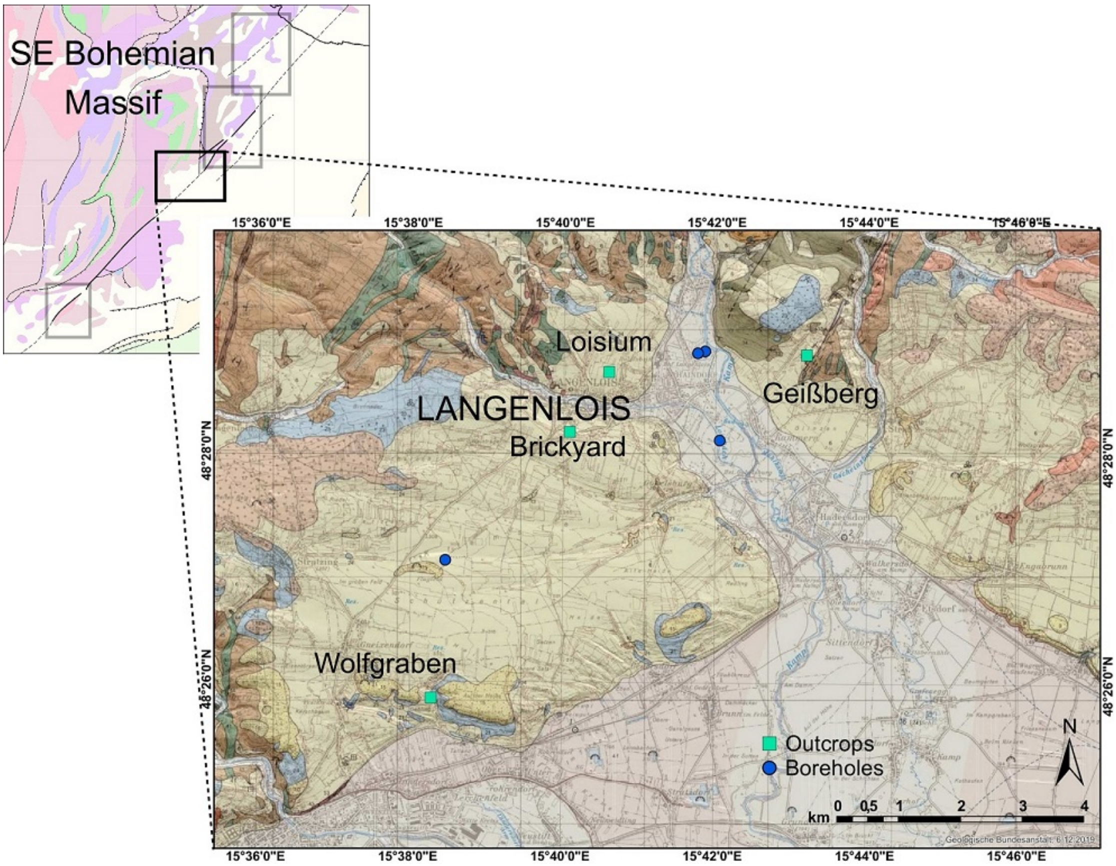

Figure 3.22.: Geographical overview of fault segment Langenlois including outcrops and locations of boreholes and local geology W. Fuchs et al. 1984.

---

[3] Regional chronostratigraphic Miocene stage of the central Paratethys area, 16 to 13.3 Ma

Re-examination of the site did not reveal slickensides (as shown by Hintersberger and Decker 2018 for a subvertical strike-slip fault). However, north-dipping faults with an offset of the loess lamination of about 3 cm could be located (figure 3.23). OSL ages were obtained at the bottom of the wall (W1) and from an outcrop one terrace above of it (W2), where no significant dislocations could be found. See both outcrops and OSL sample locations in figure 3.24. The vertical distance between the sample locations is about seven metres. The ages of 24.2 ± 1.9 ka at W1 and at 22.2 ± 1.8 ka at W2 date Late Pleistocene tectonic activity and demonstrate quick deposition of the several metres high loess sequence.

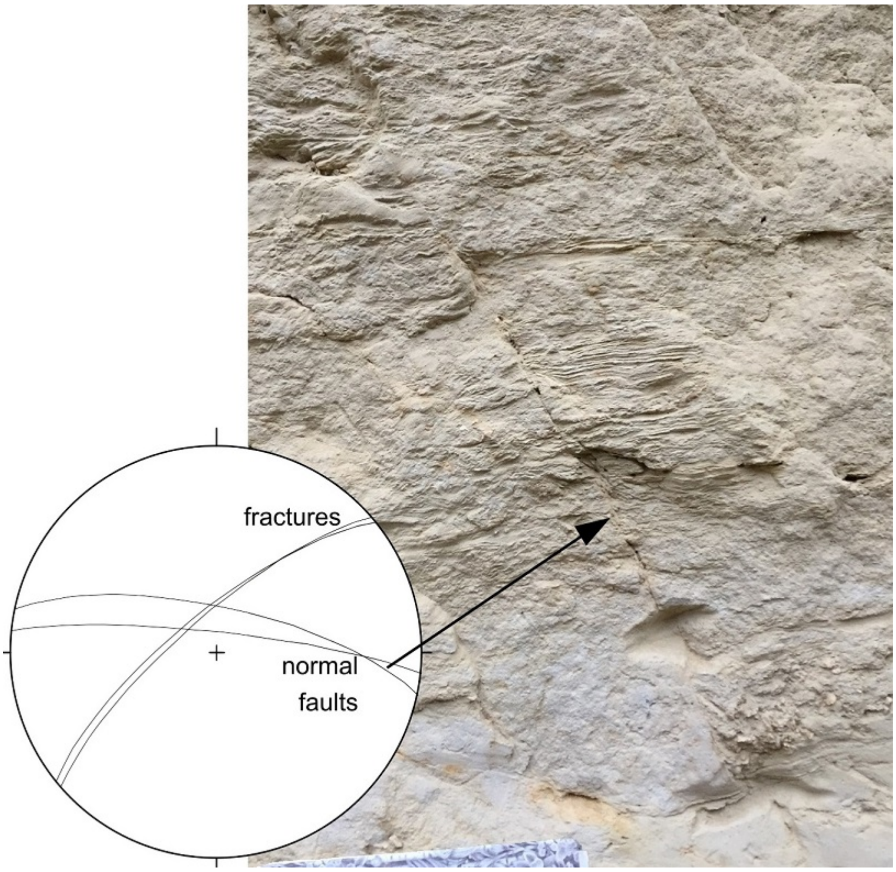

Figure 3.23.: Normal faults with 3 cm offset of laminated loess and stereoplot; direction of view is west, book for scale is 20 cm.

Figure 3.24.: Wolfgraben loess deposits with OSL sample locations (W2 on higher terrace); persons for scale, direction of view is southwest.

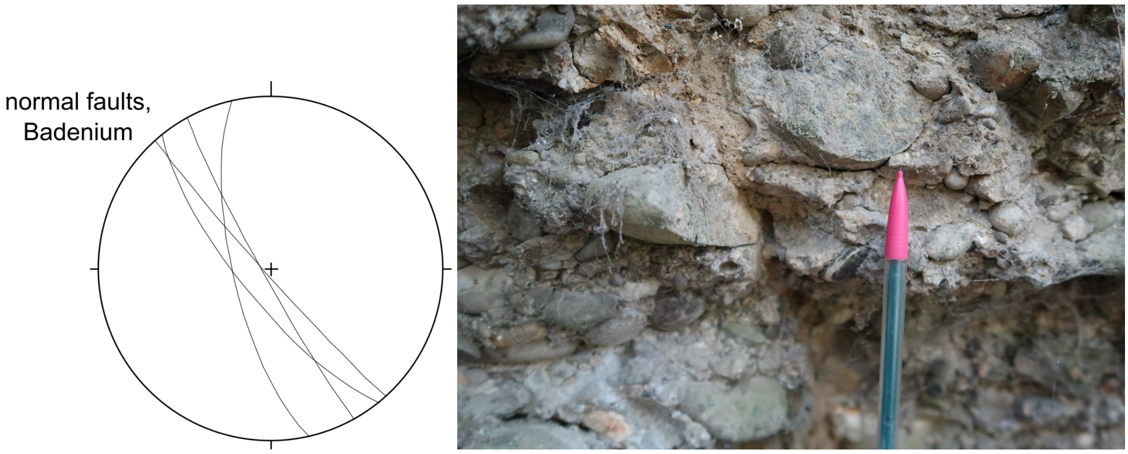

Figure 3.25.: Stereoplot (left) and photograph (right) of normal faults in nearby Badenian conglomerate at the Wolfgraben; direction of view is southeast.

3.2.4. Langenlois Former Brickyard

A former clay pit in Langenlois is also located within the supposed pull-apart basin. The up to 15 m high side walls permit insights on local stress conditions in Pleistocene sedimentary deposits. Figure 3.26 gives an overview of the pit and the further discussed faults, indicated in red.

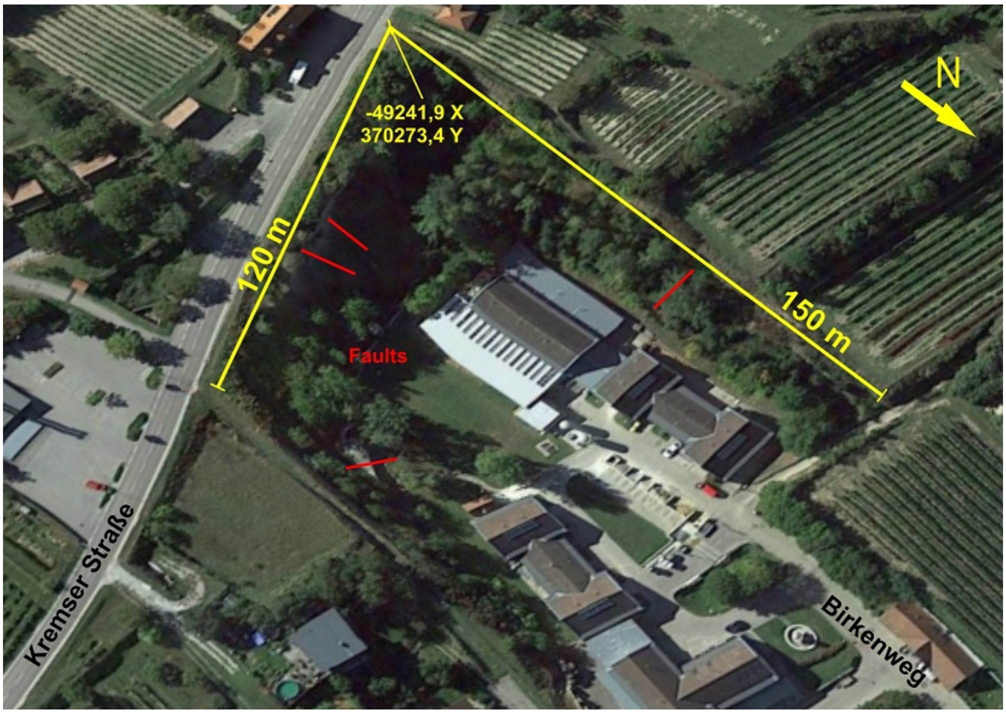

Figure 3.26.: Google Earth image from the former brickyard in Langenlois, faults indicated in red.

Thiel et al. 2011 mapped an approximately south-dipping normal fault in loess in the east-exposed (western) wall and acquired OSL age data from sedimentary profiles along the wall (sketch in figure 3.27). They were not investigating the Quaternary tectonics of the site, so neither a detailed profile nor OSL ages have been obtained around the fault-generated offset. It seems though, that at least the sedimentary layer dated at 41 ± 4 ka of their LB 5 profile further north can be compared with a stratum cut by the fault. Looking into these information at the brickyard in Langenlois exhibited a normal fault with dip to the south in the western wall, with laminae offset of 1.5 cm and a north-inclined (conjugate) fault in the eastern wall. Figure 3.28 shows the west wall fault – traceable to the uppermost layer (a) – and a detailed image of the white box (b), whereas c displays the conjugate fault system of eastern and western wall in the Schmidt's net. Since the dislocation in the west wall can be traced to the top layer, it would offset the 35 ± 2 ka loess as well and can therefore be regarded as younger than that.

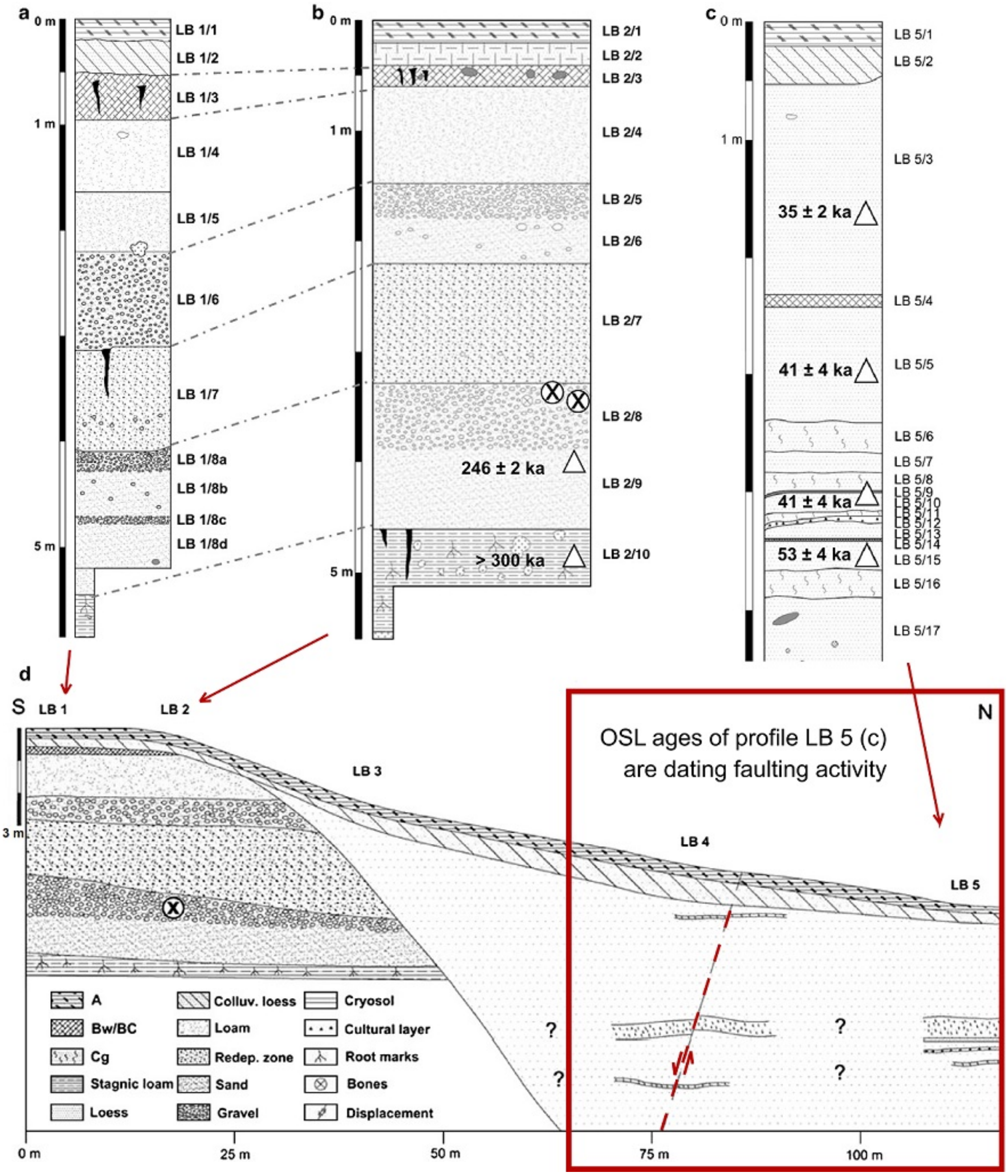

Figure 3.27.: Sketch and OSL-dated loess profiles from the W wall of the Langenlois brickyard, modified from Thiel et al. 2011. The fault indicated in the red box is shown in figure 3.28.

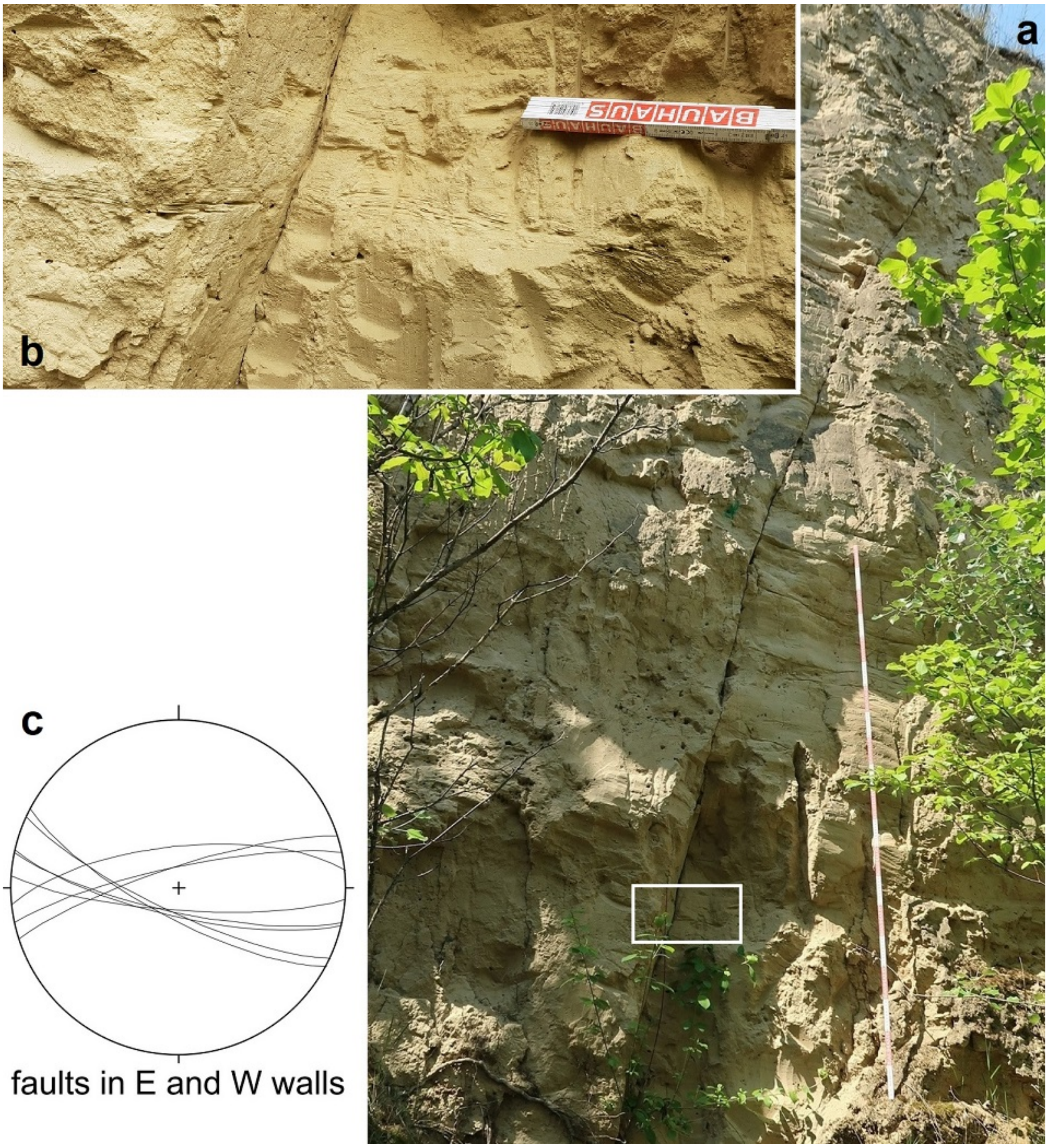

Figure 3.28.: a) W wall fault of clay pit Langenlois (folding rule is 2 m),
b) detailed photograph (white box in a) with slickenside left of fault,
c) stereoplot of normal faults in E and W walls.

East- and west-dipping faults and fractures in the southern wall have been found additionally. A photomosaic (not orthorectified) of faults in the southern wall is given in figure 3.29. The white box marks the area of the sketch of figure 3.30, also showing the compass measurements of the southern wall in the Schmidt's net. The sketch points out the dissection of the light clayey silt layer. Those faults lie within fluvial deposits, since brown cross-bedded sands and gravels unconformably overlie the 1.6 m thick red silty sand. Both, the red silty sand and the clayey silt layer taper to the west and disappear after 8 to 9 m. The same section had been discribed and sketched by Fink et al. 1978, see figure 3.31.

Thiel et al. 2011 described the transition from older fluvial sediments in the south to Late Pleistocene aeolian loess in the north (figure 3.27). The base cryosol of profile LB 2 and of the sand above it date at > 300 ka and 246 ± 29 ka. So all faults in the former brickyard cut Pleistocene deposits, the probably older southern wall faults indicate E-W extension though, whereas the young ones in the west show N-S extension.

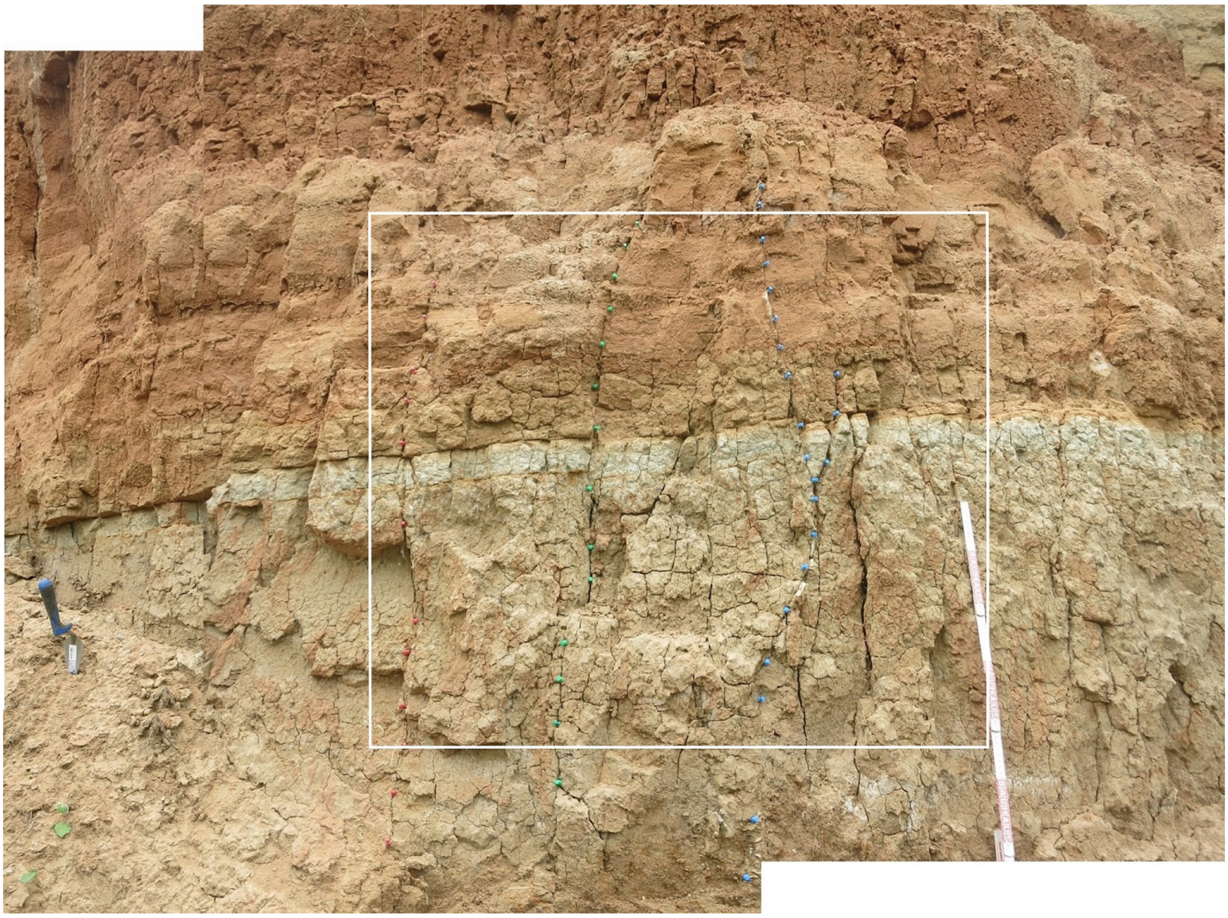

Figure 3.29.: Faulted sediment layers in S wall of clay pit Langenlois, white box shows area of sketch (figure 3.30); trowel and folding rule for scale.

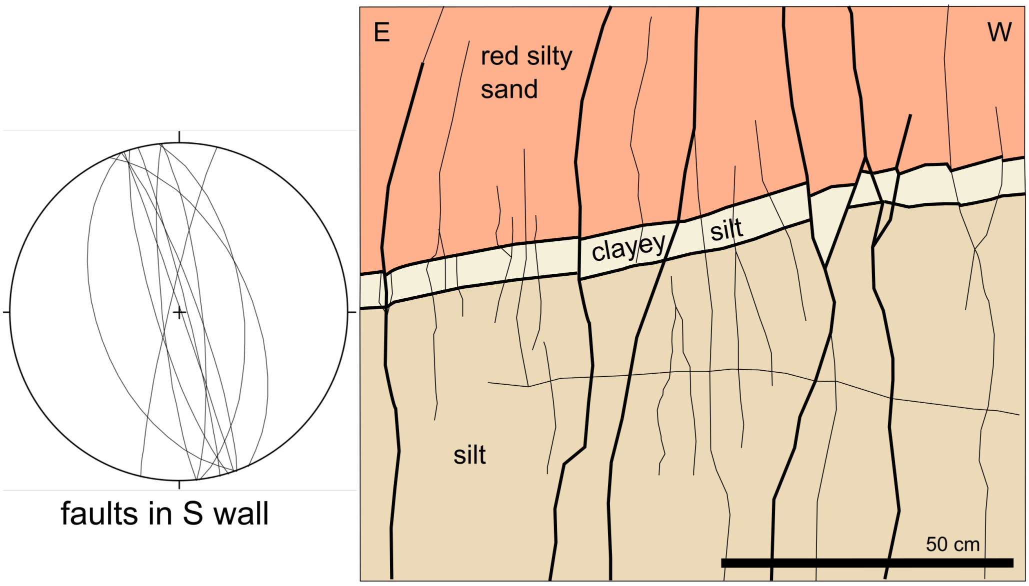

Figure 3.30.: Fault plane stereoplot (left) of and sketch of dissected light clayey silt layer (right) in S wall of brickyard Langenlois (photograph in figure 3.29).

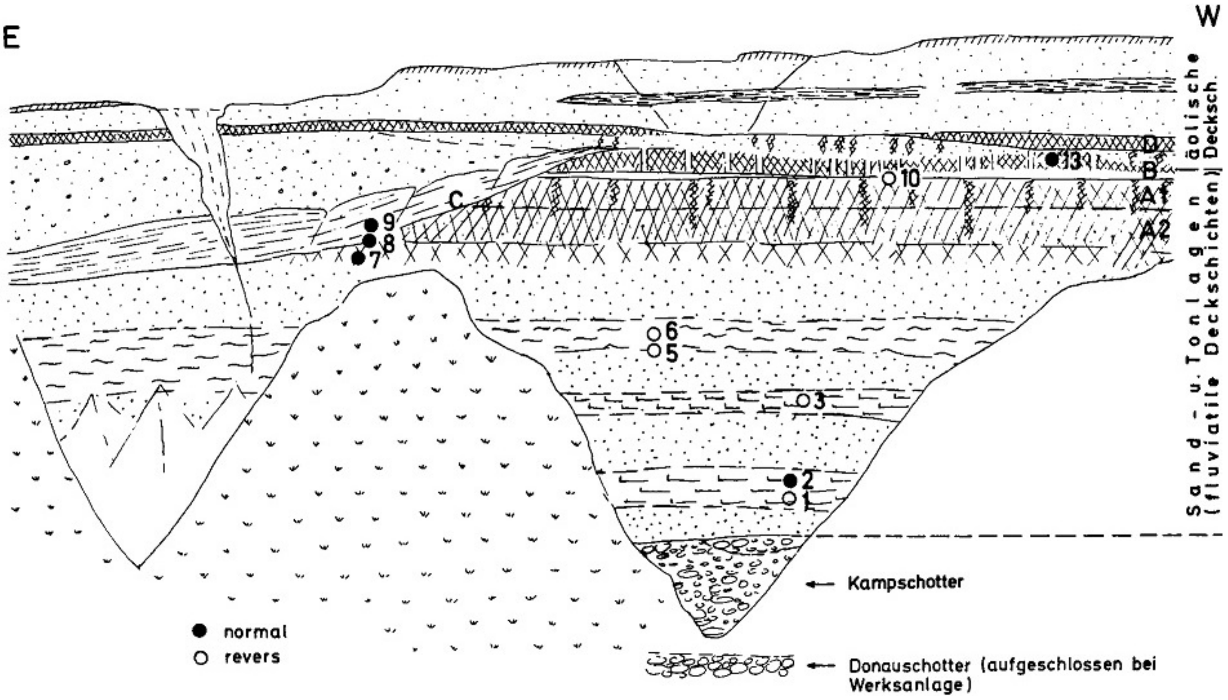

Figure 3.31.: Sketch of S wall by Ludwig Piffl in Fink et al. 1978.

3.2.5. Langenlois Loisium

The Loisium winery and spa is located about 1 km northeast from the brickyard Langenlois and also lies within the transtensional graben structure at the releasing bend between DF and FF. A construction pit for an annexe was excavated in early 2020 and we were informed by the Geological Survey of Austria[4], that normal faults offset about 2 m of sand and clayey silt. See figure 3.32 for a map of the area and sketches of the pit at Loisiumallee-Sonnenstraße and a second one in the south, shortly discussed later. The base of the about 30 x 40 m large northern excavation had partly been concreted and the walls sloped above 2 m, when the site was investigated.

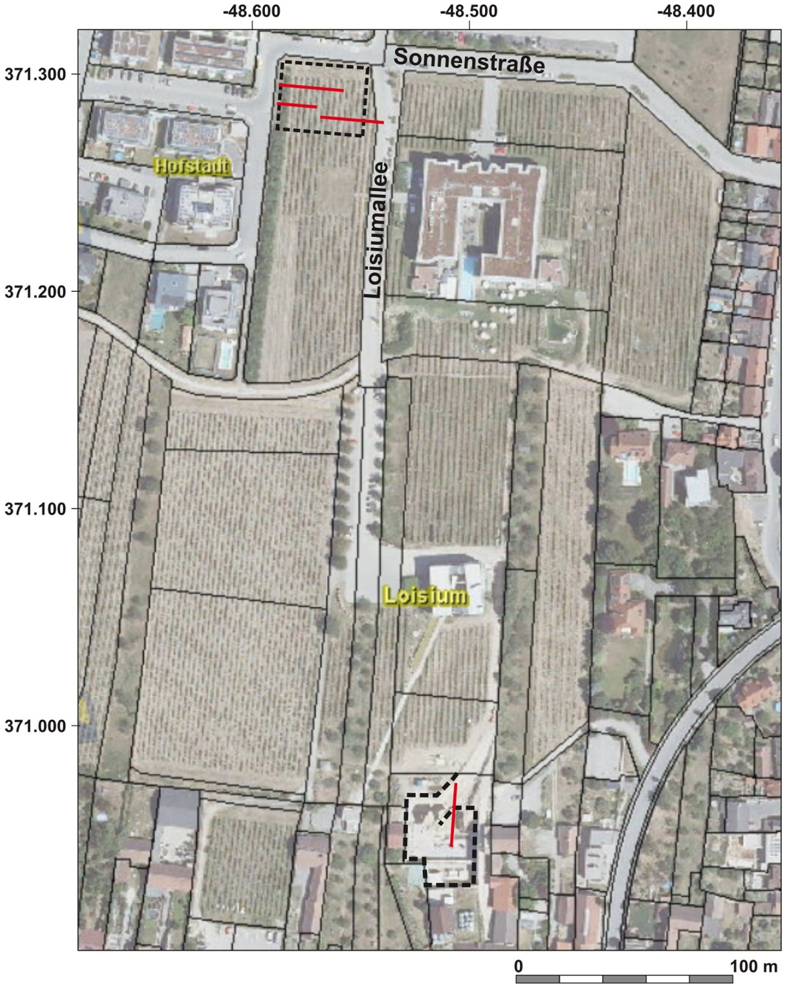

Figure 3.32.: Map of the Loisium area, two constructions pits.

---

[4] Dr. Reinhard Roetzel, former Head of Department Sedimentary Geology – Neulinggasse 38, 1030 Wien

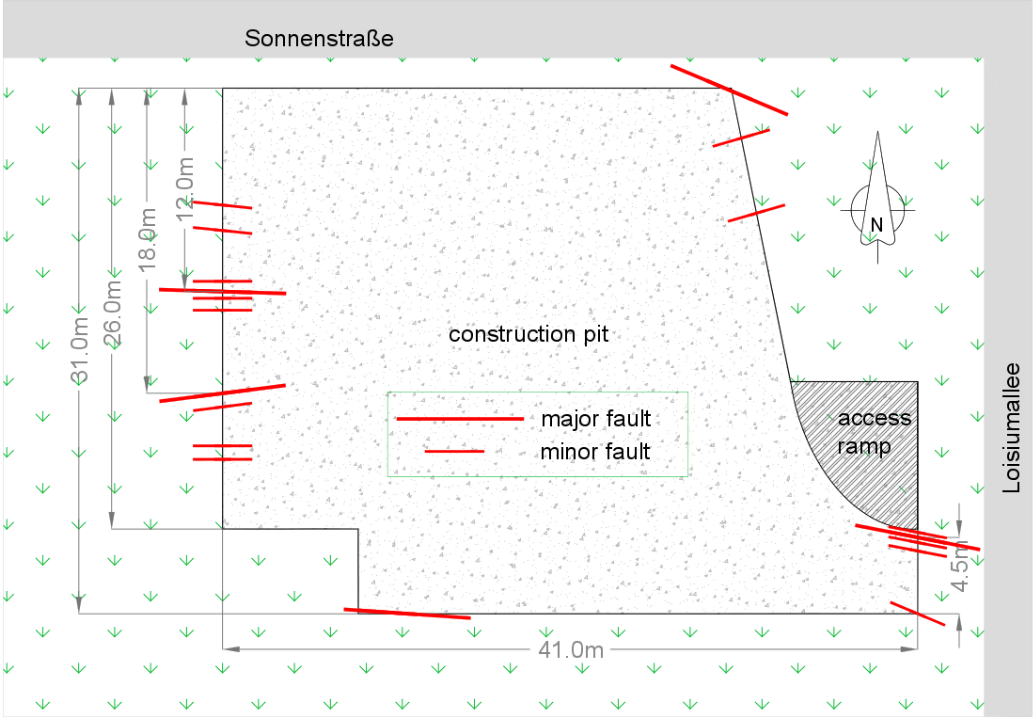

Figure 3.33.: Plan view of building pit with faults plus approximate strike.

Figure 3.33 illustrates the pit in plan view with outline of faults and approximate strikes (distances between faults and corners at intersections of fault planes with ground level). See a photograph and a sketch of the northern wall in figure 3.2.4 with OSL sample locations and numbering of the **sediment layers**. Coarse gravel ①, sometimes with rock components of 10 cm, forms the basement of the northern and eastern part at least – probably not visible along the southern wall due to a slight plunge to the southwest and faulting activity. Fluvial sediment layers of dm-thick sands with fine pebbles and cm-thick pelitic layers ② interposing the sands are prominent all over the pit; cross-stratification was observed along all side walls, with exception of the northern wall. A tapered and faulted grey clayey silt layer ③ with a thickness up to almost 3 m crops out in the south and west. The yellow sand ④ was only found at the western wall, and aeolian loess ⑤ often forms the uppermost deposit under the topsoil ⑥ or as a topsoil component.

The **northern wall** shows the best-exposed undisturbed succession. Five OSL samples had been taken in the corner to the west, but dating is not completed yet. See figure 3.35 for OSL sample locations of the northern wall and other OSL sample locations in figure 3.42).

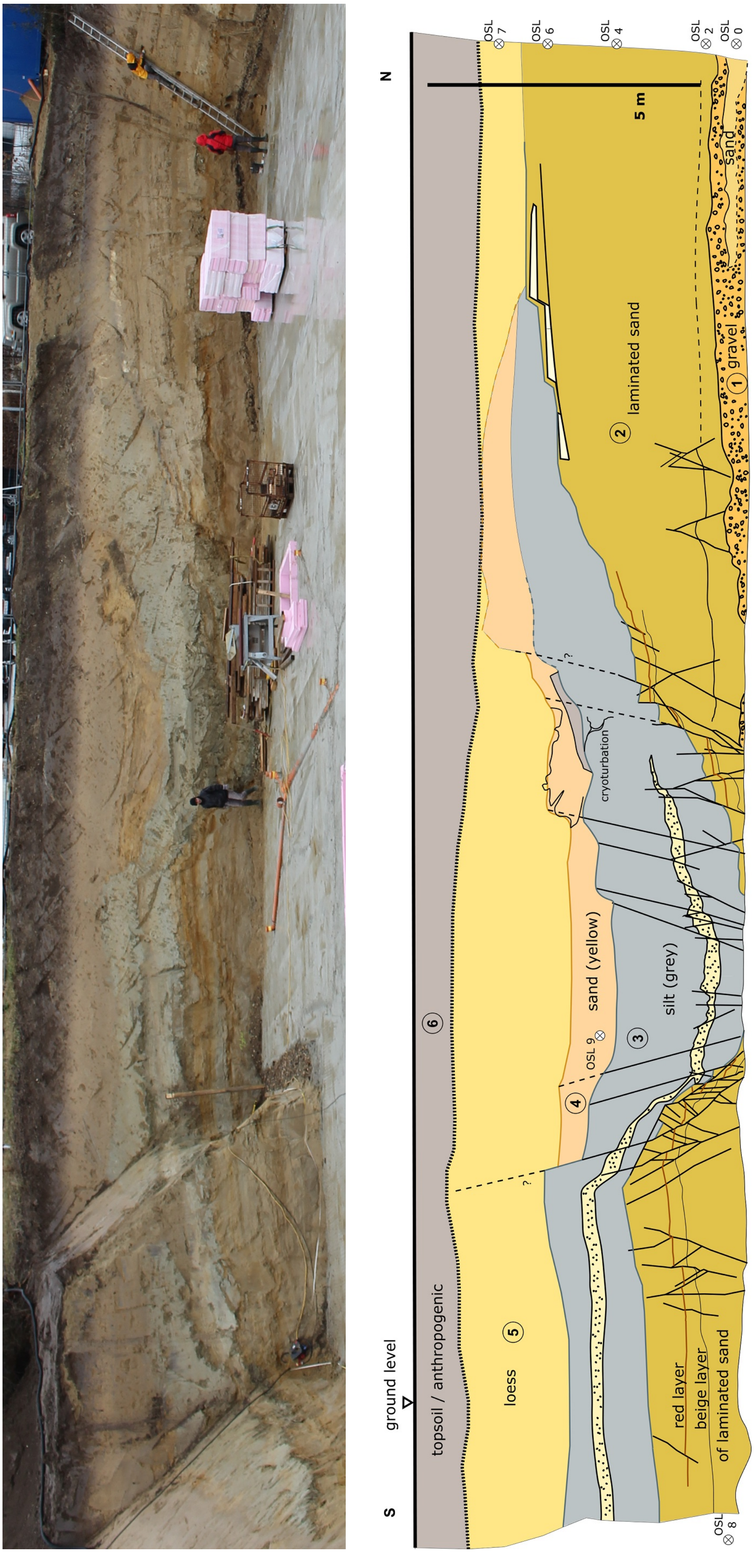

Figure 3.34.: Photo and sketch plus OSL sample locations, W wall of construction pit.

Figure 3.35.: OSL sample locations 0, 2, 4, 6, 7 at the northwestern corner of the Loisium construction pit.

Several **faults** with offsets of some centimetres to over 2 m could have been located. In the northeastern corner a distinct NE-dipping normal fault produces displacement of about 40 cm (figure 3.36). The structure seems V-shaped due to the three-dimensional cut of the fault plane in the corner. Along the **eastern wall** two conjugate systems similar to that fault (at 3 and 7.5 m distance from the northeastern corner) also lead to an offset of the lowermost-exposed layers, including the basal gravel and resulting in minor displacement.

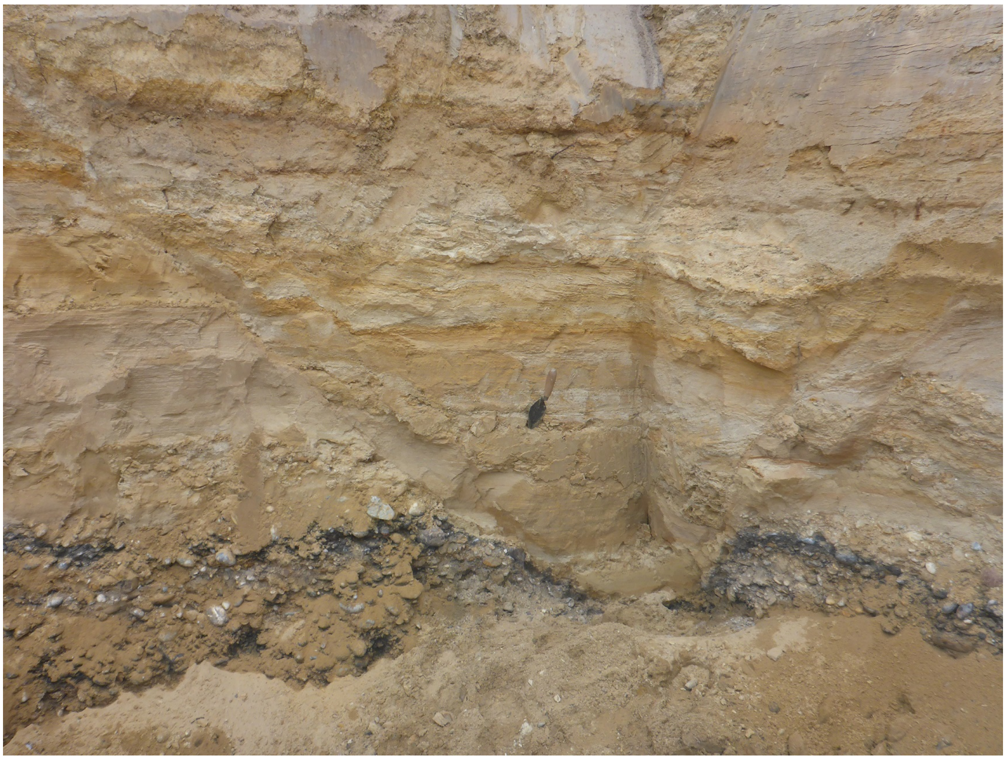

Figure 3.36.: NE-dipping normal fault in NE corner of the Loisium construction pit, trowel for scale, photograph by Reinhard Roetzel.

Further to the south, trough cross-bedding determines the unfaulted strata (figure 3.40) as far as about 18 m from the northeastern corner, where the access-ramp starts. Right after the ramp, 4.5 m from the southeastern corner, these layers are displaced considerably by a set of normal faults (figure 3.37). The maximum offset of the basement gravel reaches about 60 cm, but the most unusual structure can be found within the subsided sands in the middle of the photograph. Subsided strata would be expected to be upward concave or to stay horizontal, as in the northeastern corner (figure 3.36). Here, the layers seem to bend downwards at the northern (left) major fault, which is considered as an effect of prehistoric earthquake activity. The sediments are likely to have filled a fracture at the fault. Soil liquefaction and flowing back of sand into a resulting void also could have happened. Such seismogenic structures of the observed size correspond to an intensity $I \approx$ V-VII according to the ESI-07 scale (Michetti, Esposito, et al. 2007, Serva et al. 2016). A thinner fracture at the southern fault (right) with light sediment infill could support the interpretation of paleoseismic evidence, it's lateral continuity had not been checked though. The structures seem to end at a siltier layer overlying the sands, which would lie underneath the sampled layer (OSL-8) of the southern wall. The sand overlying the base gravel however is corresponding to the one at the northern wall, hosting the luminescence sample location OSL-2. The result of dating will therefore give an approximate age of the assumed earthquake activity. Another sub-vertical fault to the north could be observed around that spot and several ones parallel to the major fault in the south (plus minor conjugate faults) further to the southeastern corner, where the basal gravel is offset similarly as discussed above, but with less displacement.

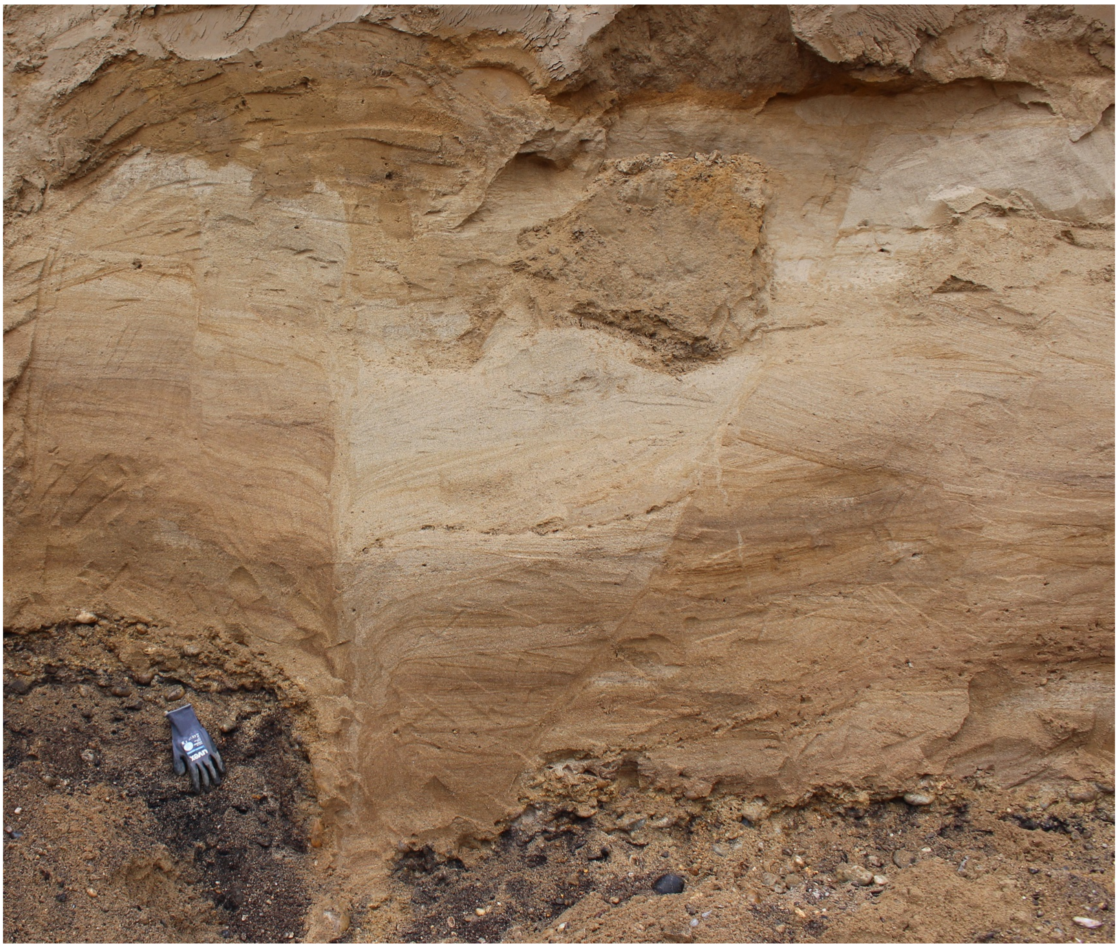

Figure 3.37.: Faults close to SE corner of the construction pit, glove (size 8) for scale.

The **southern wall** shows tabular cross-stratified sand, some layers laminated horizontally, but all markedly dipping to the southwest – 3D-view due to missing corner in the southwest (sample for OSL dating from that step of the southern wall in figure 3.42). The wedge-shaped layer of grey clayey silt encloses a bed of fine gravel. A sub-vertical slickenside with roughly vertical striation could be detected in the lowermost section of the silt, adjacent to the primarily underlying sands (figure 3.38).
Figure 3.34 shows the tapered grey silt layer at the southern wall (area of slickenside) in the left of the photograph, and the **western wall**, where the sands as well as the

thicker grey silt bed continue laterally. Here these sediments are faulted considerably. The minimum offset of the light fine gravel is 2.1 m left of the fault zone and 1.2 m to the right. See the left (southern) side of the fault zone in detail in figure 3.41. The light fine gravel can be traced from right of the spirit level (1 m in length) to the upper left corner of the picture. Figure 3.34 shows the tapered grey silt layer at the southern wall (area of slickenside) in the left of the photograph, and the western wall, where the sands as well as the thicker grey silt bed continue laterally. Here these sediments are faulted considerably. The minimum offset of the light fine gravel is 2.1 m left of the fault zone and 1.2 m to the right. See the left (southern) side of the fault zone in detail in figure 3.41. The light fine gravel can be traced from right of the spirit level (1 m in length) to the upper left corner of the picture.

Figure 3.38.: Slickenside with lineation, S wall of building pit, glove (size 8) for scale.

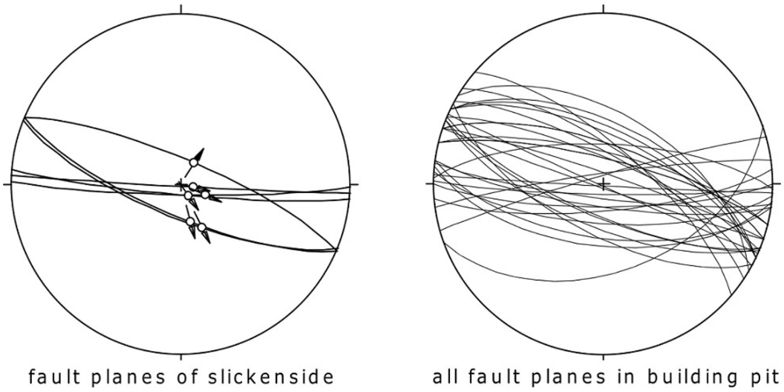

Figure 3.39.: Schmidt's net of slickenside (S wall) left; all measured fault planes right.

Figure 3.40.: Cross-stratified gravel and sand at the E wall of the Loisium building pit, trowel for scale, photo by Reinhard Roetzel.

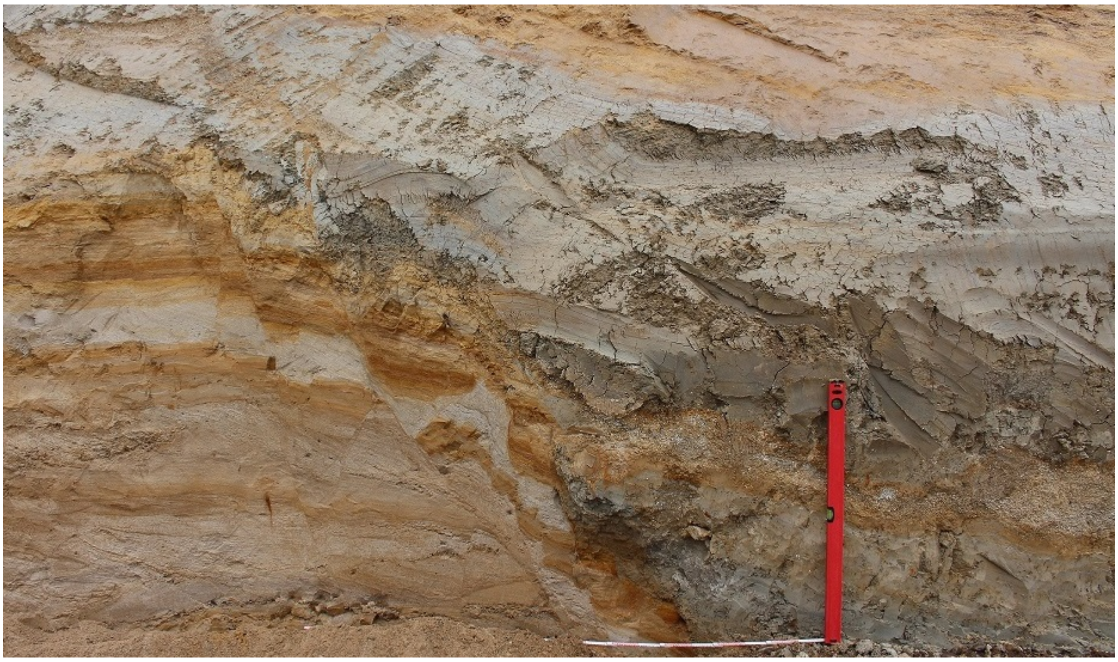

Figure 3.41.: S part of fault zone at W wall of building pit, spirit level for scale is 1 m.

Several smaller-scale dislocations (sometimes conjugated) with single offsets of a few cm to 30 cm accompany the fault zone on both sides. The sketch in figure 3.34 depicts the western wall plus OSL locations (also of bordering sidewalls south and north).

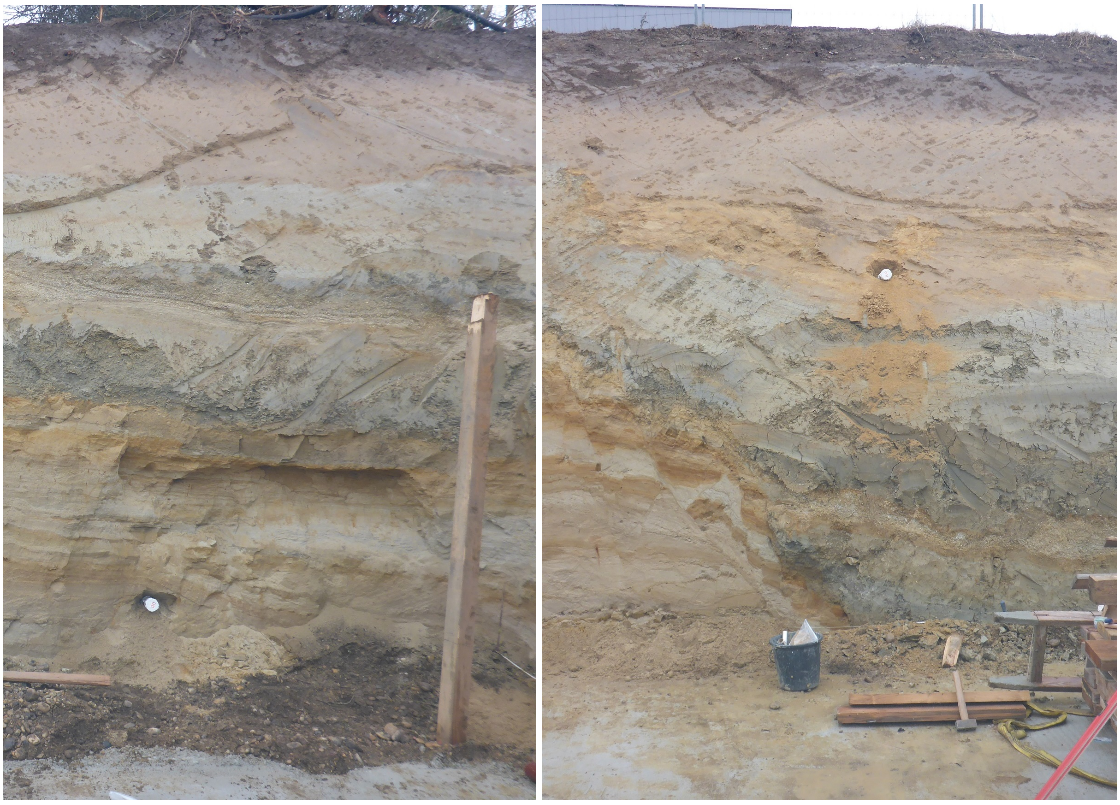

(a) OSL sample 8, southern wall

(b) OSL sample 9, western wall

Figure 3.42.: OSL sample locations at the construction pit: a) at SW corner, 40 cm above concrete level, direction of view is S; b) 2.6 m above concrete level.

Though OSL dating for the building pit described above is not completed yet, Auer (in prep.) found similar strata at the **construction site of a previous annexe south** of the Loisium winery in 2018 and carried out OSL dating (figure 3.43). Normal faults in the southern construction pit (figure 3.44) strike approximately perpendicular to the ones of the northern pit, but similar ages of the sediments in both pits can be assumed. The oldest sands in the south show a deposition age of 157.0 ± 21.7 ka, the youngest displaced layers date at 50 ka maximum.
Therefore the offset of 2.1 m, as described for the northern excavation, in presumably 150 ka gives an average vertical sliprate of 0.014 mm/a.

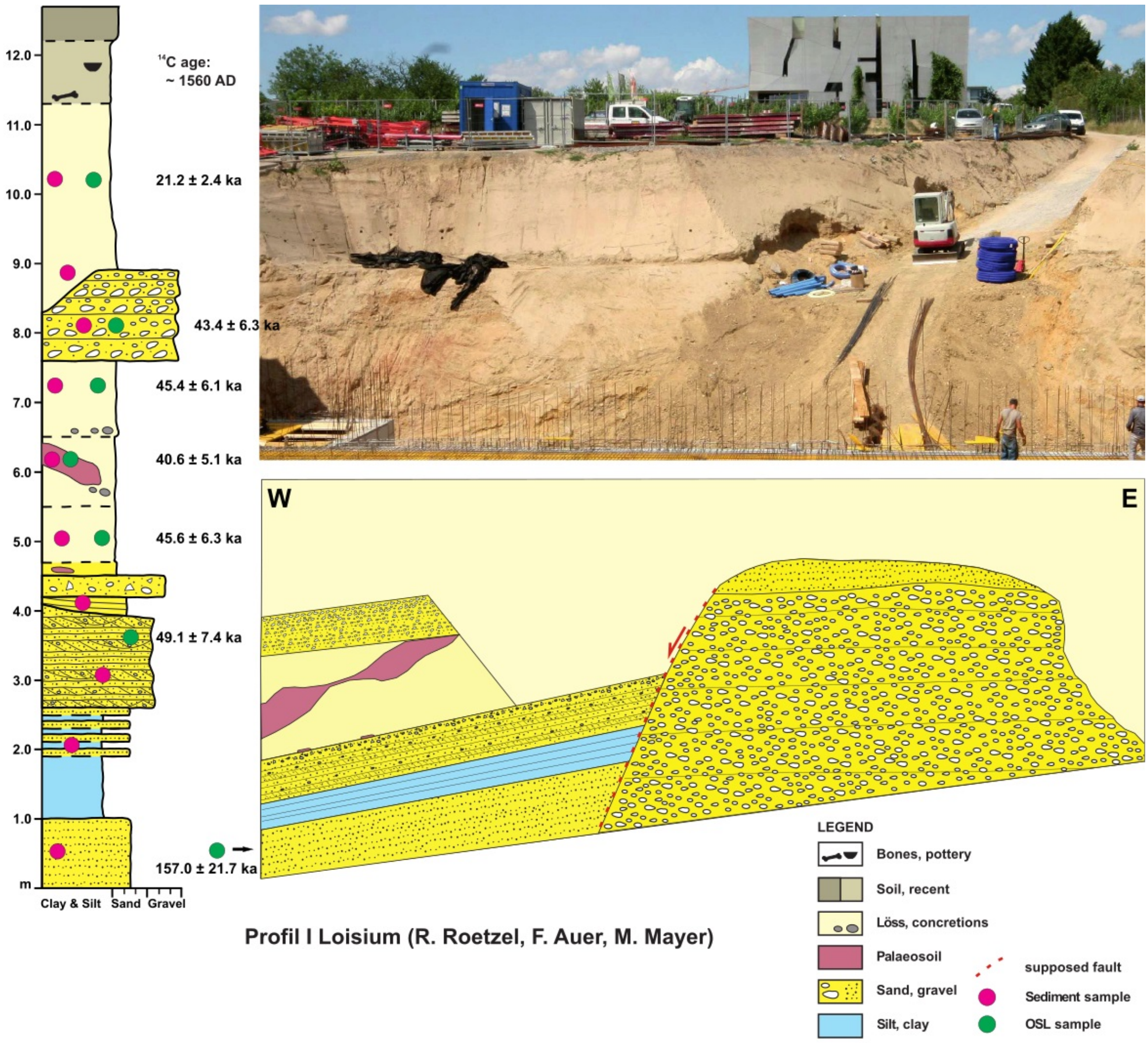

Figure 3.43.: Photograph of earlier construction pit at Loisium (south) and sedimentological profile with OSL ages by Auer (in prep.)

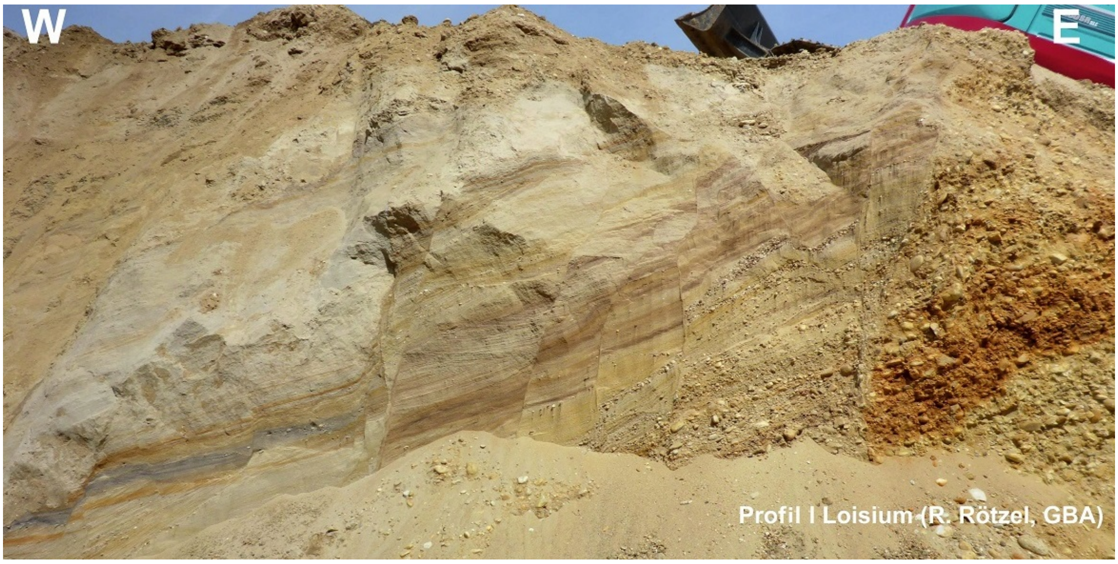

Figure 3.44.: Normal faults in earlier building pit at Loisium (S), dated by Auer (in prep.)

3.2.6. Langenlois Geißberg

The Geißberg, separating Langenlois from Straß im Straßertal in the northeast, consists of Moldanubian crystalline rocks (Nehyba et al. 2012). Its northeastern margin follows the strike of the Falkenberg Fault (FF), which forms the southeastern border of the Zöbing half-graben. Remnants of the Permo-Carboniferous sediment fill (Zöbing Fm., Vasicek 1991a) can be found next to the FF and Neogene or Quaternary deposits (loess) elsewise. Vinyard terraces cutting the Geißberg area make good outcrops giving insights on the tectonic activity. The Permo-Carboniferous sandstones and shales of the Zöbing Fm. appear intensively faulted and fractured.

Figure 3.45 shows photograph and sketch of an outcrop one terrace higher and further to the east as the other one (figure 3.46). The sketches depict the contact of Permian sandstone to loess – an E-W striking fault manifests in both outcrops. The lower terrace outcrop shows arcose sandstone of the Zöbing Fm. adjacent to scarp-related colluvial deposits and Pleistocene loess. The colluvium of diamict composition contains fine-grained (clayey) material as well as fault breccia with component size up to 10 cm. The top layer was identified as anthropogenic, because of roots of grape vine, a planting hole and a piece of pottery. The upper (and smaller) outcrop does not expose consolidated rock at all. The mix of fine-grained material, disintegrated arcosic sandstone and adjacent loess can be related to faulting. Luminescence dating of the yellow in-situ loess (sample G1) of the lower outcrop gives a result of 35.6 ± 4 ka, which can be regarded as the minimum age of tectonic activity. OSL ages of the other sediments and those of the upper outcrop could not be obtained, because of sediment redeposition (multiple bleaching events or incomplete bleaching of some grains). Anyway, vinyard terraces are anthropogenic formations, which is to be kept in mind for interpretation.

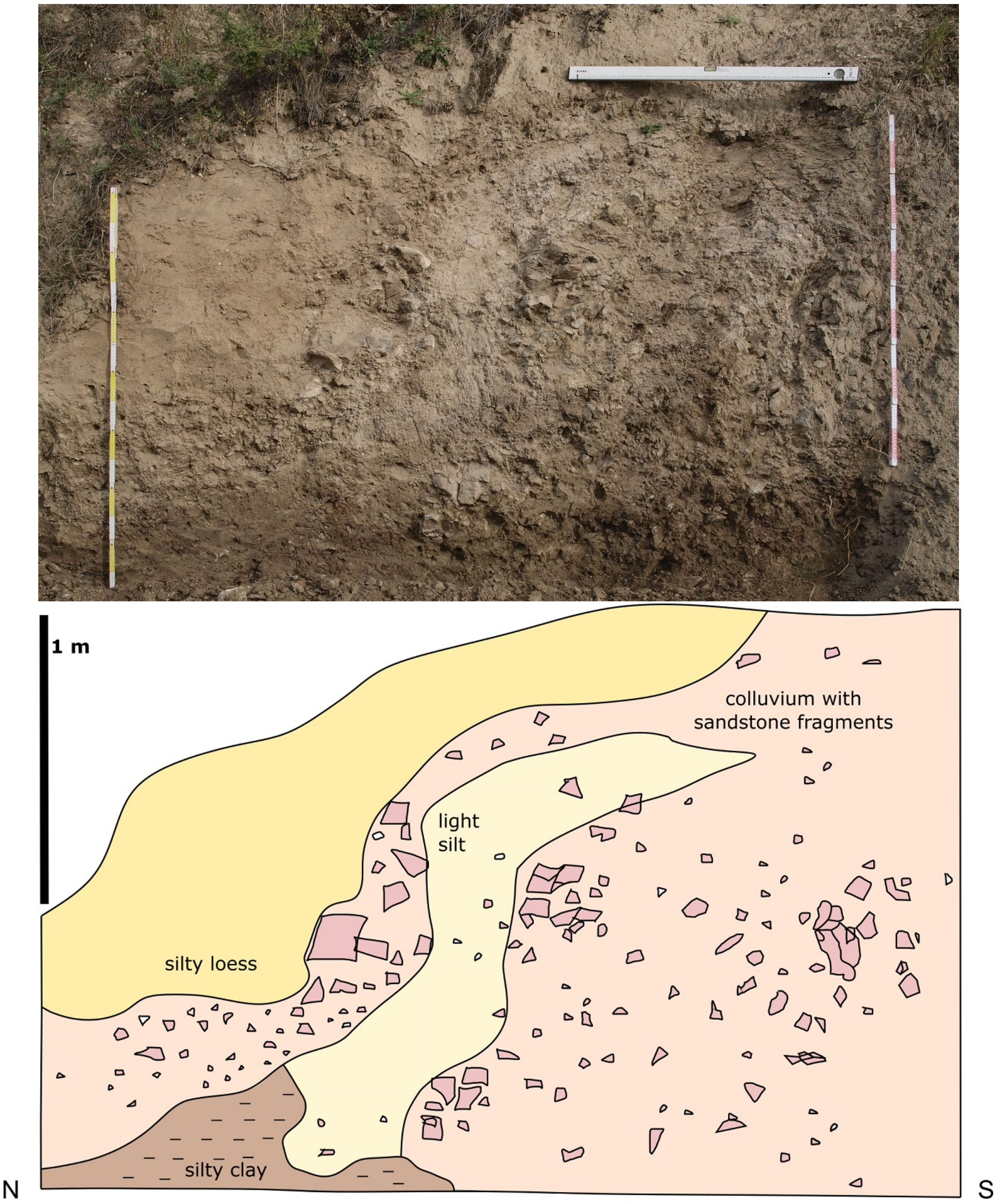

Figure 3.45.: Photograph and sketch of upper vinyard terrace outcrop at X -45389.0, Y 371550.4 (Geißberg); direction of view is east. Water spirit level is 1 m.

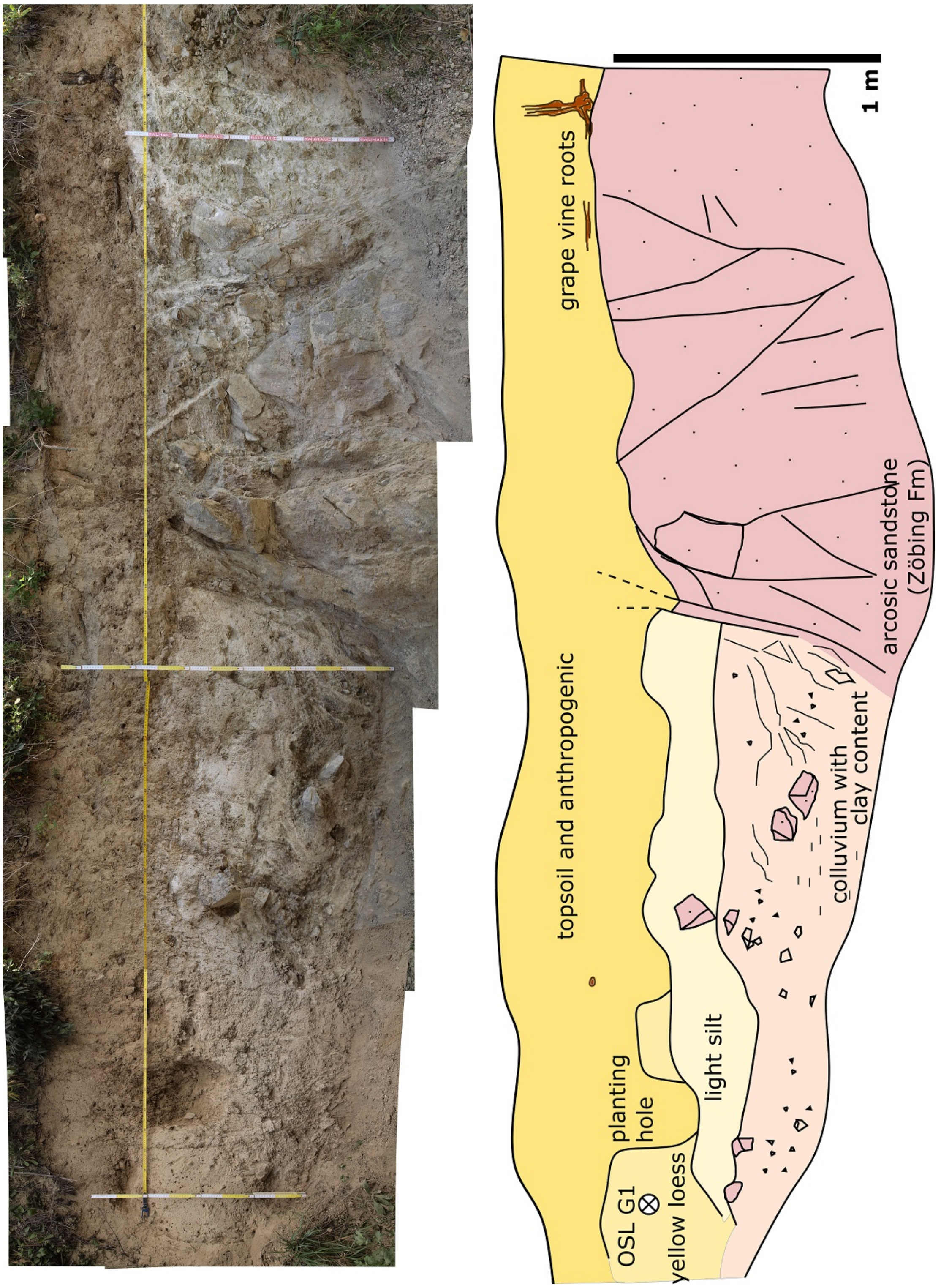

Figure 3.46.: Stitched photograph and sketch of lower vinyard terrace outcrop at the Geißberg (X -45413.6, Y 371550.6); direction of view is east. Folding rule right hand side in photograph is 1 m.

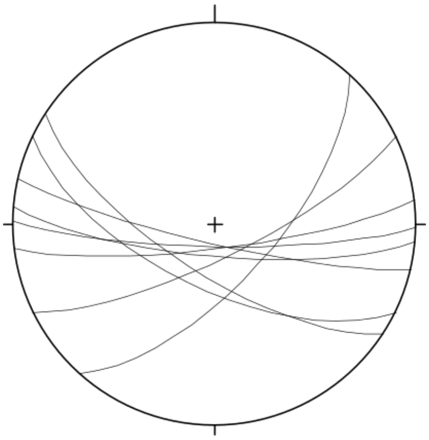

Figure 3.47.: Schmidt's net of fault planes and fractures of the lower vinyard terrace outcrop.

Two directions of faulting could be discriminated at the Geißberg: A flat-angle lineation on the NW-SE striking surfaces (Schmidt's plot figure 3.47) identified a strike-slip motion, whereas close to the Perm-loess contact a steep striation, most likely from normal faulting, was found.

4. Derivation of Geological Profiles

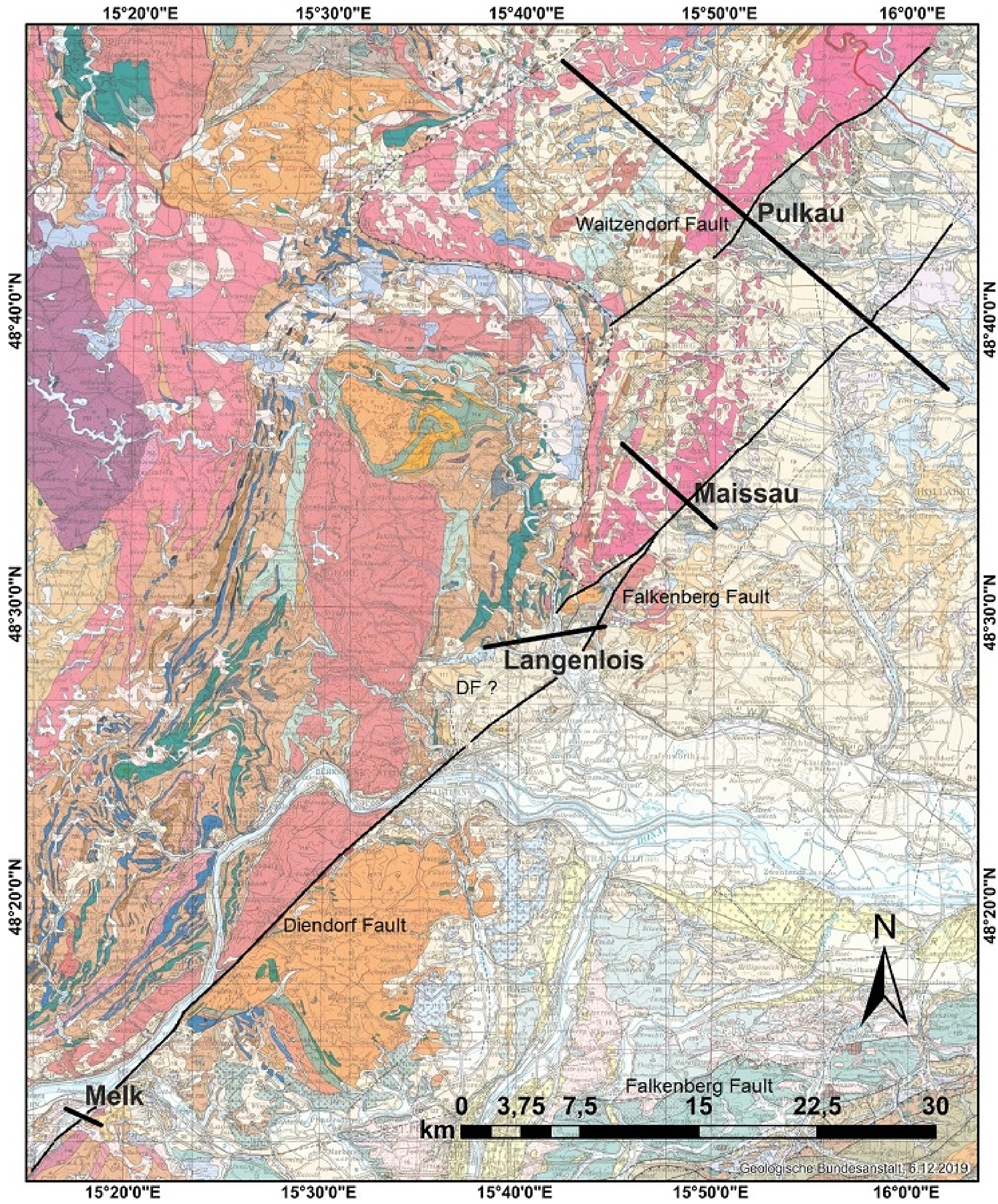

Figure 4.1.: Overview of profile locations in the geological map of Lower Austria 1:200.000 (Schnabel 2002) and supposed strike of DF, WF, FF.

Including available information on faulting and Tertiary and Quaternary sediment thickness (in addition to the geological surface information) from geophysical surveys and boreholes three geological cross sections at different fault segments have been interpreted. The fourth and northeasternmost profile crossing the Waitzendorf Segment (WF and DF) was compiled by Hintersberger and Decker 2018. Figure 4.1 gives an overview of all cross sections in the geological map of Lower Austria in the scale of 1:200.000 (Schnabel 2002).

4.1. Zelking Segment (Melk)

For the geological profile close to Melk (figure 4.3, location in figure 4.2), we could integrate sedimentary thicknesses derived from trenching and a shallow borehole nearby, plus ERT imaging data right on site, ending just several metres from the borehole (ERT GEP1, see chapter 3.2.1).
Small rectangles of alluvium in figure 4.3 depict coarse-grained sediments in the trench and the borehole, and limited lateral resolution of these data (legend for profiles Melk, Langenlois and Pulkau in figure 4.4). The well reaches the sands of the Melk Formation underlying fluvial deposits at 7.1 m beneath ground level. That seems to correlate with

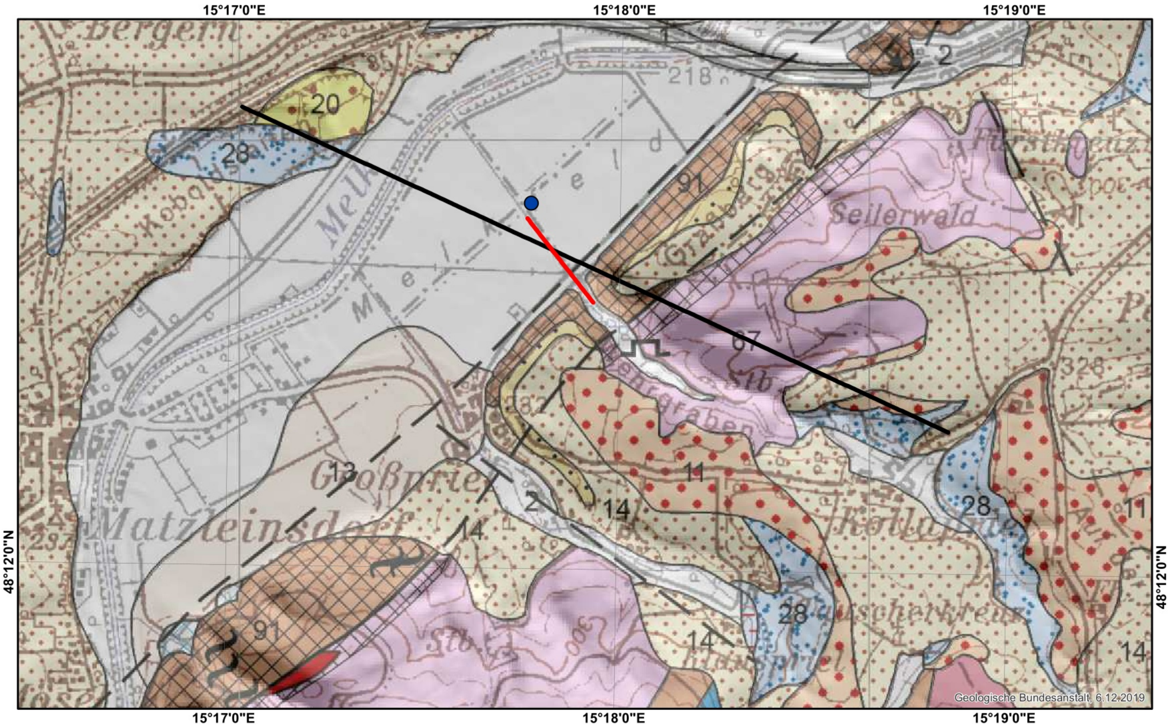

Figure 4.2.: Location of geological profile across the DF at Großpriel, plus approximate ERT profile line with 5 m spacing at trench site (red) and borehole location (blue) on the geological map of Melk (Kreuss and Linner 2018).

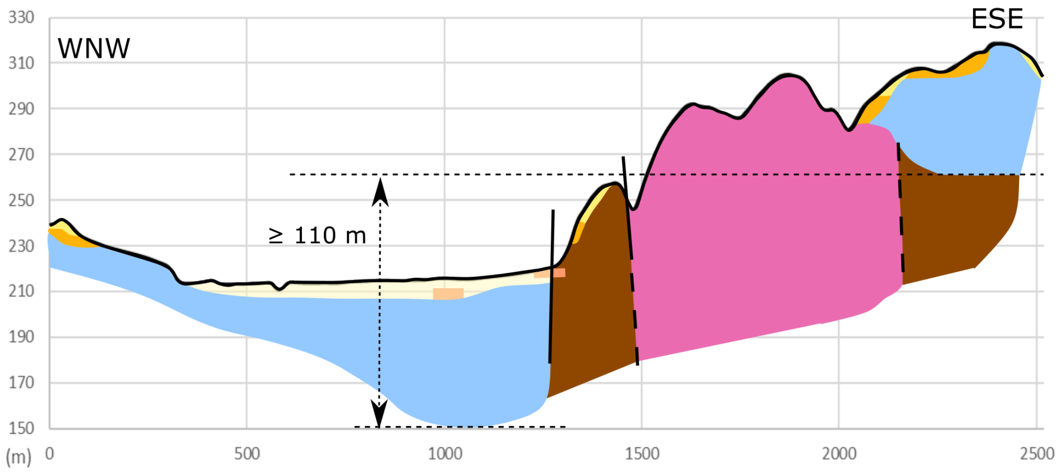

Figure 4.3.: Geological profile across the DF and comparison of elevations of the base of Oligocene sediments.

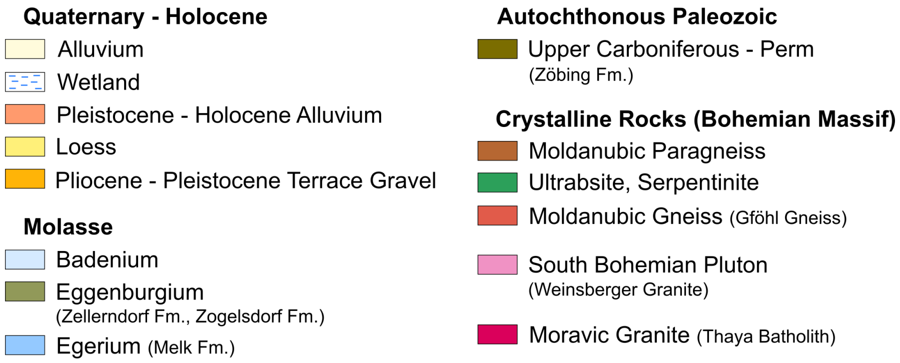

Figure 4.4.: Legend for geological profiles (figures 4.3, 4.6, 4.8), cf. Schnabel 2002.

the subsurface information at the end of the 5 m ERT profile, which does not indicate notable lithological change to a depth of 60 m (maximum inversion depth) – interpreted as Oligocene to Miocene sand (Melk Fm.) by Hintersberger and Decker 2018. On the geological map in the scale of 1:50.000 (Kreuss and Linner 2018), the base of Melk sands overlying crystalline rocks in the eastsoutheastern profile area lies around 260 m in altitude, resulting in an offset of these sediments of at least 110 m across the fault scarp of the DF.
This reflects post-depositional (especially Miocene) faulting activity. Assuming continuing vertical displacement until recent times, an offset of 110 m in ca. 20 Ma would give an average vertical sliprate of about 0.006 mm/a. Despite the clearly linear topography of the supposed fault scarp, we cannot proof more recent faulting activity, though.

4.2. Langenlois Segment

Due to the formation of the Zöbing pull-apart basin and the Pleistocene loess cover around Langenlois it is difficult to follow the strike of the DF or FF nowadays. Young or recent strike-slip activity could lead to subsidence along normal faults within the basin or at its margins. The area is shown in the map with the possible major fault lines indicated (figure 4.5, geological map of Krems 1:50.0000 W. Fuchs et al. 1984).

Two 60 m deep wells close to the Kamp river do not reach the base of Badenian sediments, which crop out at higher altitude to the west and overlie Permian rocks to the east at even higher elevation (see map overview and also figure 4.6). We do not know, how much

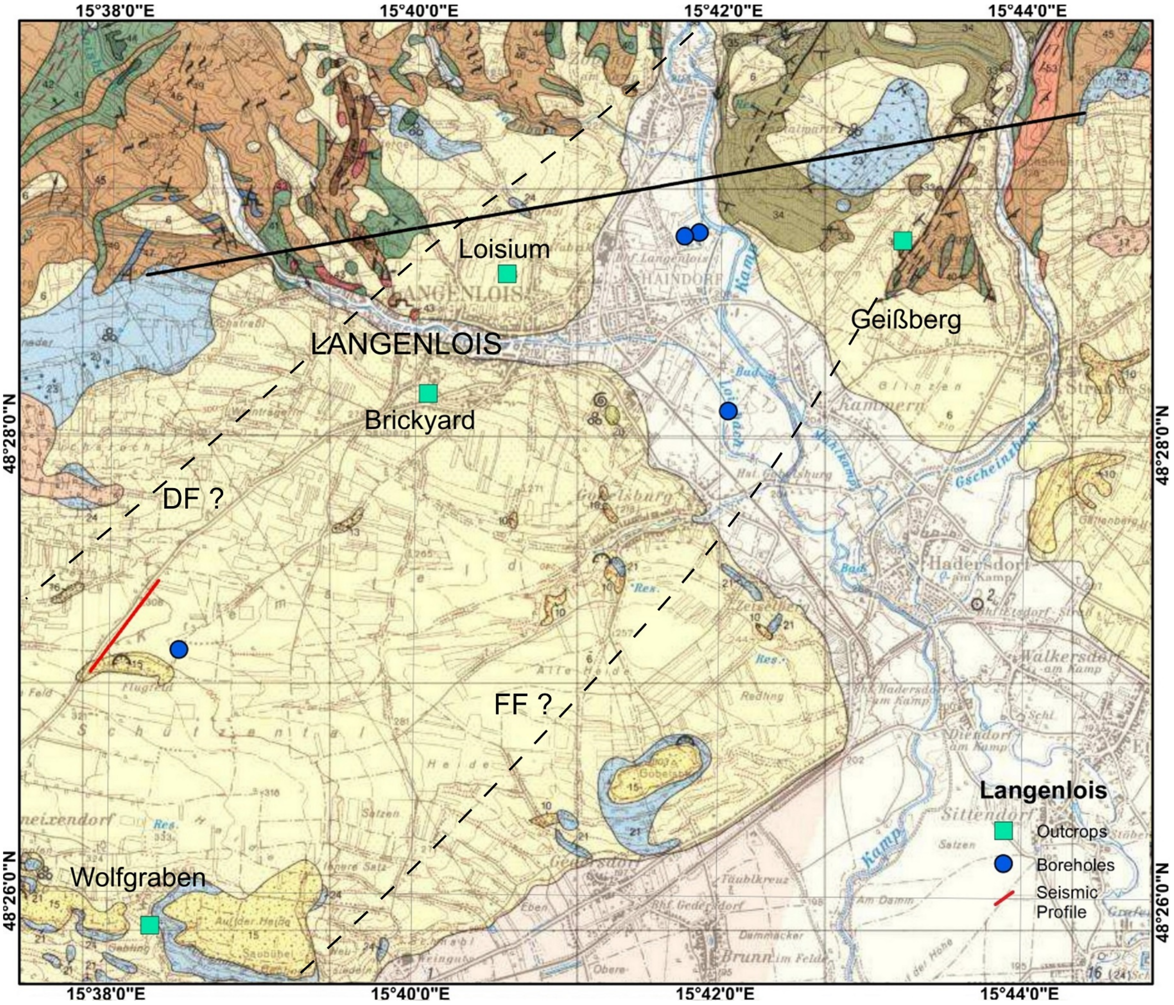

Figure 4.5.: Location of geological profile across the Kamp valley, with boreholes and outcrops around Langenlois, plus seismic profile (Meurers et al. 1993).

of these deposits had already been eroded at Kamp level (or higher altitudes), but the offset of the top of the proximal western outcrop to the top of the Badenian sediments in the boreholes is about 55 m. The offset from the borehole bottom to the base of the easternmost outcrop is about 200 m. A smaller normal displacement in between the boreholes (they are 100 m apart) is also likely, since a change from clayey silt to alternating sand and silt can be located with an offset of about 11 m from one borehole to the other. A N-S striking possible fault in the Kamp valley is delineated in the geological map of Lower Austria in the scale of 1:200.000 (Schnabel 2002). An offset of 200 m of the Badenian sediments, created in the last 13.3 Ma would lead to a average vertical slip rate of about 0.015 mm/a.

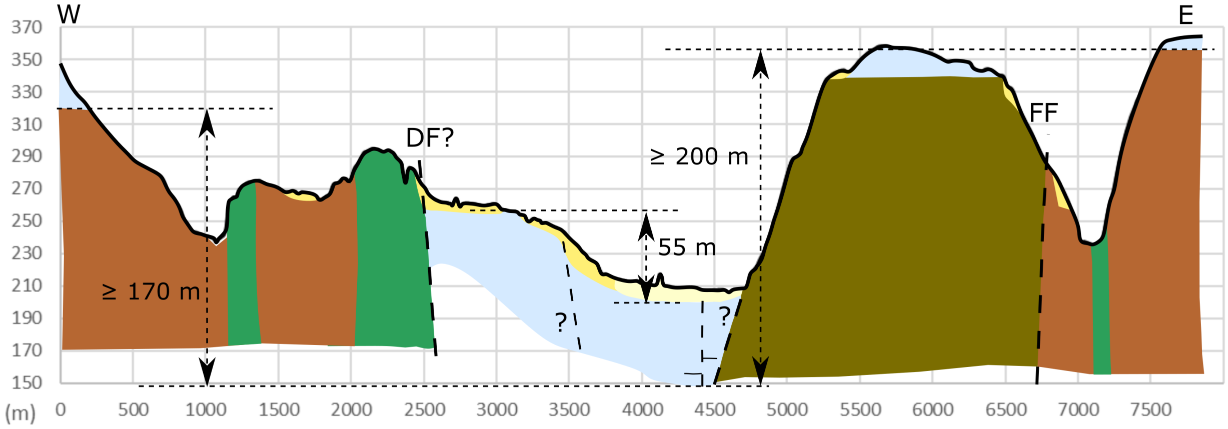

Figure 4.6.: Geological profile across the Kamp valley, strike of the FF and assumed strike of DF plus smaller normal faults.

A 2D seimsic survey by Meurers et al. 1993 with a 920 m long profile line within 4 km south of the western end of the geological profile close to Gneixendorf and a borehole nearby show the crystalline rocks at a depth of 100 to 130 m. In the northeastern quarter of the profile another short (≈ 170 m long) reflector at about 60 m below ground level had been detected, but not been discussed in detail. The seismic line probably lies within the pull-apart basin between DF and FF.

4.3. Maissau Segment

Tertiary and Quaternary sediment thickness of about 50 m next to the DF had been obtained from a seismic profile by Meurers et al. 1993. The seismic data also show minor change in rock properties at smaller depth, which is interpreted as the top of Eggenburgian[1] deposits under the Pleistocene loess cover. Sediments of the Eggenburg Group (cf. Steininger and Seneš 1971) are discriminated in the geological map (figure 4.7, greenish colours), but not in the profile (figure 4.8). And again, we do not know the exact thickness of these sediments overlying the granite on the ridge across the DF, though an offset seems likely, since the Zellerndorf Fm. of the Eggenburg Gr. reaches an elevation of 445 m in the geological map (Schnabel 2002) about 650 m from the profile line in the northwest (Sachsendorf). Comparing these topographic heights of Eggenburgian sediments in the surroundings of the profile line to interpretations of seismic data, the vertical offset of Eggenburgian sediments generated in the last 18.3 Ma, can be estimated at 80 to 90 m at the DF at Maissau. The resulting average vertical sliprate would be 0.004 to 0.005 mm/a (assuming constant deformation since sediment deposition).

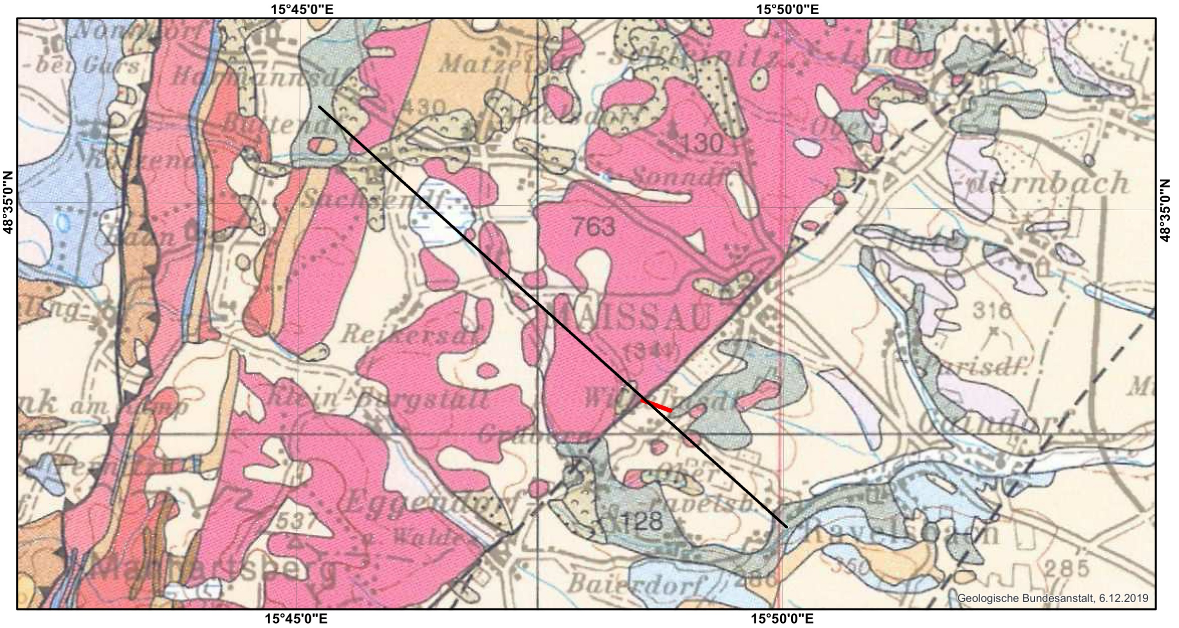

Geologische Bundesanstalt, 6.12.2019

Figure 4.7.: Location of geological profile across DF at Maissau and of seismic profile (Meurers et al. 1993, red).

---

[1] Regional chronostratigraphic Miocene stage of the central Paratethys area, 20.8 to 18,3 Ma

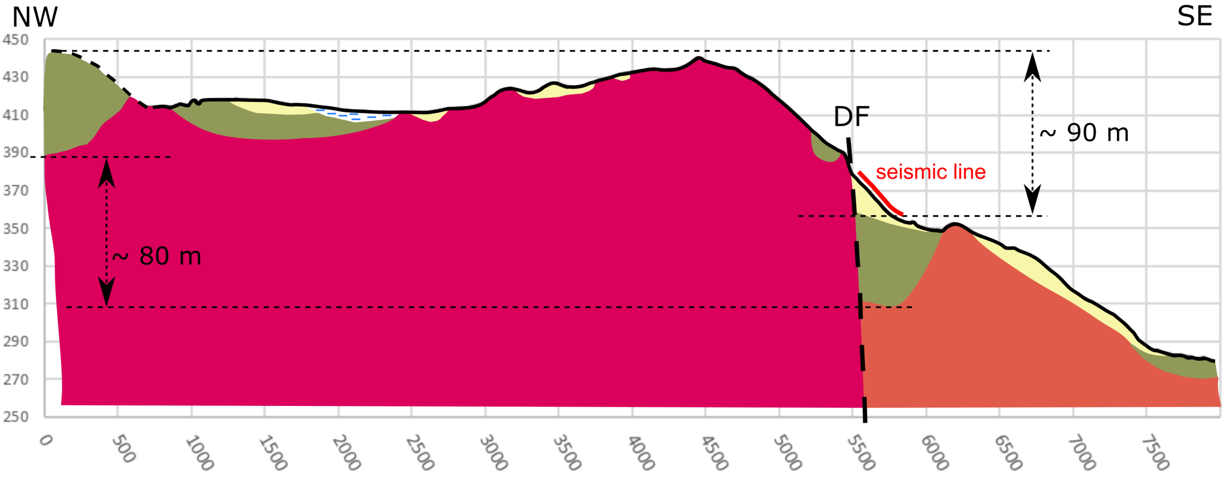

Figure 4.8.: Profile across the DF and comparison of elevations of top and bottom of Eggenburgian sediments.

4.4. Waitzendorf Segment (Pulkau)

The longest and northeasternmost profile from Hintersberger and Decker 2018 is based on the comparison of depth and thickness of Ottnangian[2] marine sediments from borehole data. The different elevations of these shallow marine sediments along the profile across the WF and DF are depicted in figure 4.10. The vertical offsets generated in the last 17 Ma, are 170 m at the WF and 30 m at the DF, resulting in average vertical sliprates of about 0.01 mm/a and 0.002 mm/a (assuming constant deformation since sediment deposition).

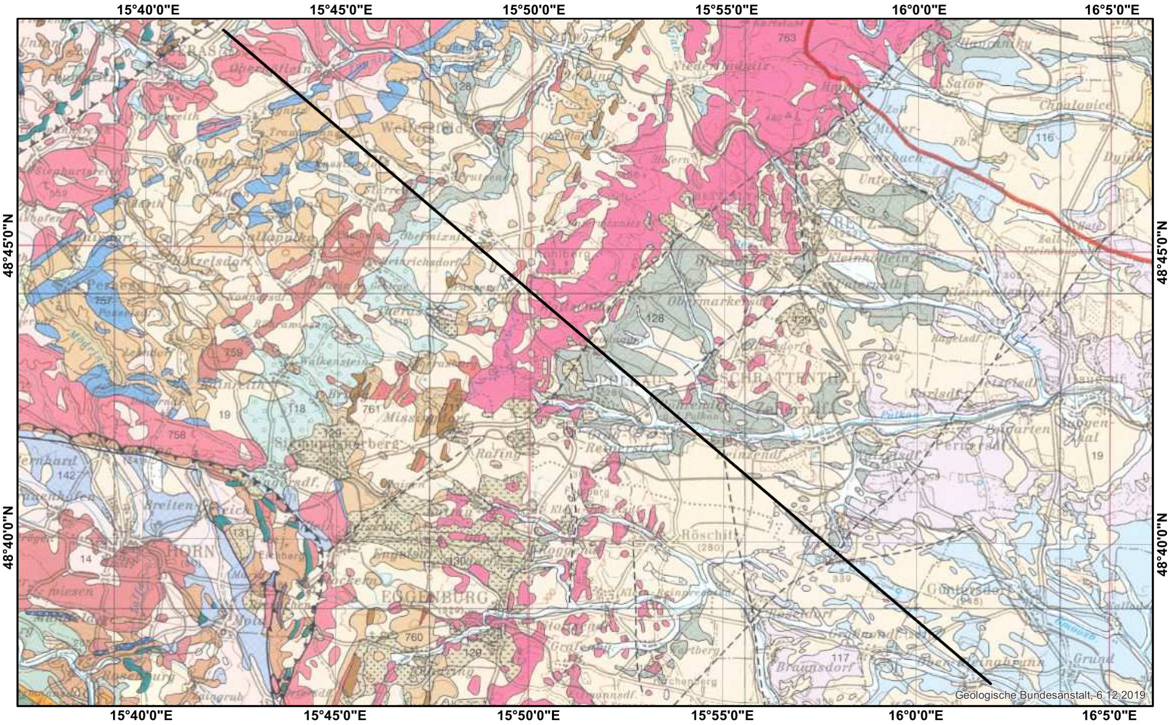

Figure 4.9.: Location of geological profile across WF and DF at Pulkau (Hintersberger and Decker 2018).

---

[2] Regional chronostratigraphic Miocene stage of the central Paratethys area, 18.3 to 17 Ma

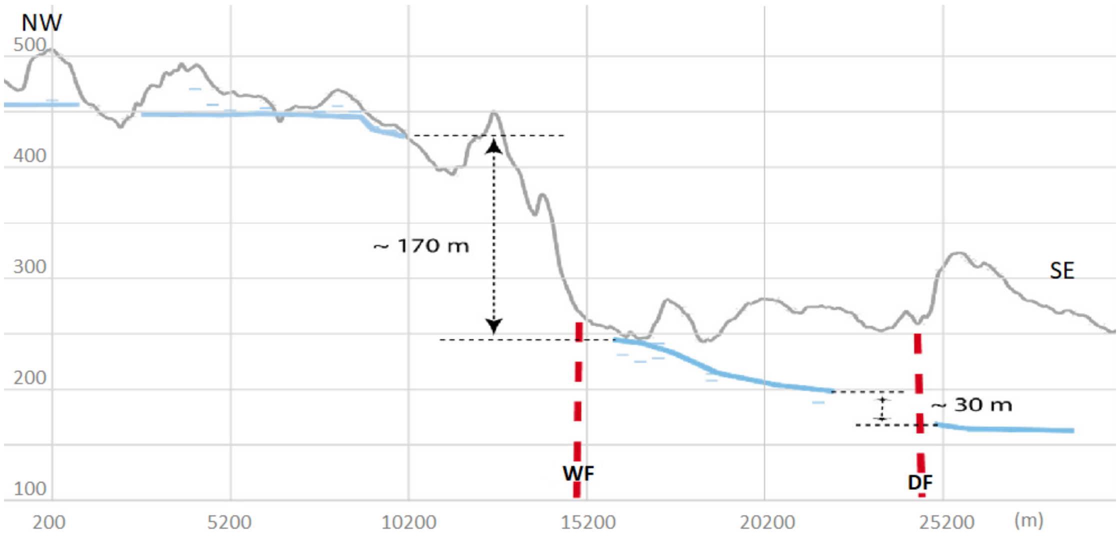

Figure 4.10.: Profile across the WF and DF and elevations of Ottnangian sediments, modified from Hintersberger and Decker 2018.

5. Discussion

Analysing tectonic geomorphology data and Quaternary deformation data along 80 km of the Diendorf Fault System in Lower Austria shows varying results on tectonic activity. The conclusions of the different methods are outlined and discussed in this chapter to gain a general view of the faulting activity along DF, FF and WF.

5.1. Geological Profiles

Four transects crossing the DF and WF at the towns of Melk, Maissau and Pulkau (Platt, respectively) and the pull-apart basin at Langenlois have been derived in chapter 4. They do not only show vertical bedrock offsets, they especially underline Miocene faulting activity. Comparing topographic heights of top or base of sedimentary units along these profile lines at opposite fault blocks suggests around 100 m to 200 m of vertical displacement since Miocene times. This would lead to average vertical slip rates of about

- 0.005 mm/a at Melk
- 0.01 mm/a at Langenlois
- 0.004-0.005 mm/a at Maissau
- 0.01 mm/a at the WF at Pulkau and 0.002 mm/a at the DF at Platt (continuation of the DF, parallel to the WF at Pulkau).

These values are only rough estimations of Miocene deformation rates, but they reveal two times higher vertical slip rates at Langenlois and Pulkau compared to Melk and Maissau. As Peresson and Decker 1997 showed, Late Miocene E-W compression inverted Middle Miocene lateral extrusion of the Eastern Alps (Ratschbacher et al. 1991) from 9 to 5.3 Ma and caused considerable uplift of the Bohemian Massif. According to Roštínský and Roetzel 2005, the northwestern block of the DF was lifted up 200 m higher than the southeastern block, resulting in the formation of the morphological features known today. Assuming, that the Late Miocene uplift along the DF's fault scarp was about the same for all cross section locations, the differences in the average vertical slip rates established after 5.3 Ma. At Langenlois, the Quaternary vertical displacement rate at the Loisium construction pit matches the Miocene vertical slip rate derived from Badenian sediment heights. There, both rates reflect subsidence within a pull-apart basin, not at a distinct fault scarp (as for instance at Maissau and Pulkau). At Melk the vertical slip rate was calculated from sediment offsets with higher elevations in the *southeast*. So this southernmost part of the southeastern fault block was probably decoupled from the relative subsidence compared to the northeastern block and the uplift here was larger, because Egerian sediments can be found in similar elevations on both fault blocks of the DF, or even about 30 m higher in the southeast – not along the cross section, but within a radius of 5 km. A hypothetical inverted vertical motion in the last 5.3 Ma compensating a vertical offset of about 200 m, and producing up to 30 m additional displacement in the southeast would give an average slip rate of 0.04 mm/a for Melk. A 4 times higher average vertical slip rate than at Langenlois and Pulkau does seem unlikely, whereas the latter had been calculated for earlier onsets of deformation (with minimum ages of the displaced sediments). Recalculation, assuming an onset of deformation at 9 Ma for all locations, gives average displacement rates of about 0.01 mm/a at Melk and Maissau, 0.02 mm/a at Langenlois and Pulkau (WF) and 0.003 mm/a at Platt. However, at Langenlois Badenian sediments are subsided within a transtensional basin, which appears to be similar at Melk for Egerian sediments. There, Egerian sediments seem to be subsided between two major faults, since they occur at similar elevations on both fault blocks, and are interpreted to lie much deeper in the valley based on ERT imaging results. The subsidence at both, Melk and Langenlois, is therefore presumed to have started earlier than 9 Ma, and the average vertical slip rates listed above seem more appropriate. Again, they are only best estimates, which should give a first valuation of deformation rates.

5.2. Electrical Resistivity Tomography (ERT)

The ERT profiles at the **Zelking segment (area of Melk)** especially mark offsets of crystalline rock blocks or show the thickness of sediment layers over hard rock (chapter 3.12). Finding faults or fault branches in sediments in ERT images requires experience in interpreting geophysical data and, sometimes, some imagination. The detailed GEP2 image, though, seems to actually display displacement of two to three different sediment layers (chapter 3.2.1, figure 3.12). That these structures could have been formed by fluvial channels was considered, since faint traces of former meanders can be seen in satellite images of the floodplains fields and meadows. This seems unlikely though, because the sharp offset at about 50 m profile length (detailed GEP2) manifests over 20 m vertically, which would be an abnormally big erosive channel. Therefore, the offset of the detailed GEP2 image is considered as a fault.

5.3. Trenching

At the **Zelking segment** of the DF, where recent tectonic activity had been expected due to a distinctly linear mountain front with triangular facettes and interpretation of geophysical data (GEP 2, as discussed above), no clear evidence of faulting could be found in the trench at **Großpriel** (chapter 3.2.2). Reconsidering our trench location, the site with a larger drainage basin compared to the surrounding watersheds and with a visible alluvial fan might not have been the best choice, because higher sedimentation (and erosion) rates are likely to interfere with the formation of seismogenic structures. As described in chapter 2.4, trenching might not be able to capture all recent surface faulting events, for instance, an earthquake rupture may not occupy exactly the same trace every time (Michetti, Audemard M., et al. 2005). Since the DF could be seen as a fault zone localising at more than one fault branches, a minor branch could as well lie some metres further to the southeast of the mapped trench, where the northeastern wall collapsed due to slippage on wet clay or further northwest across the street, as inferred by Piana Agostinetti et al. (in preparation).

5.4. Quaternary and Miocene Sediment Thickness from Shallow Boreholes

Shallow boreholes southwest of **Melk** give insights on sediment heights close to the trench site at **Großpriel** at the **Zelking segment** (chapter 3.2.1). Surprisingly, Quaternary thickness close to the end of the GEP1 ERT profile is low, despite a supposed alluvial fan being deposited at the valley mouth. Anthropogenic influence by agriculture and straightening of the river Melk and the tributary at site is considered as an explanation for that. Also, the well near the ERT profile samples a very distal part of the tributary's alluvial debris or might lie beyond the clearly influenced area. In any case, borehole data around Melk could not reflect recent faulting activity. First, the drillings may be distributed too sparsely close to the DF, and second, they do not cross the fault scarp, so that sediment heights on both fault blocks could be compared.

Data from deeper boreholes at **Langenlois** (Kamp valley floor level), however, had been useful for estimating (post) Miocene vertical displacement. The resulting average vertical sliprate correlates with the one derived from Quaternary sediments at the Loisium slope.

5.5. Tectonic Geomorphology

The morphotectonic indices calculated in chapter 3.1.1 to identify faulting related subsidence or uplift rather indicate uplift of the whole area around **Zelking** (south of **Melk**) than of one fault block relative to the other. Stream profiles appear clearly anomalous for the bigger part, so some kind of relative movement was assumed. Longitudinal profiles of the rivers Melk and Mank supported the idea of local uplift at both sides of the Diendorf fault, as inferred in chapter 3.1.1.

Around the **Zöbing pull-apart basin** (**Langenlois**) and **Maissau**, especially the Vf values point out the disequilibrium of most of the creeks. A detailed Vf survey crossing the half-graben of Zöbing apparently marks the location of WF and FF. Northeast of Maissau, the supposed N-S-striking linking fault of DF and WF seems equilibrated in the south (around Etzmannsdorf, Wartberg, Stoitzendorf), whereas the northern part (area of Röschitz and Rohrendorf) shows high Vf values, suggesting active uplift. This leads to the interpretation of a minor fault parallel to the WF starting at Roggendorf and striking in northeast direction, as presumed in the geological map of Lower Austria (Schnabel 2002). A stepover from that fault to the WF could then lie to the west of the villages Röschitz and Rohrendorf, an area, not sampled by Vf measuring points. Roetzel et al.

1998 (geological map of Hollabrunn) and Roštínský and Roetzel 2005 respectively suggest an even more dissected landscape between WF and DF, since bedrock inselbergs showed fault patters of the previous kinematic situations. Further northeast, the geomorphic indices also imply tectonic influence from **Pulkau** to Retz.

5.6. Faulted Strata

Figure 5.1 summarises the compass measurements of faults and fractures at the different outcrop locations. Except for data from crystalline rocks at Melk (Perm to Miocene faulting), at least two main tectonic regimes of (post) Miocene and Quaternary faulting can be derived from sediments:

- Miocene and/or Middle Pleistocene WSW-ENE extension

- Late Pleistocene S(SW)-N(NE) extension

Non of these directly reflects N-S convergence due to northbound Alpine orogenic thrusting, which had been suggested to reactivate Quaternary left-lateral strike-slip faulting along the DF by Decker 1999. Levi et al. 2019 confirmed approximately N-S directed recent maximum horizontal stresses $S_H max$ from borehole breakouts from the frontal part of the Eastern Alps south(west) of the Bohemian Massif. Assuming that faulting was reactivated by such stresses, graben formation of the so-called Zöbing pull-apart basin at a releasing bend close to Langenlois could also be reinitiated. This would cause an extensional regime within the basin, which would perfectly explain WSW-ENE-directed extension and secondary normal faults in theory (see chapter 2.3). The NNW-SSE striking normal faults at the brickyard Langenlois, corresponding to the ones reported by Auer (in prep.) at an excavation at Langenlois Loisium, seem to fit into that idea, but the older NW-SE striking ones in Badenian conglomerates at Wolfgraben could also have been established during a similar deformational regime in Miocene, or during a Late Miocene to Pliocene stress field with vertical maximum stress axis σ_1 and NNE-trending minimum stress axis σ_3 (Decker 1999). More data would be necessary, for a clear discrimination between these earlier stress regimes, in any case, the (N)NE-trending faults at Langenlois are likely to represent two different deformational phases along the DF, one from Miocene–Pliocene times and one from Pleistocene.

The recent kinematic setting around Langenlois seems more complex again, leading to N(NE)-S(SW) extension, which would need further investigation though, but e.g. gravitational movement along bedrock slopes (locally) or a local to regional-scale rotational deformation component are first concepts, which could possibly affect secondary faulting during basin formation. A rotational component might be established by loading of the foreland by the Alpine thrust wedge, resulting in downward bending of the foreland, which could establish a deformational regime, entirely seperate from the DF, and in agreement to N-directed Alpine thrusing.

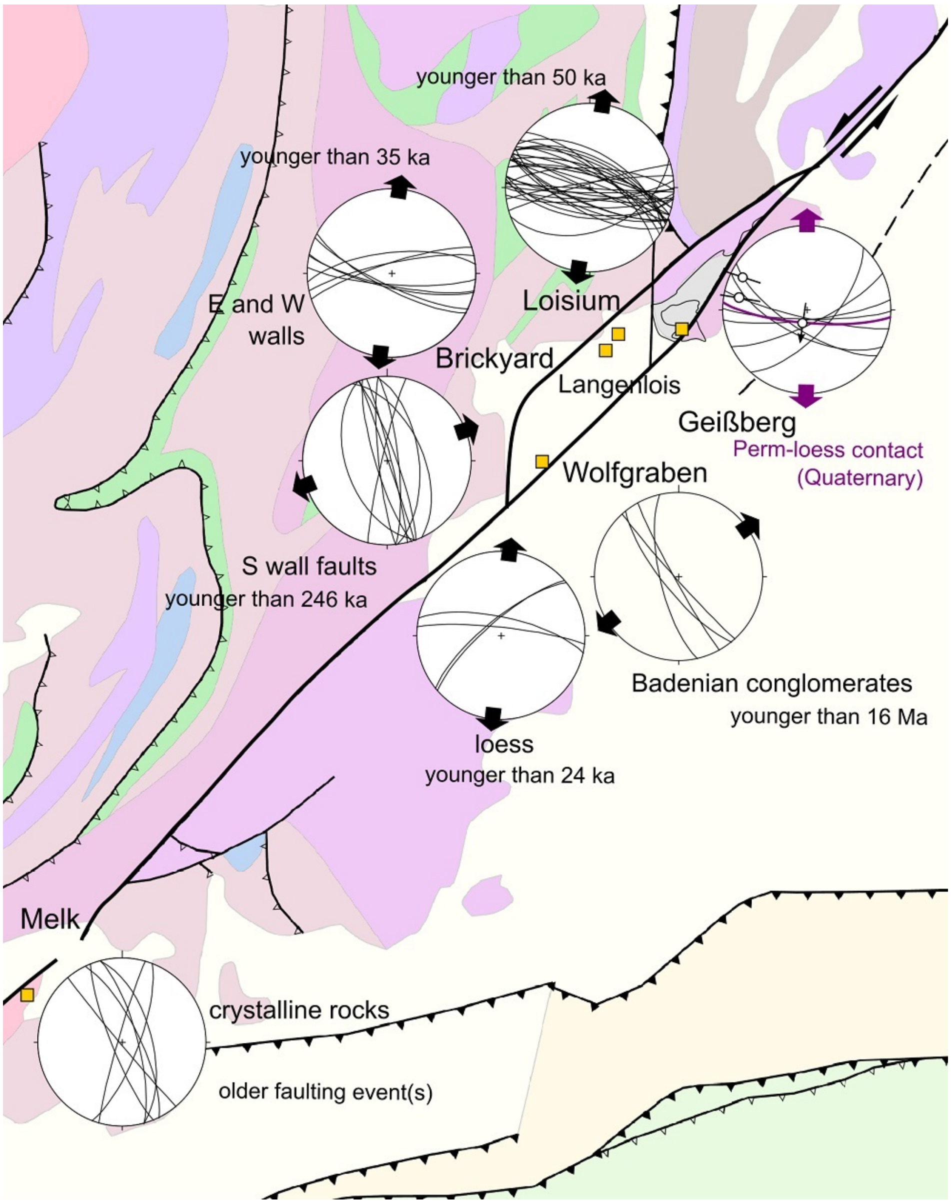

Figure 5.1.: Locations of outcrops plus stereoplots of slip data, mostly obtained from Late Pleistocene sediments, legend in appendix.

6. Conclusions

Analysing of tectonic geomorphology, geophysical subsurface investigations and shallow borehole data, as well as geological cross sections and Quaternary deformation data from outcrops, and taking previous studies into account, the Diendorf Fault System can be regarded as active.

In particular, a releasing bend and resulting pull-apart basin around Langenlois, well assessed in four outcrops, with partly considerable vertical displacement of Quaternary sediments, provides strong evidence for the DF's tectonic activity. Although, the W(NW)-E(SE)-trending normal faults at Langenlois do not represent a stress field, associated with a pull-apart basin along the DF, entirely perfectly. In any case, the NNW-SSW-trending faults at the brickyard and described by Auer (in prep.) at a construction pit at Loisium are in agreement with a possible Quaternary transtensional regime at the DF at Langenlois. The average vertical slip-rate of 0.01 mm/a from Miocene sedimentary displacement in Langenlois remains unchanged, if only Quaternary vertical displacement is considered – derived from a single outcrop though, at a second excavation pit at Loisium, where Quaternary faults even hint prehistoric coseismic deformation. The vertical displacement rate of 0.01 mm/a in Langenlois is also similar to the one at the WF at Pulkau obtained from Ottnangian sediment offsets.

The average vertical slip-rate calculations are only best estimates and we cannot provide Quaternary faulting data for Maissau and Pulkau. Yet, sinistrally deflected rivers at Maissau are a clear expression of young to ongoing strike-slip faulting, which is believed to cause vertical displacement as described above at the releasing bend at Langenlois. An explanation for missing evidence of strike-slip faulting at Pulkau could be found between WF and DF in dissecting smaller-scale parallel faults and N-S striking linking faults. Strain distribution on three or more NE-SW trending fault branches there, in contrast to only one, the DF, at Maissau, could compensate left-lateral deformation. The overall displacement along the DF is considered to be reactivated by northbound Alpine thrusting. The fault segment at Melk is possibly influenced by the Alpine thrust in a different way, maybe associated with the south Bohemian basement spur (cf. Reinecker and W. A. Lenhardt 1999). Already Late Miocene E-W compression affected that region differently than the fault scarps further north. In more recent times, especially the area around Zelking shows hints of uplift of both sides of the fault. There, the reactivation might not clearly manifest in strike-slip faulting, because of tectonic loading and rigid tilting of the southernmost tip of the Bohemian Massif.

References

Auer, Fabian ((in prep.)). *Deciphering the Quaternary sedimentary and neotectonic history of a loess-paleosol sequence from Langenlois (Lower Austria) by optically stimulated luminescence (OSL) dating.* unpublished. Innsbruck.

Basili, Roberto et al. (2013). *The European Database of Seismogenic Faults (EDSF) Compiled in the framework of the Project SHARE; The European Database of Seismogenic Faults; EDSF.*

Baumgart, Susanne (2019). *Bericht zur archäologischen Fundmeldung in Großpriel.* St. Pölten.

Bell, F.G. (2004). *Engineering Geology and Construction.* Taylor & Francis. ISBN: 9780415259392.

Blott, Simon J. and Kenneth Pye (2012). “Particle size scales and classification of sediment types based on particle size distributions: Review and recommended procedures”. In: *Sedimentology* 59.7, pp. 2071–2096. ISSN: 0037-0746.

Brandmayr, Michael et al. (1995). “Conjugate shear zones in the Southern Bohemian Massif (Austria): implications for Variscan and Alpine tectonothermal activity”. In: *Tectonophysics* 248.1, pp. 97–116. ISSN: 0040-1951.

Bull, W.B. and L.D. McFadden (1977). “Tectonic Geomorphology north and south of the Garlock Fault, California.” In: *Geomorphol. arid reg. annu. geomorphol. symp. 8. proc.; Binghampton, N.Y.; S.L.; BIBL. 1 P. 1/2; 6 ILL.* Pp. 115–138.

Burbank, Douglas W. and Robert S. Anderson (2012). *Tectonic geomorphology.* 2nd ed. Chichester [u.a.]: Wiley. ISBN: 9781444338867.

Coolen, Joris (2015). *Siedlungsgeografische Studien zum Frühneolithikum in der Umgebung von Melk, Niederösterreich.* Beiträge zur Ur- und Frühgeschichte Mitteleuropas ; 80. Langenweissbach: Beier & Beran, Archäologische Fachliteratur, p. 524. ISBN: 9783941171480.

Decker, Kurt (1999). “Tektonische Auswertung integrierter geologischer, geophysikalischer, morphologischer und strukturgeologischer Daten”. In: *Geogenes Naturraumpotential Horn-Hollabrunn etc., Projektbericht Bund-Bundesländerkooperation, Heinrich et al.* P. 250.

Everett, Mark E. (2013). *Near-Surface Applied Geophysics.* Cambridge University Press. DOI: `10.1017/CBO9781139088435`.

Feathers, James (2008). “Luminescence Dating”. In: *Encyclopedia of Archaeology.* Elsevier Inc, pp. 1590–1592. ISBN: 9780123739629.

Figdor, Harald and Adrian E. Scheidegger (1977). “Geophysikalische Untersuchungen an der Diendorfer Störung”. In: *Verh. Geol.B.-A.* Pp. 243–277.

Fink, J. et al. (1978). *Exkursion durch den österreichischen Teil des nördlichen Alpenvorlandes und den Donauraum zwischen Krems und Wiener Pforte : Erg. : Anläßlich der DEUQUA-Tagung 1978 in Österreich.* Wien: Österr. Akad. d. Wiss.

Folk, R.L. and W.C. Ward (1957). "Brazos River Bar – a study in the significance of grain size parameters". In: *Journal of Sedimentary Petrology* 48, pp. 3–26.

Friedman, Gerald M. (1962). "On Sorting, Sorting Coefficients, and the Lognormality of the Grain-Size Distribution of Sandstones". In: *The Journal of Geology* 70.6, pp. 737–753. ISSN: 00221376.

Fuchs, Gerhard and Alois Matura (1976). "Zur Geologie des Kristallins der südlichen Böhmischen Masse". In: *Jahrbuch der Geologischen Bundesanstalt* 119, pp. 1–43.

Fuchs, W. et al. (1984). *Geologische Karte der Republik Österreich 1: 50000. 38 Krems.* Geologische Bundesanstalt. Karte. Wien.

Hack, John T (1973). "Stream-profile analysis and stream-gradient index". In: *Journal of Research of the us Geological Survey* 1.4, pp. 421–429.

Hintersberger, Esther and Kurt Decker (2018). "Active Tectonics of the Diendorf-Boskovice Fault System (Lower Austria) and its Possible Impact on the Seismic Safety of the NPP Dukovany". In: p. 60.

Hintersberger, Esther, Kurt Decker, et al. (2018). "Implications from palaeoseismological investigations at the Markgrafneusiedl Fault (Vienna Basin, Austria) for seismic hazard assessment." In: 18.2, pp. 531–553. ISSN: 1561-8633.

Jaros, J. and Z. Mísař (1976). "Nomenclature of the tectonic and lithostratigraphic units in the Moravian Svratka Dome (Czechoslovakia)". In: *Věst. ÚÚG Praha* 51.2, pp. 113–122.

Karl, Raimund (1996). *Latènezeitliche Siedlungen in Niederösterreich : Untersuchungen zu Fundtypen, Keramikchronologie, Bautypen, Siedlungstypen und Besiedlungsstrukturen im latènezeitlichen Niederösterreich : 1 : Grundlagen.* Historica - Austria ; 2. Wien: Österr. Archäologie-Bund, Dachverb. Österreich. ISBN: 3901515038.

Kreuss, Otto and Manfred Linner (2018). *Geofast – Zusammenstellung ausgewählter Archivunterlagen der Geologischen Bundesanstalt 1:50.000 – 54 Melk: Stand 2018.* Geologische Bundesanstalt.

Leichmann, J. and E. Hejl (1996). "Quarternary tectonics at the eastern border of the Bohemian massif: new outcrop evidence." In: *Geological Magazine* 133. ISSN: 0016-7568.

Lenhardt, Wolfgang et al. (2007). "Seismic activity of the Alpine-Carpathian-Bohemian Massif region with regard to geological and potential field data". In: *Geologica Carpathica* 58. ISSN: 1335-0552.

Levi, N et al. (2019). "The stress field in the frontal part of the Eastern Alps (Austria) from borehole image log data". eng. In: *Tectonophysics* 769, p. 228175. ISSN: 0040-1951.

Libby, Willard F. (June 1946). "Atmospheric Helium Three and Radiocarbon from Cosmic Radiation". In: *Phys. Rev.* 69 (11-12), pp. 671–672. DOI: `10.1103/PhysRev.69.671.2`.

– (1952). *Radiocarbon dating.* Chicago, Ill.: Univ. of Chicago Press.

Matte, Philippe (1990). "Terrane boundaries in the Bohemian Massif: Result of large-scale Variscan shearing". In: *Tectonophysics* 177.1, pp. 151–170. ISSN: 0040-1951.

Matura, A. (1984). *Das Kristallin am Suedostrand der Boehmischen Masse zwischen Ybbs/Donau und St. Poelten.* Jahrbuch der Geologischen Bundesanstalt Wien. Vienna.

McCalpin, James P. (2008). *Paleoseismology.* 2nd ed. International geophysics series. Amsterdam ; Boston : Academic Press. ISBN: 1-282-28543-2.

Meurers, Bruno et al. (1993). "Seismische Untersuchung der Untergrundstruktur der Molasse am Ostrand der Böhmischen Masse". In: p. 10.

Meyer, Michael (2019). "Altersdatierung der Lössaufschlüsse Gaisberg und Wolfsgraben (Raum Langenlois, Niederösterreich) mittels Optisch Stimulierter Lumineszenz". In: p. 10.

Michetti, AM., Franck A. Audemard M., and S. Marco (2005). "Future trends in paleoseismology: Integrated study of the seismic landscape as a vital tool in seismic hazard analyses". In: *Tectonophysics* 408.1-4, pp. 3–21. ISSN: 0040-1951.

Michetti, AM., E. Esposito, et al. (2007). "Environmental seismic intensity scale-ESI 2007". In: *Memorie Descrittive della Carta Geologica d'Italia* 74, pp. 7–54.

Nasir, Asma et al. (2013). "Assessing the completeness of historical and instrumental earthquake data in Austria and the surrounding areas". In: *Austrian Journal of Earth Sciences* 106.1, pp. 90–102. ISSN: 2072-7151.

Nehyba, Slavomír, Reinhard Roetzel, and Lubomír Mastera (2012). "Provenance analysis of the Permo-Carboniferous fluvial sandstones of the southern part of the Boskovice Basin and the Zobing Area (Czech Republic, Austria): implications for paleogeographical reconstructions of the post-Variscan collapse basins". In: *Geologica Carpathica* 63.5, p. 365. ISSN: 13350552. URL: `http://search.proquest.com/docview/1322351084/`.

Novotný, Miroslav (2012). "Depth-Recursive Tomography of the Bohemian Massif at the CEL09 Transect—Part B: Interpretation". In: *Surveys in Geophysics* 33.2, pp. 243–273. ISSN: 0169-3298.

Peresson, Herwig and Kurt Decker (1997). "Far-field effects of Late Miocene subduction in the Eastern Carpathians: E-W compression and inversion of structures in the Alpine-Carpathian-Pannonian region". In: *Tectonics (Washington, D.C.)* 16.1, pp. 38–56. ISSN: 0278-7407.

Piana Agostinetti et al., Nicola ((in preparation)). "Near-surface investigation using teleseismic P-waves embedded in active seismic recordings". In: *Geophysical Prospecting.*

Popotnig, Angelika, Dana Tschegg, and Kurt Decker (2013). "Morphometric analysis of a reactivated Variscan fault in the southern Bohemian Massif (Bud/vejovice basin, Czech Republic)". In: *Geomorphology* 197, pp. 108–122. ISSN: 0169-555X.

Pospíšil, Lubomil et al. (2009). "Geodetic and geophysical analyses of the Diendorf-Čebín tectonic zone.(Report)". In: *Acta Geodynamica et Geomaterialia* 6.3, pp. 309–321.

– (2012). "Active tectonics in the eastern margin of the Bohemian Massif–based on the geophysical, geomorphological and GPS data.(Report)". In: *Acta Geodynamica et Geomaterialia* 9.3, p. 315. ISSN: 1214-9705.

Ramírez-Herrera, María Teresa (1998). "Geomorphic assessment of active tectonics in the Acambay graben, Mexican Volcanic Belt". In: *Earth Surface Processes and Landforms* 23.4, pp. 317–332. ISSN: 0197-9337.

Ranftl, Eva-Maria (2017). "Untersuchung der tektonischen Aktivität der Diendorfer Störung im Bereich Zelking-Matzleinsdorf". Bachelor Thesis. Department of Geodynamics and Sedimentology, University of Vienna, p. 38.

Ratschbacher, Lothar, Wolfgang Frisch, and Hans Gert Linzer (1991). “Lateral Extrusion in the Eastern Alps. Part 2: structural analysis”. In: *Tectonics* 10.2, pp. 257–271.

Reinecker, J. and W. A. Lenhardt (1999). “Present-day stress field and deformation in eastern Austria”. In: *International Journal of Earth Sciences* 88.3, pp. 532–550. ISSN: 1437-3254.

Roetzel, R. et al. (1998). *Geologische Karte der Republik Österreich 1: 50000. 22 Hollabrunn.* Geologische Bundesanstalt. Karte. Wien.

Roštínský, Pavel, Lubomil Pospíšil, and Otakar Svábenský (2013). “Recent geodynamic and geomorphological analyses of the Diendorf–Čebín Tectonic Zone, Czech Republic”. In: *Tectonophysics* 599, pp. 45–66. ISSN: 0040-1951.

Roštínský, Pavel, Lubomil Pospíšil, Otakar Svábenský, et al. (2020). “Risk faults in stable crust of the eastern Bohemian Massif identified by integrating GNSS, levelling, geological, geomorphological and geophysical data”. In: *Tectonophysics* 785, p. 228427. ISSN: 0040-1951.

Roštínský, Pavel and Reinhard Roetzel (Mar. 2005). “Exhumed Cenozoic landforms on the SE flank of the Bohemian Massif in the Czech Republic and Austria”. In: *Zeitschrift für Geomorphologie* 49, pp. 23–45.

Rötzel, Reinhard (1996). “Bericht 1994/1995 über geologische Aufnahmen im Tertiär und Quartär mit Bemerkungen zur Tektonik am Diendorfer Störungssystem auf Blatt 22 Hollabrunn”. In: *Jahrb. Geol.B.-A.* 139.3, pp. 286–295.

Rötzel, Reinhard, Peter Hochuli, and Friedrich Steininger (1983). “Die Faziesentwicklung des Oligozäns in der Molassezone zwischen Krems und Wieselburg (Niederösterreich)”. In: *Jahrbuch der Geologischen Bundesanstalt* 126.1, pp. 129–179.

Scheidegger, Adrian E. (1976). “Untersuchungen des Beanspruchungsplanes im Einflußgebiet der Diendorfer Störung”. In: *Jahrb. Geol.B.-A.* 119, pp. 83–95.

Schermann, Otmar (1966). “Über Horizontalseitenverschiebung am Ostrand der Böhmischen Masse”. In: *Mitteilungen d. Ges. d. Geol.- u. Bergbaustud.* 16, pp. 89–103.

Schnabel, Wolfgang (2002). *Geologische Karte von Niederösterreich 1:200.000.* Geologische Bundesanstalt. Wien.

Schumm, Stanley A. (May 1956). “Evolution of Drainage Systems and Slopes in Badlands at Perth Amboy, New Jersey”. In: *GSA Bulletin* 67.5, pp. 597–646. ISSN: 0016-7606. DOI: `10.1130/0016-7606(1956)67[597:EODSAS]2.0.CO;2`.

Serva, Leonello et al. (2016). “Earthquake Hazard and the Environmental Seismic Intensity (ESI) Scale”. In: *Pure and applied geophysics* 173.5, pp. 1479–1515. ISSN: 0033-4553.

Slánská, Jarmila (1976). “A red-bed formation in the South Bohemian Basins, Czechoslovakia”. In: *Sedimentary Geology* 15.2, pp. 135–164.

Stackebrandt, Werner and Hans-Joachim Franzke (1989). “Alpidic reactivation of the variscan consolidated lithosphere: The activity of some fracture zones in Central Europe.” In: *Z. Geol. Wiss.* 17, pp. 699–712.

Steininger, Fritz and Ján Seneš (1971). *Chronostratigraphie und Neostratotypen : Miozän der zentralen Paratethys : 2 : M [tief] 1 - Eggenburgien : die Eggenburger Schichtengruppe und ihr Stratotypus.* Bratislava: Verl. der Slowak. Akad. d. Wiss.

Štěpančíková, Petra et al. (2010). “Active tectonics research using trenching technique on the south-eastern section of the Sudetic Marginal Fault (NE Bohemian Massif, central Europe)”. In: *Tectonophysics* 485.1-4, pp. 269–282. ISSN: 0040-1951.

Talling, Peter J. et al. (1997). “Regular spacing of drainage outlets from linear fault blocks”. In: *Basin Research* 9.4, pp. 275–302. ISSN: 0950-091X.

Thiel, Christine et al. (2011). “Sedimentation and erosion processes in Middle to Late Pleistocene sequences exposed in the brickyard of Langenlois/Lower Austria”. In: *Geomorphology* 135.3, pp. 295–307. ISSN: 0169-555X.

Tollmann, Alexander (1985). *Geologie von Österreich : 2 : Außerzentralalpiner Anteil : mit 27 Tabellen.* ger. Wien: Deuticke. ISBN: 3700545231.

Vasicek, Werner (1991a). “Das Jungpaläozoikum von Zöbing”. In: *Geologie am Ostrand der Böhmischen Masse in Niederösterreich. Schwerpunkt Blatt 21 Horn. Jahrestagung d. Geol.B.-A.* 72. Ed. by Reinhard Rötzel, pp. 98–101.

Vittori, Eutizio, Stefano Sylos-Labini, and Leonello Serva (1991). “Palaeoseismology: review of the state-of-the-art”. In: *Tectonophysics* 193.1. Multidisciplinary Evaluation of Historical Earthquakes, pp. 9–32. ISSN: 0040-1951. DOI: `https://doi.org/10.1016/0040-1951(91)90185-U`.

Waldmann, Leo (1922). “Das Südende der Thayakuppel”. In: *Jahrb. Geol.B.-A.* 72, pp. 183–204.

Wells, DL and KJ Coppersmith (1994). “New empirical relationships among magnitude rupture length, rupture width, rupture area and rupture surface”. In: *Bull Seismol Soc Am* 4.84, pp. 975–1002.

A. Appendix

A.1. Additional Figures and Tables

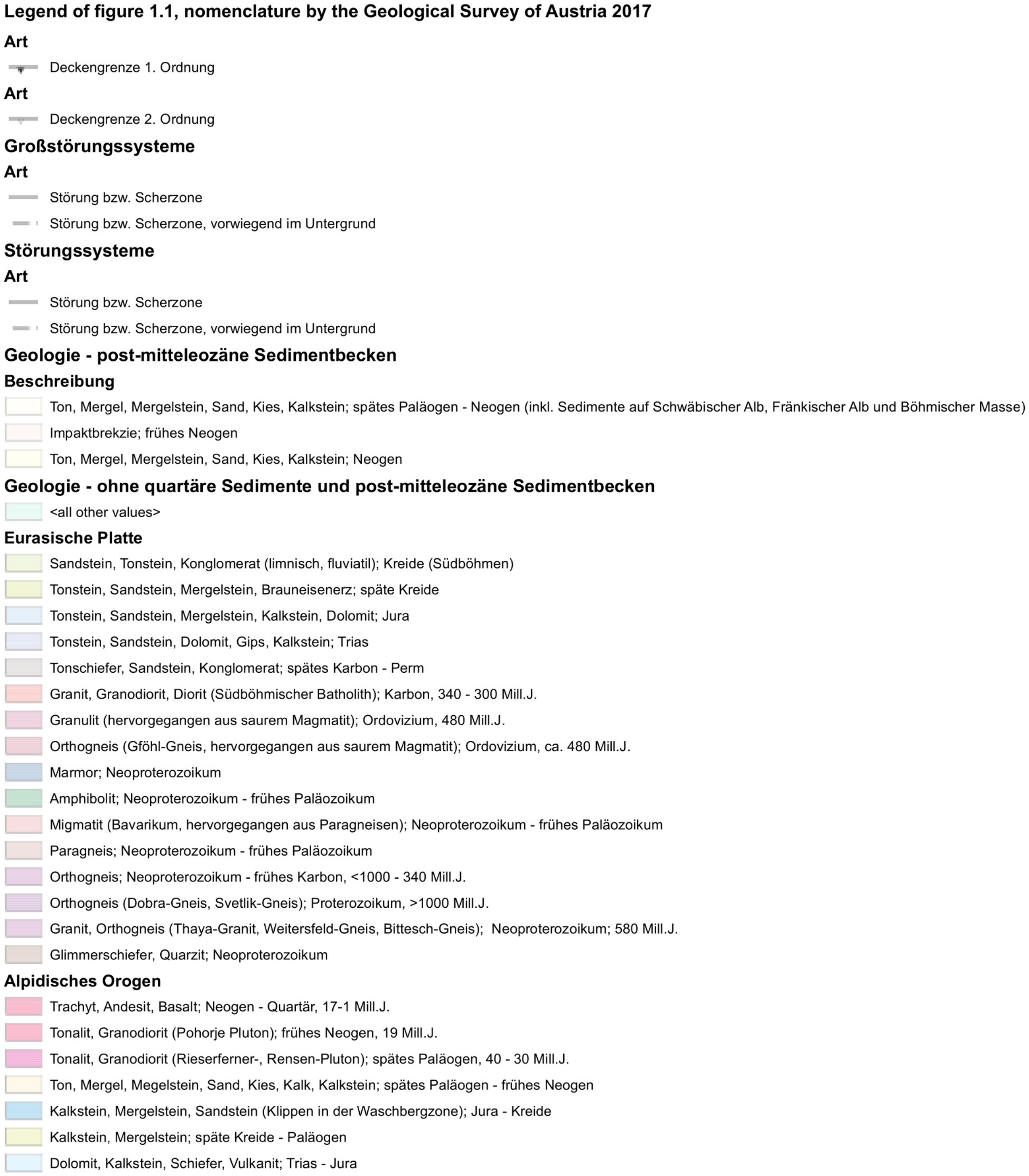

Legend of figure 1.1, nomenclature by the Geological Survey of Austria 2017

Art

— Deckengrenze 1. Ordnung

Art

— Deckengrenze 2. Ordnung

Großstörungssysteme

Art

— Störung bzw. Scherzone

- - Störung bzw. Scherzone, vorwiegend im Untergrund

Störungssysteme

Art

— Störung bzw. Scherzone

- - Störung bzw. Scherzone, vorwiegend im Untergrund

Geologie - post-mitteleozäne Sedimentbecken

Beschreibung

▢ Ton, Mergel, Mergelstein, Sand, Kies, Kalkstein; spätes Paläogen - Neogen (inkl. Sedimente auf Schwäbischer Alb, Fränkischer Alb und Böhmischer Masse)
▢ Impaktbrekzie; frühes Neogen
▢ Ton, Mergel, Mergelstein, Sand, Kies, Kalkstein; Neogen

Geologie - ohne quartäre Sedimente und post-mitteleozäne Sedimentbecken

▢ <all other values>

Eurasische Platte

▢ Sandstein, Tonstein, Konglomerat (limnisch, fluviatil); Kreide (Südböhmen)
▢ Tonstein, Sandstein, Mergelstein, Brauneisenerz; späte Kreide
▢ Tonstein, Sandstein, Mergelstein, Kalkstein, Dolomit; Jura
▢ Tonstein, Sandstein, Dolomit, Gips, Kalkstein; Trias
▢ Tonschiefer, Sandstein, Konglomerat; spätes Karbon - Perm
▢ Granit, Granodiorit, Diorit (Südböhmischer Batholith); Karbon, 340 - 300 Mill.J.
▢ Granulit (hervorgegangen aus saurem Magmatit); Ordovizium, 480 Mill.J.
▢ Orthogneis (Gföhl-Gneis, hervorgegangen aus saurem Magmatit); Ordovizium, ca. 480 Mill.J.
▢ Marmor; Neoproterozoikum
▢ Amphibolit; Neoproterozoikum - frühes Paläozoikum
▢ Migmatit (Bavarikum, hervorgegangen aus Paragneisen); Neoproterozoikum - frühes Paläozoikum
▢ Paragneis; Neoproterozoikum - frühes Paläozoikum
▢ Orthogneis; Neoproterozoikum - frühes Karbon, <1000 - 340 Mill.J.
▢ Orthogneis (Dobra-Gneis, Svetlik-Gneis); Proterozoikum, >1000 Mill.J.
▢ Granit, Orthogneis (Thaya-Granit, Weitersfeld-Gneis, Bittesch-Gneis); Neoproterozoikum; 580 Mill.J.
▢ Glimmerschiefer, Quarzit; Neoproterozoikum

Alpidisches Orogen

▢ Trachyt, Andesit, Basalt; Neogen - Quartär, 17-1 Mill.J.
▢ Tonalit, Granodiorit (Pohorje Pluton); frühes Neogen, 19 Mill.J.
▢ Tonalit, Granodiorit (Rieserferner-, Rensen-Pluton); spätes Paläogen, 40 - 30 Mill.J.
▢ Ton, Mergel, Megelstein, Sand, Kies, Kalk, Kalkstein; spätes Paläogen - frühes Neogen
▢ Kalkstein, Mergelstein, Sandstein (Klippen in der Waschbergzone); Jura - Kreide
▢ Kalkstein, Mergelstein; späte Kreide - Paläogen
▢ Dolomit, Kalkstein, Schiefer, Vulkanit; Trias - Jura

Figure A.1.: Legend of figures 1.1 and 5.1, part 1.

▭ Andesit, Rhyolith (Bozener Quarzporphyr); Perm
▭ Granit, Granodiorit (Brixner, Ifinger-Granit); Perm
▭ Tonschiefer, Sandstein, Kalkstein; spätes Karbon - Perm
▭ Kalkstein, Tonschiefer, Vulkanit; Kambrium - Devon
▭ Quarzphyllit, Phyllonit; Neoproterozoikum - Kambrium
▭ Paragneis; Neoproterozoikum - Kambrium
▭ Konglomerat, Mergel, Mergelstein, Tonschiefer, Sandstein (Gosau-Gruppe); späte Kreide - Paläogen
▭ Kalkstein, Dolomit, Mergel, Mergelstein, Tonschiefer, Sandstein; Perm - frühe Kreide
▭ Kalkmarmor, Dolomit, Quarzit, Konglomerat, Porphyroid (schwach metamorph); Perm - Jura
▭ Tonschiefer, Phyllit, Sandstein, Konglomerat, Kalkstein, Dolomit, Kalkmarmor; Karbon
▭ Marmor; spätes Ordovizium - Devon
▭ Grünschiefer, Diabas; spätes Ordovizium - Devon
▭ Phyllit, Schiefer, Grauwacke; Kambrium - Devon
▭ Porphyroid ("Blasseneck-Porphyroid"), schwach metamorph; Ordovizium, ca. 470 Mill.J.
▭ Orthogneis, Granit (Martell Granit); Perm, 285-250 Mill.J.
▭ Orthogneis; vorwiegend Karbon, 360 - 300 Mill.J.
▭ Marmor; vorwiegend Ordovizium - Devon
▭ Quarzphyllit, Glimmerschiefer, Phyllonit; Neoproterozoikum - Devon
▭ Glimmerschiefer, Paragneis; Neoproterozoikum - Devon
▭ Amphibolit; Neoproterozoikum - Devon
▭ Orthogneis; vorwiegend Ordovizium, ca. 480 Mill.J.
▭ Paragneis, Glimmerschiefer; Neoproterozoikum - Ordovizium
▭ Ultrabasit: Serpentinit, Pyroxenit; Neoproterozoikum - Ordovizium
▭ Marmor, Dolomit, Quarzit, Metakonglomerat, Porphyroid (schwach metamorph); Perm - Jura
▭ Orthogneis; Ordovizium und Karbon, ca. 480 und 350 - 300 Mill.J.
▭ Amphibolit; Neoproterozoikum - Devon
▭ Glimmerschiefer, Paragneis, Phyllit, Phyllonit; Neoproterozoikum - Karbon
▭ Tektonische Melange aus Kalkglimmerschiefer, Glimmer führendem Marmor, Phyllit (Bündnerschiefer-Gruppe) und Ophiolit: Serpentinit, Prasinit; Jura - Kreide
▭ Kalkglimmerschiefer, Tonschiefer, Phyllit, Sandstein (mit Schuppen von Gesteinen aus Paläozoikum - Trias); Jura - Eozän
▭ Kalkmarmor, Dolomit, Quarzit, Arkosegneis, Gips; Perm - Trias
▭ Ophiolit (inkl. Ultrabasit von Nauders): Serpentinit, Prasinit; Jura - Kreide
▭ Granit (Tasna-Granit); Karbon, ca. 320 Mill.J.
▭ Glimmerschiefer; Neoproterozoikum - Ordovizium
▭ Wechsellagerung aus Sandstein, Mergelstein und Tonstein ("Rhenodanubischer Flysch"); Kreide - Paläogen
▭ Kalkschiefer, Kalkglimmerschiefer, Phyllit, Glimmerschiefer, Quarzit (Bündnerschiefer-Gruppe); Jura - Eozän
▭ Ophiolit: Serpentinit, Prasinit; Jura - Kreide
▭ Kalkstein, Mergelstein, Mergel; Trias - Paläogen
▭ Kalkstein, Mergelstein, Mergel, Kohle; Jura - Paläogen
▭ Phyllit, Glimmerschiefer, Quarzit (Brennkogelserie, "Kasererserie"); Kreide
▭ Marmor (Hochstegen-, Silbereck-Marmor); später Jura
▭ Kalkmarmor, Dolomitmarmor, Quarzit, Arkosegneis, Gips, Glimmerschiefer (inkl. Schuppen aus Orthogneis); Karbon - Trias
▭ Orthogneis, Granit ("Zentralgneis"); spätes Karbon - frühes Perm
▭ Phyllit, Glimmerschiefer, basischer und saurer Metavulkanit; Kambrium - frühes Karbon
▭ Glimmerschiefer, Paragneis, Migmatit, Amphibolit; Neoproterozoikum - Ordovizium
▭ Europe NUTS 0 Boundaries

Figure A.2.: Legend of figures 1.1 and 5.1, part 2.

Valley	SL 20	SL 60	SL 100	Comment	Lenght (m)
1	58.67	58.96	58.98		2800
2	87.32	87.18	88.43		3060
3	117.37	118.84	118.78		1690
4	166.40	164.04	163.93	max	1350
5	69.24	67.48	64.55		420
5a	44.75	46.98	40.98	2 SL 100	220
6	112.36	112.27	112.04		840
7	123.46	124.19	123.96		1240
8	45.83	44.48	48.37		490
9	100.35	101.48	103.54		690
9a	8.51	11.41	13.9	1 SL 60, 1 SL 100	90
10	81.02	81.29	80.84		500
11	61.84	57.61	60.13		360
12	53.45	56.02	53.23		350
13	23.33	23.76	18.23	1 SL 100	160
14	58.52	54.97	59.71		600
16	23.97	25.22	18.72	1 SL 100	130
17	32.39	33.70	34.57	2 SL 100	190
18	29.38	29.37	29.66	NW river Melk	560
19	23.12	22.44	21.67	NW river Melk	430
20	39.00	39.03	34.87	NW	510
21	25.99	26.96	26.34	NW	480
22	46.73	46.68	47.08	NW	3230

Valley	Wdf (m)	Vf	X (m)	Y (m)
1	52	1.069	-76643	341251
2	43	1.025	-76822	340690
3	10	0.187	-77922	340156
3	15	0.284	-77922	340156
4	12.2	0.174	-78376	339606
6	4.5	0.081	-79051	339171
7	1.5	0.023	-79203	338951
9	0.5	0.011	-79434	338398
10	0.5	0.010	-79734	338180
14	2	0.036	-80568	337079
17	0.5	0.033	-80874	336527
18	4.5	0.158	-81250	336199
18	4.5	0.169	-81250	336199
19	4	0.166	-81177	336087
20	1.5	0.037	-80554	338080
21	0.5	0.018	-80633	337747
22	28.5	0.499	-81377	337758
22	34.5	0.754	-81231	337533

Table A.1.: Tables of valleys of the Zelking segment (chapter 3.1.1), both from Ranftl 2017. Top: mean SL values for calculation intervals of 20, 60 and 100 m, comments and total stream length); bottom: measured floor widths Wdf, Vf values and coordinates of measuring points.

Valley	ShpA (m^2)	RctWd (m)	RctL (m)	FlwL (m)	Re	Bs	C	Rf
1	2238745.89	1488.94	2702.97	3878.56	0.625	2.605	0.441	0.149
2	2011308.00	1347.75	2301.21	3476.62	0.695	2.580	0.539	0.166
sw 2	328185.81	467.42	934.35	1265.71	0.692	2.708	0.615	0.205
3	674600.57	840.98	1497.83	1837.98	0.619	2.186	0.415	0.200
sw 3	57519.01	215.92	504.37	557.12	0.537	2.580	0.451	0.185
4	615645.57	744.08	1103.91	1632.66	0.802	2.194	0.705	0.231
5	140493.45	328.20	755.72	808.31	0.560	2.463	0.528	0.215
5a	39715.88	137.45	539.06	560.26	0.417	4.076	0.374	0.127
6	270297.43	374.34	1040.82	1154.97	0.564	3.085	0.560	0.203
7	485894.39	848.23	1177.54	1508.19	0.668	1.778	0.494	0.214
8	115129.42	249.04	722.45	880.76	0.530	3.537	0.521	0.148
9	164129.10	291.91	969.53	1021.50	0.472	3.499	0.436	0.157
9a	22335.70	88.78	425.94	429.52	0.396	4.838	0.340	0.121
10	141838.85	298.91	706.30	831.75	0.602	2.783	0.612	0.205
12	140416.87	421.78	542.46	637.86	0.779	1.512	0.678	0.345
13	69799.07	250.96	467.37	567.54	0.638	2.262	0.620	0.217
14	167248.88	405.17	634.66	1055.95	0.727	2.606	0.583	0.150
15	20976.03	93.47	339.80	360.51	0.481	3.857	0.494	0.161
16	39141.24	178.75	378.60	463.67	0.590	2.594	0.587	0.182
17	53237.47	213.38	432.02	555.70	0.603	2.604	0.556	0.172
18	227444.31	520.64	854.99	969.65	0.629	1.862	0.505	0.242
19	107798.36	343.19	690.15	912.07	0.537	2.658	0.423	0.130
22	2103432.54	1160.94	3112.68	3610.68	0.526	3.110	0.418	0.161
21	89254.49	295.01	536.49	626.14	0.628	2.122	0.501	0.228
20	148128.95	330.03	693.67	749.30	0.626	2.270	0.631	0.264
no 3	45645.15	195.05	437.15	520.55	0.551	2.669	0.513	0.168
11	148632.13	429.74	555.65	652.71	0.783	1.519	0.717	0.349

Table A.2.: Table of geometric parameters of watersheds (shape length and area, flow length), circumscribing rectangles (width and length) around Zelking from ArcGIS and calculated Re, Bs, C, Rf values by Ranftl 2017 (chapter 3.1.1).

Valley	Wdf (m)	Vf	X	Y	Location NE to SW
3	1.4	0.03	-25973	407110	Gnadlersdorf (Hnanice)
4	1.6	0.06	-26085	407208	
5	2.2	0.04	-27064	406121	Oberretzbach
6	2.2	0.04	-29723	404926	Retz, Hölzelmühle
7	26.5	0.24	-29946	405189	
8	2.7	0.09	-30879	403915	Retz, Weißes Kreuz
9	35	0.7	-31548	402664	Rosenau, SG
10	5.8	0.12	-32923	402381	Rosenau, Kriegerdenkmal
11	8	0.64	-32841	401634	Breitenmühle
28	5.5	0.11	-35424	398669	Leodagger
44	19.3	0.32	-37904	397424	Hammerschmiede
29	16	0.18	-37056	396970	Pulkautal, Peschtamühle
41	1	0.02	-33961	395040	btw. Rohrendf. a. Groß-Reipersdf.
42	2.1	0.04	-35019	392881	Roggendorf
43	1.6	0.05	-33789	392795	Röschitz
0	200	3.64	-34977	390046	Stoitzendorf
1	100	6.45	-33299	390333	Klein Reinprechtsdorf
39	92	8.1	-34470	388839	Grafenberg
40	37.2	7.5	-33831	388869	Wartberg
38	60	2.45	-35870	386989	Etzmannsdorf
2	17.5	0.35	-35853	385654	Straning - Aumühle
30	13	0.34	-36582	384807	Limberg - hinter Steinbruch
31	7	0.23	-36057	383600	Oberdürnbach
32	7.5	0.75	-36286	383107	Oberdürnbach - Marterl
33	2	0.1	-37151	382464	Maissau - Juliusberg
34	6.2	0.35	-38265	381421	Maissau
35	3.8	0.17	-38164	381235	
36	3.6	0.11	-38535	380929	Maissau - Klosterbigl
12	5	0.16	-40012	380283	Grübern
13	2	0.03	-41756	379873	Eggendorf - Klein Burgstall
14	26	0.39	-41395	379408	
37	1.4	0.03	-42390	378169	Zemling - Manhartsberg
15	12.3	0.25	-42135	377878	
16	12.5	0.22	-43595	376758	Diendorf, Bösendürnbach
17	61.5	0.72	-42199	374846	
18	6.5	0.92	-45401	375495	
19	7.5	0.18	-45541	375347	Wolfsgraben
20	8.6	0.16	-45651	374987	and
21	19.3	0.32	-45660	374823	Straßertal
22	77.7	1.7	-45636	374391	
23	55.1	1.47	-45660	373476	
24	52.9	0.62	-45419	373198	
25	58	0.73	-45194	373171	
26	4.5	0.11	-44683	373065	
27	96	1	-44478	372705	

Table A.3.: Table of Vf values and coordinates of measuring points of the valley floor width Wdf around Maissau and Pulkau. (chapter 3.1.2).

No	ShpA (m^2)	RctWd (m)	RctL (m)	FlwL (m)	Re	Bs	C	Rf
1	8177074.15	1889.69	7973.30	9567.46	0.405	5.063	0.28	0.089
2	6226290.17	1774.74	5429.74	6693.75	0.519	3.772	0.359	0.139
3	1591135.60	784.90	3226.96	3856.42	0.441	4.913	0.367	0.107
4	4418468.98	1648.15	4756.56	5257.89	0.499	3.19	0.395	0.16
5	31177723.69	6105.46	13679.44	20736.09	0.461	3.396	0.231	0.073
6	483208.58	711.48	1326.17	1897.99	0.591	2.668	0.454	0.134
7	11252462.47	3184.55	5589.50	7412.33	0.677	2.328	0.514	0.205
8	3730133.02	1596.68	4124.12	5358.33	0.528	3.356	0.432	0.13
35	2475874.82	969.71	3507.87	3928.99	0.506	4.052	0.454	0.16
36	4554202.68	2066.37	4900.77	6002.87	0.491	2.905	0.342	0.126
37	2095486.65	1334.11	2734.97	4862.82	0.597	3.645	0.363	0.089
38	2458259.31	1112.37	4659.04	5259.31	0.380	4.728	0.291	0.089
39	1705091.35	770.93	3600.45	3927.15	0.409	5.094	0.339	0.111
40	1255955.17	847.12	3699.33	4315.82	0.342	5.095	0.225	0.067
41	927474.03	594.75	3751.54	4104.06	0.290	6.9	0.176	0.055
42	15752844.40	2928.49	10585.88	13092.31	0.423	4.471	0.264	0.092
43	2788271.57	1512.49	4113.11	5072.99	0.458	3.354	0.316	0.108
44	351868.20	295.71	1962.99	2173.92	0.341	7.351	0.253	0.074
45	468196.52	345.17	2228.57	2397.82	0.346	6.947	0.258	0.081
46	1104800.90	508.34	3401.99	3813.86	0.349	7.503	0.253	0.076
47	995115.90	622.37	3266.77	3548.82	0.345	5.702	0.232	0.079
48	2595810.19	1956.28	2494.04	3092.97	0.729	1.581	0.429	0.271
49	821111.69	787.30	1517.32	2044.18	0.674	2.596	0.617	0.197
50	1289074.75	986.54	1963.32	2282.36	0.653	2.313	0.616	0.247
51	793177.62	838.66	1576.40	2249.80	0.637	2.683	0.574	0.157
52	2479841.37	1806.44	2629.63	4181.53	0.676	2.315	0.459	0.142
53	1356515.95	1478.59	1633.99	2188.48	0.804	1.48	0.542	0.283
54	3154460.07	1206.50	3618.68	4043.33	0.554	3.351	0.531	0.193
55	1098239.87	639.06	3109.31	3462.06	0.380	5.417	0.302	0.092
56	1202758.63	715.12	3110.35	3496.63	0.398	4.89	0.286	0.098
57	1523235.70	881.21	3029.25	3567.06	0.460	4.048	0.357	0.12
58	1465079.31	982.35	2997.20	3464.19	0.456	3.526	0.352	0.122
59	1558320.84	1032.89	2942.46	3390.16	0.479	3.282	0.332	0.136
60	11682578.42	2836.78	8027.04	9487.90	0.480	3.345	0.324	0.13
61	79702073.66	9076.52	20399.07	33095.10	0.494	3.646	0.165	0.073
62	9873552.62	3558.64	6232.35	7791.95	0.569	2.19	0.31	0.163
63	1555744.40	1089.27	3034.40	3847.84	0.464	3.532	0.305	0.105
64	1166260.59	608.13	2816.23	3237.69	0.433	5.324	0.373	0.111
65	1273424.83	704.13	2876.19	3408.33	0.443	4.841	0.334	0.11
66	549339.02	444.17	2320.17	2467.38	0.360	5.555	0.27	0.09
67	883506.24	721.87	2455.89	2910.50	0.432	4.032	0.312	0.104
68	4265349.90	2337.30	3812.62	5888.46	0.611	2.519	0.302	0.123
69	616985.38	488.15	2490.42	2721.58	0.356	5.575	0.246	0.083
70	2859060.60	1203.03	4579.02	5415.45	0.417	4.501	0.294	0.097
71	4394703.88	1525.37	4172.07	5332.59	0.567	3.496	0.466	0.155
72	4740466.95	1743.41	4493.38	5502.63	0.547	3.156	0.429	0.157
73	7481883.30	2633.90	4005.95	5249.73	0.770	1.993	0.625	0.271
74	61271386.13	9407.78	13607.78	20936.45	0.649	2.225	0.289	0.14
75	26554921.79	3499.71	14002.20	18808.86	0.415	5.374	0.232	0.075
76	5240228.47	1974.50	4770.20	6469.02	0.541	3.276	0.448	0.125
77	24042968.76	4534.51	9277.29	12353.40	0.596	2.724	0.44	0.158

Table A.4.: Table of geometric parameters as in table A.2 around Maissau and Pulkau, values by Hintersberger and Decker 2018 (chapter 3.1.2).

No	X (m)	Y (m)	Ground L (m)	Quat base (m)	Quat over	Top Cryst (m)	Quat thick (m)	Mio thick (m)
61	-78889	343174	211.8	196.7	Melk Sand		15.1	
62	-78433	343160	210.7	197.8	Melk Sand		12.9	
63	-78152	343181	210.15	197.55	Melk Sand		12.6	
64	-77936	343179	210.55	197.25	Melk Sand		13.3	
65	-77536	343152	210.75	197.15	Melk Sand		13.6	
66	-77311	343180	210.45	197.15	Melk Sand		13.3	
67	-77154	343140	210.55	197.15	Melk Sand		13.4	
68	-76837	343157	209.8	197.6	Melk Sand		12.2	
69	-76541	343169	210.1	197	Melk Sand		13.1	
97	-76079	343248	209	199.3	cryst. rock	199.3	9.7	0
98	-75983	343261	209.35	197.55	Melk Sand	183.75	11.8	13.8
99	-76145	343034	208.6	196.9	Melk Sand	171.7	11.7	25.2
187	-80202	342922	210.5	199.1	Melk Sand		11.4	
188	-80200	342923	210.5	198.8	clay marl		11.7	
189	-80146	342931	210.5	198.7	Melk Sand		11.8	
190	-80076	342960	210.5	200.7	Melk Sand		9.8	
191	-79999	342984	210.7	197.9	Melk Sand		12.8	
192	-79564	343092	211.45	199.25	Melk Sand		12.2	
222	-78430	342832	210.4	198.6	cryst. rock	198.6	11.8	0
223	-79415	342652	211.3	199.5	Melk Sand		11.8	
224	-79400	341969	211.9	200	cryst. rock	200	11.9	0
225	-80068	342431	210.75	198.95	Melk Sand		11.8	
226	-80144	341921	212.35	199.85	Melk Sand		12.5	
301	-78465	343325	211.2	195.6	Melk Sand		15.6	
302	-79410	343191	211.4	196.8	Melk Sand		14.6	
303	-80198	342919	212	198	Melk Sand		14	
304	-81063	342669	212.25	200.55	Melk Sand		11.7	
305	-80939	343081	211.1	201.6	Melk Sand		9.5	
306	-82447	342537	212.4	199.4	Melk Sand		13	
384	-80854	342718	211.45	199.55	Melk Sand		11.9	
385	-80667	342782	210.9	200.3	Melk Sand		10.6	
386	-79124	343168	208.67	197.57	Melk Sand		11.1	
387	-79005	343179	205.15	194.75	Melk Sand		10.4	
388	-78876	343195	208.2	197.1	Melk Sand		11.1	
389	-78975	343175	206.13	195.43	Melk Sand		10.7	
390	-79045	343178	206.8	196	Melk Sand		10.8	
617	-79539	339540	224.4	212.3	cryst. rock	212.3	12.1	
618	-77419	343300	210	197.4	Melk Sand		12.6	5.4
619	-77079	341810	213.9	206.8	Melk Sand		7.1	
620	-77769	341040	218.8	208.4	Melk Sand		10.4	
657	-78810	342729	210	197.8			12.2	
658	-78822	342759	209.9	197.8			12.1	
659	-78801	342947	210.85	197.75	Melk Sand		13.1	
660	-79332	342644	211.15	199.85	Melk Sand		11.3	
661	-79558	342871	210.8	197.1	Melk Sand		13.7	
1	-77327	343616	210.4	198.6	cryst. rock	198.6	11.8	0
2	-75616	343803	210.05	198.65	Melk Sand		11.4	
3	-75554	343596	209.5	198.1	cryst. rock	198.1	11.4	0
4	-75505	343441	209.35	199.55	Melk Sand	195.95	9.8	3.6
5	-75485	343841	210.3	196.2	Melk Sand	148.3	14.1	47.9
6	-75405	343617	209.15	198.35	cryst. rock	198.35	10.8	0
7	-75359	343502	208.6	199.2	cryst. rock	199.2	9.4	0
8	-75332	343889	210.35	195.65	Melk Sand		14.7	
9	-75291	343786	209.25	194.85	cryst. rock	194.85	14.4	0
10	-75251	343664	208.35	197.75	cryst. rock	197.75	10.6	0
11	-77313	343424	210	198.5	Melk Sand		11.5	
12	-76462	343714	209.5	194.2	cryst. rock	194.2	15.3	0
13	-75122	343721	208.05	198.35	cryst. rock	198.35	9.7	0
14	-74775	343942	207.85	197.75	Melk Sand	170.95	10.1	26.8
15	-76418	343525	208.75	196.95	Melk Sand	182.75	11.8	14.2
18	-76453	343665	209.55	197.05	Melk Sand		12.5	

No	X (m)	Y (m)	Ground L (m)	Quat base (m)	Quat over	Cryst top (m)	Quat thick (m)	Mio thick (m)
23	-76143	343759	210.2	197.7	cryst. rock	197.7	12.5	0
24	-76264	343479	208.85	197.15	Melk Sand	177.05	11.7	20.1
25	-75787	343593	208.5	194	Melk Sand	183.8	14.5	10.2
26	-75671	343895	207.85	197.35	cryst. rock	197.35	10.5	0
27	-75698	343697	209.85	197.25	Melk Sand	170.45	12.6	26.8
28	-75682	343522	208.75	196.55	Melk Sand	186.95	12.2	9.6
29	-75395	344082	210.05	198.05	Melk Sand	160.65	12	37.4
30	-75359	343954	209.45	197.05	Melk Sand	143.15	12.4	53.9
31	-75323	343852	210.35	195.15	Melk Sand	135.35	15.2	59.8
32	-75303	343798	209.75	193.25	Melk Sand	173.75	16.5	19.5
34	-75221	343925	210.3	196.3	Melk Sand	125.5	14	70.8
35	-75178	343844	208.55	195.05	Melk Sand	182.55	13.5	12.5
36	-76637	343361	209.05	195.65	Melk Sand	159.85	13.4	35.8
37	-76084	343669	209.8	197.1	Melk Sand	159.2	12.7	37.9
38	-76326	343705	209.65	197.85	Melk Sand	181.85	11.8	16
39	-75875	343275	209.9	199	Melk Sand	152.7	10.9	46.3
40	-75932	343556	209.9	196.6	Melk Sand	136.9	13.3	59.7
41	-76030	343449	209.75	195.55	Melk Sand	171.25	14.2	24.3
42	-75159	344165	210.05	197.25	Melk Sand	175.35	12.8	21.9
43	-75193	343560	208.9	198.7	Melk Sand	187.1	10.2	11.6
44	-75783	343812	209.8	198	cryst. rock	198	11.8	0
45	-75758	343777	209.75	198.05	cryst. rock	198.05	11.7	0
46	-75729	343733	209.85	197.95	Melk Sand	181.55	11.9	16.4
47	-76124	343725	208.8	198.4	cryst. rock	198.4	10.4	0
48	-76108	343696	209.75	197.75	Melk Sand	182.75	12	15
49	-76395	343704	209.5	197.2	Melk Sand	185	12.3	12.2
50	-75778	343398	209.5	198.2	Melk Sand	162.8	11.3	35.4
51	-76044	343589	210.05	195.65	Melk Sand	133.25	14.4	62.4
61	-78889	343174	211.8	196.7	Melk Sand		15.1	
62	-78433	343160	210.7	197.8	Melk Sand		12.9	
63	-78152	343181	210.25	197.55	Melk Sand		12.7	
64	-77936	343179	210.55	197.25	Melk Sand		13.3	
65	-77536	343152	210.75	197.15	Melk Sand		13.6	
66	-77311	343180	210.45	197.15	Melk Sand		13.3	
67	-77154	343140	210.55	197.15	Melk Sand		13.4	
68	-76837	343157	209.8	197.6	Melk Sand		12.2	
69	-76541	343169	210.1	197	Melk Sand		13.1	
70	-76506	343555	208.5	195.6	Melk Sand	179.1	12.9	16.5
71	-76251	343634	209.3	197.4	Melk Sand	180.65	11.9	16.75
72	-76219	343441	208.95	196.75	Melk Sand	171.95	12.2	24.8
73	-76179	343232	209.4	199.2	cryst. rock	199.2	10.2	0
74	-76509	343589	208.75	195.55	Melk Sand	179.75	13.2	15.8
75	-76271	343516	209.3	196.5	Melk Sand	179.4	12.8	17.1
76	-76197	343317	210.2	198.7	Melk Sand	173.8	11.5	24.9
90	-74301	344279	209.2	197.1	Melk Sand		12.1	
91	-74920	344081	209.4	197.6	Melk Sand		11.8	
92	-74685	344327	209.25	197.75	cryst. rock	197.75	11.5	0
93	-74441	344290	207.65	196.85	Melk Sand		10.8	
100	-75954	343720	209.3	196.6	Melk Sand	182.5	12.7	14.1
101	-75906	343734	210.55	196.05	Melk Sand	183.9	14.5	12.15
102	-75858	343748	210.3	197.8	Melk Sand	197.2	12.5	0.6
103	-75810	343762	210.1	197.9	cryst. rock	197.9	12.2	0
104	-76407	343466	209.25	198.55	Melk Sand	185.85	10.7	12.7
105	-76506	343358	210.2	197.4	Melk Sand	181	12.8	16.4
106	-76406	343364	210.35	197.05	Melk Sand	183.95	13.3	13.1
107	-76326	343251	209.6	197.6	Melk Sand	176.8	12	20.8
108	-76389	343276	209.75	199.05	Melk Sand	177.25	10.7	21.8
109	-76326	343309	209.6	197.5	Melk Sand	170.4	12.1	27.1
110	-76458	343183	210	198	Melk Sand	176.9	12	21.1

Table A.5.: Table of borehole locations of the Danube hydroelectric power plant drillings plus data plotted in figures 3.8 and 3.9, (chapter 3.2.1).

Profile	X (m)	Y (m)		Location
GEP1 long	-76860	341502	SE	Großpriel
	-76918	341584	Street	
	-77065	341788	NW	
GEP1 short	-76891	341507	SE	
	-76936	341558	NW	
GEP2 short	-77824	340635	SE	Matzleinsdorf
	-77904	340785	NW	
GEP2 long	-77826	340624	SE	
	-77989	340936	NW	
GEP3	-78593	339939	SE	Zelking - Mösel
	-78806	340217	NW	
GEP4 long	-80313	337814	NE	Zelking - parallel River Melk and DF
	-80417	337675	SW	
GEP4 short	-80344	337771	NE	
	-80386	337713	SE	

Table A.6.: Starting and ending coordinates of geoelectrical profiles (GEP) discussed in chapter 3.2.1.

Location	**Dip Dir**	**Dip**	**Lin**		**sense**	Comment
Großpriel	230	88				crystalline rocks
	075	75				crystalline rocks
	286	86				crystalline rocks
	075	61				crystalline rocks
	111	74				crystalline rocks
	064	73				crystalline rocks
	248	80				edge ’post hole’ in trench
	298	26				channel in trench, right (SE)
	090	67				channel in trench, left (NW)
Langenlois Wolfgraben	006	82			dn	loess
	012	72			dn	loess
	321	74				loess (fracture)
	319	76				loess (fracture)
	228	87			dn	conglomerate
	257	72			dn	conglomerate
	241	86			dn	conglomerate
	231	75			dn	conglomerate
Langenlois brickyard	354	70			dn	E wall
	348	80			dn	E wall
	342	80			dn	E wall
	205	78			dn	SW wall
	192	78			dn	SW wall
	208	75			dn	SW wall - 1,5 cm offset
	193	76	172	69	dn	SW wall
	184	79			dn	SW wall
	253	79			dn	S wall
	070	81			dn	S wall
	250	50			dn	S wall
	071	89			dn	S wall
	066	55			dn	S wall
	264	82			dn	S wall
	283	85			dn	S wall
	076	86			dn	S wall
	083	59			dn	?
	084	79			dn	?
Langenlois Loisium	019	71			dn	SE corner, next fault S from main
	002	71			dn	W wall, S! \
	344	86			dn	W wall /
	352	85			dn	W wall main fault S \
	019	85			dn	W wall
	184	71			dn	W wall
	204	89			dn	W wall
	208	66			dn	W wall main fault N bottom
	188	79			dn	W wall main fault N
	188	64			dn	W wall main fault NN
	186	60			dn	W wall with conjugate X (N from main)
	187	83			dn	W wall, N!
	014	78			dn	SE corner main fault
	031	56			dn	NE corner
	026	61			dn	NE corner
	026	64			dn	NE corner
	034	73			dn	NE corner bottom (W)
	026	67			dn	NE corner top
	160	47			dn	E wall \
	029	76			dn	SE corner, S wall
	041	72			dn	S wall, further W
	202	69			dn	E wall \
	014	78			dn	SE corner (E wall \)
	019	71			dn	SE corner (E wall \)
	203	75			dn	S wall slickenside

Location	**Dip Dir**	**Dip**	**Lin**		**sense**	Comment
	023	78			dn	S wall slickenside (small fault plane, E!)
	183	89	124	83	dn	S wall slickenside
	175	77			dn	S wall slickenside
	181	85	080	78	dn	S wall slickenside
	202	74	158	65	dn	S wall slickenside
	199	88			dn	W wall
	180	79			dn	W wall
	014	75			dn	W wall
Langenlois Geißberg	193	82	274	5		
	206	64	291	9		
	185	77				
	132	66				
	154	76				
	184	81	196	82		
	173	80				
	213	70				
	336	62				
	330	62				
	033	64				joint

Table A.7.: Compass measurements from southwest to northeast.

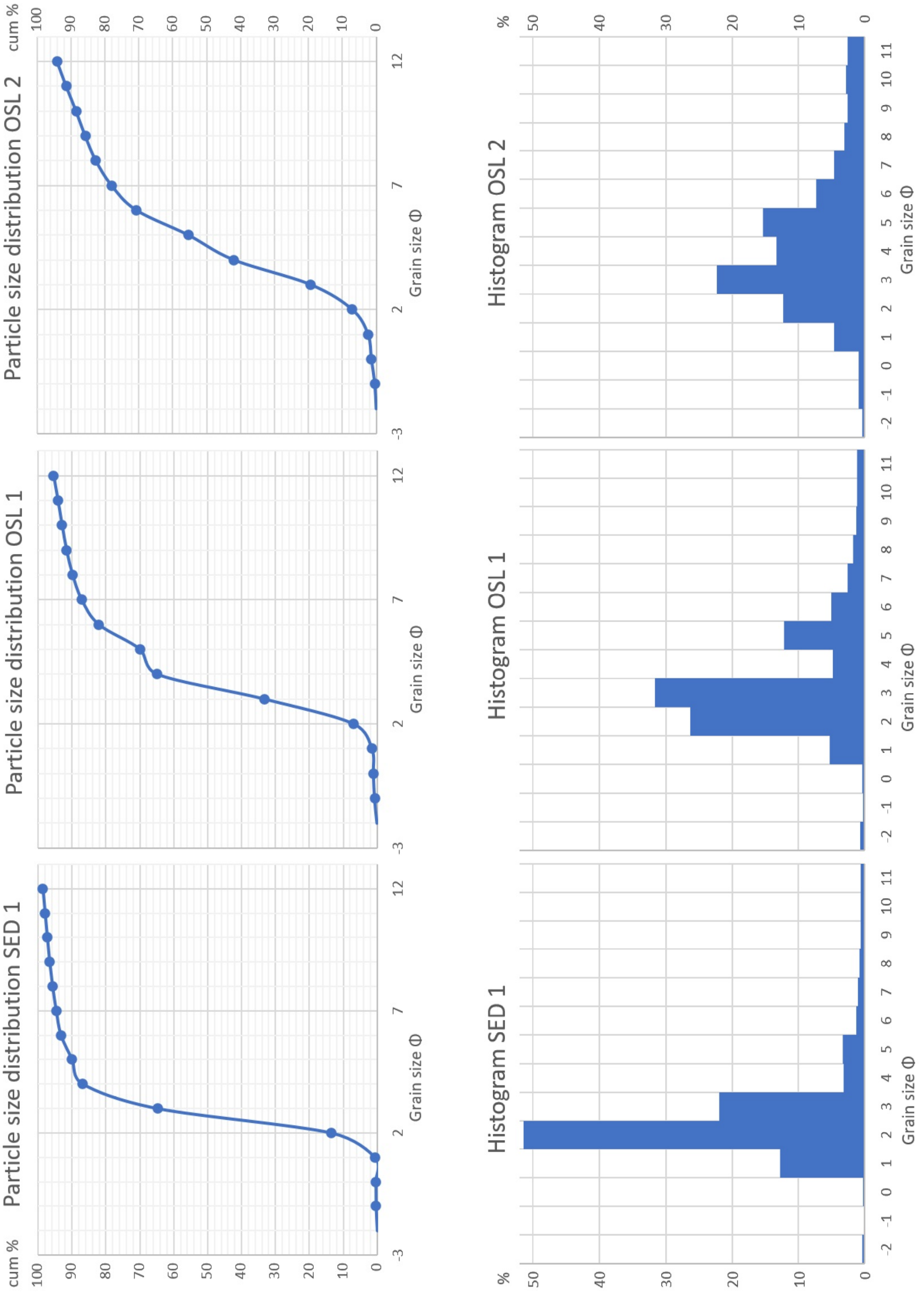

Figure A.3.: Grain size distributions (top/left) and histograms (bottom/right) of sediment samples SED 1, OSL 1, OSL 2 from trench (Großpriel, chapter 3.2.2).

GRAIN SIZE STATISTICS – PARAMETER DEFINITION			
Moment Method		**Graphically (Folk and Ward 1957)**	
		Median (Φ)	$Md = \Phi_{50}$
		Modus (Φ)	Mo = most frequently occuring grain size
Mean (Φ)	$\bar{x} = \sum \frac{f_i m_i}{100}$	Mean (Φ)	$M = \frac{\Phi_{16} + \Phi_{50} + \Phi_{84}}{3}$
Standard deviation	$\sigma = \sqrt{\frac{f_i(m_i - \bar{x}^2)}{100}}$	Sorting	$So = \frac{\Phi_{84} - \Phi_{16}}{4} + \frac{\Phi_{95} - \Phi_5}{6.6}$
Skewness	$\alpha_3 = \frac{f_i(m_i - \bar{x})^3}{100\sigma^3}$	Skewness	$Sk = \frac{\Phi_{16} + \Phi_{84} - 2\Phi_{50}}{2(\Phi_{84} - \Phi_{16})} + \frac{\Phi_5 + \Phi_{95} - 2\Phi_{50}}{2\Phi_{95} - \Phi_5}$
Kurtosis	$\alpha_4 = \frac{f_i(m_i - \bar{x})^4}{100\sigma^4}$	Kurtosis	$K = \frac{\Phi_{95} - \Phi_5}{2.44\Phi_{75} - \Phi_{25}}$

Particle size classes $\Phi = -\frac{\log(mm)}{log(2)}$

f_i = frequency of grain size (%) per Φ-interval with midpoint m_i; Φ_i = ith percentile of cum. frequency curve

CALCULATION	**sample SED 1**		**sample OSL 1**		**sample OSL 2**	
Moment Method	value	description	value	description	value	description
$\bar{x}(\Phi)$	3.17		4.22		5.26	
σ	1.90	poorly sorted	2.49	very poorly srt.	3.00	extr. poorly srt.
α_3	2.80	strongly pos.	1.53	pos. skewed	0.90	pos. skewed
α_4	12.51	extr. leptok.	5.63	very leptok.	3.31	leptokurtic
Graphically						
$Md(\Phi)$	2.7		3.5		4.6	
$Mo(\Phi)$	2.5		3.2		3.4	
$M(\Phi)$	2.87		4.07		5.25	
So	1.3	poorly sorted	2.7	very poorly srt.	3.0	very poorly srt.
Sk	0.4	strongly pos.	0.5	strongly pos.	0.4	strongly pos.
K	2.2	very leptok.	1.7	very leptok.	1.4	leptokurtic

Table A.8.: Grain size parameters: Definition and formulae (top), calculations based on moment statistics (interpretation after Friedman 1962) and graphical derivation after Folk and Ward 1957 (bottom).

Paleoseismological Trench - Diendorf Fault
City of Melk, Großpriel

Orthorectified Photomosaic of NE and SW section
grid spacing is 0.5 m